OVGU Magdeburg

Doctoral Thesis

On the elastic-plastic behaviour of regular honeycomb structures

Author: Sara Bucci

A thesis submitted in the

in the

Institut für Mechanik
Otto-Von-Guericke Universität Magdeburg
Department of mechanics

December 2017

"Nothing behind me, everything ahead of me, as is ever so on the road."

Jack Kerouac, On the Road

Zusammenfassung

Institut für Mechanik - OVGU Magdeburg

On the elastic-plastic behaviour of regular honeycomb structures

by M. Sc. Sara Bucci

Innerhalb der Gruppe der periodischen, zellulären Materialien sind Wabenstrukturen mit am leichtesten und widerstandsfähigsten. Sie sind weit verbreitet im Einsatz, zum Beispiel in der Luft- und Raumfahrt, der Automobilindustrie und der Verpackungsindustrie. Gibson und Ashby behandeln die lineare Elastizität von Wabenstrukturen mit Hilfe der mechanischen Bilanzen, Experimente und numerische Simulationen sind in Papka und Kyriakides zu finden. In dieser Arbeit wird das ebene, elastisch-plastische Verhalten auf drei unterschiedlichen Größenskalen untersucht. Auf der Mikroebene werden Finite-Elemente-Simulationen (FE) mit Hilfe des FE-Werkzeugs Abaqus durchgeführt, um relevante elastische und plastische effektive Materialkennwerte wie den Elastizitätsmodul und die Fließfläche zu erhalten. Anschließend wird ein effektives Materialgesetz entwickelt, mit dem verschiedene Probleme, wie die nicht-Konvexität der Fließfläche, die Gültigkeit von Druckers Postulat und die Gültigkeit einer assoziierten Fließregel diskutiert werden. Des weiteren wird auf einer meso-Ebene ein Feder-Balken-Modell entwickelt, anhand dessen eine analytische Homogenisierung der Wabenstruktur erfolgt. Für die Plastizität wird anhand der effektiven Verfestigung von Balken bei Biegung sowie der Symmetrie der Struktur ein Prediktor-Korrektor Einschrittverahren entwickelt. Das daraus resultierende effektive Modell wird auf der Makroebene in FE Simulationen untersucht, wobei sich zeigt, dass einige Charakteristika der Plastizität von Wabenstrukturen, insbesondere der Beginn von Dehnungslokalisierung, erfolgreich reproduziert werden können. Diese Analyse wurde für zwei Materialien durchgeführt, nämlich Aluminium und Polyethylen, welche repräsentativ in ihrer jeweiligen Materialklasse (Metalle und Thermoplaste) sind. Der vorgeschlagene Ansatz ist neu und erstaunlich einfach, weswegen er gut als Ausgangspunkt für weitere Untersuchungen dienen kann. Sinnvolle Erweiterungen könnten zum Beispiel die Formulierung für große Deformationen und für Medien mit inneren Freiheitsgraden (Mikropolare Theorie oder Gradienten-Theorie) sein. Die Methode kann weiterhin leicht auf andere zelluläre Strukturen übertragen werden.

Contents

List of Figures

List of Tables

Chapter 1

Introduction

Humans have always tried to understand the nature, to know how it works, and to learn how to use it for their own needs, to imitate it and even to improve it. Every scientific field that has been developed during the history, has born to solve clues imposed by the nature Russo [2013]. Honeycomb structures are an example of this: the perfection of the bees' regular hexagonal honeycomb, which is extremely light, spacious and resistant, was inspiring artists, designers and lately engineers, which in 1938 a.C. reproduced, for the first time, structures with this shape and characteristics (see Cross [1990]). What is more, during the previous and last centuries, technology has developed exponentially, making always easier the realization of almost any desired structure. Processes like 3-D printing, electro-spinning, foaming, selective laser sintering and other advanced techniques for manufacturing, have made the production of complex materials possible, materials which present new and very different characteristics (for a general discussion on this argument see dell'Isola et al. [2015]). This allowed industries to invent and produce almost every kind of structure, which may have all the necessary properties to satisfy the requirements for a given scope. Every thinkable and printable material becomes then a new subject of study.
In this framework, cellular solids like foams or honeycomb-like structures, are replacing full solids, thanks to their better and optimized properties. In particular, because of their structure, cellular solids permit the minimization of the used material, maximizing, at the same time, the strength, the thermal properties, the energy absorption and so on. This not only reduces the costs of production, but also widens the applicability of such materials.
What distinguishes cellular solids from bulk material, is indeed their internal structure: as suggested by the name, these are media made of cells which are interconnected by solid struts and which fill the space. If the cells of the structure can connect to each other through open faces then it is called open-celled, while if the cells are separated through solid walls then it is called closed-celled. Most of the foams are part of the first family, some of them are partially open and partially closed, and almost all honeycomb-like structures belong to the second family.

In nature there exist many materials, like wood or cork, which can be idealized as honeycomb structures. Building a model for such natural materials is very convenient, because of the simplified geometry which makes the mechanisms of deformation and failure easier to analyze. Since always man had tried to imitate nature and also in this case we try to reproduce a structure which is convenient from many points of view (as we already stated). That is why we build honeycombs made of polymers, metal or ceramic

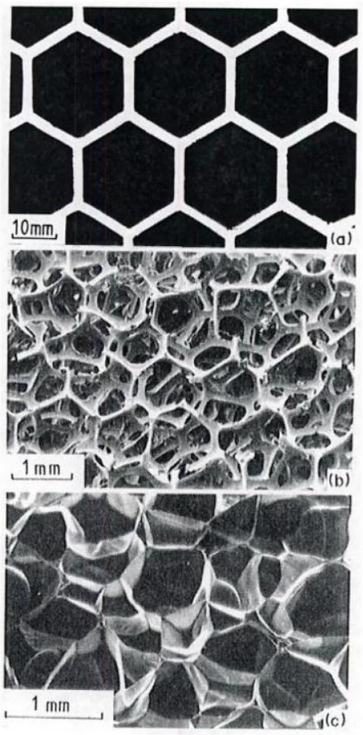

Figure 1.1: Examples of open and closed celled structures: a) hexagonal honeycomb; b) open celled foam; c) closed celled foam. (Gibson and Ashby [1997])

to fill sandwich panel cores.
The peculiarity of these structures is that they all have one or more internal length scale. This fact awards them for all the aforementioned properties which need a specific mathematical framework in order to be properly modelled. In particular, for materials that have a microstructure, the overall mechanical behaviour depends on the interaction between the different length scales.
Because of their wide use, either as structural components or for other applications, it is important to study the global behaviour of honeycombs, of which their yielding and failure mechanisms are most interesting.
Let us have al look at Figures 1.2a and 1.2b, where an in-plane compression test on an aluminium specimen of honeycomb structure is performed. The overall crushing behaviour can be summarized as follows:

0-1 In the initial configuration and geometry, we have linear elastic behaviour.

1-2 Then, non-linear elastic behaviour starts, with the consequent reduction in stiffness.

2-3 Immediately follow the on-set of localization and the collapse of the first row of cells.

3-4 Then the deformations spread to the neighbouring rows, leaving the rest undeformed.

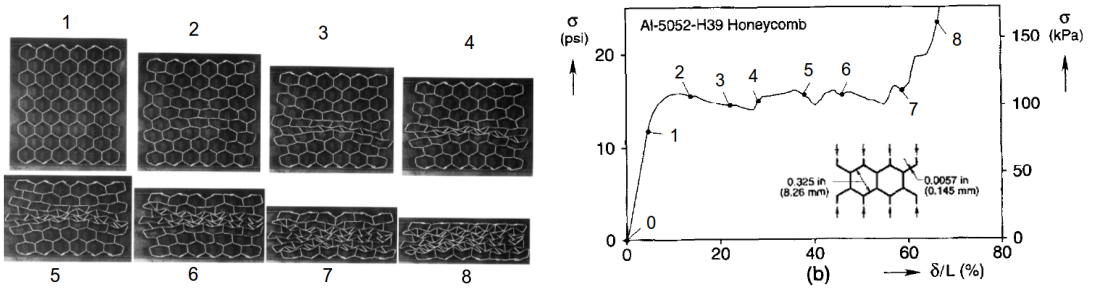

Figure 1.2: Crushing of a compressed 6x6 cell aluminium honeycomb structure and the corresponding stress strain curve. Experimental results from Papka and Kyriakides [1994]

4-5-6 The collapsing of the first row triggers the one of the neighbouring ones subsequently; the contact between cell's walls causes the increasing of stiffness.

7-8 At the end, almost all cells have collapsed and got in contact; a sharp rise of the load required for further deformations is experienced.

We see that their unusual way of in-plane localization by collapse of adjacent rows suggest a non-classical evolution of the deformations of the structure. The observed behaviour is also widely described in Zhang and Ashby [1992], Papka and Kyriakides [1999a,b] and Zhu and Mills [2000], where not only uni-axial compression tests, but also multi-axial compression, tension or indentation tests are performed.
Understanding this behaviour will allow engineers to optimize the properties of the honeycombs and even to modify the structure itself in order to get non-classical, even exotic behaviours (see dell'Isola et al. [2015]).

Structure of the work and goals

The structure of this work is shown in the diagram (1.4). The central topic of the study are honeycomb structures, in the pink rectangle, and, in particular, their mathematical model concerning elastic and plastic behaviour. In the green boxes the chapters are presented, each of them related to the central one through one arrow. The directions of the red arrows indicate what we obtained studying the specific topic, while the black ones rather state the approach or method used. Finally the dotted lines indicate sub-arguments included in the relative topic.
The study is conducted on three different scales: the micro-scale, where we study a representative volume element (RVE), with the actual material properties, we set a boundary value problem (BVP) and perform numerical homogenization; the meso-scale, where we use the same RVE but we now look at the cell size, with a system of three bars, on which we perform analytical homogenization and develop an algorithm for the plastic problem; finally the macro-scale, coming both from the micro- and meso-scales, where we forget the structure inside the body, and we look at it as a continuum with the material properties coming out from the homogenization procedures. The whole analysis is conducted on two core materials, namely polyethylene and aluminium which are representative for

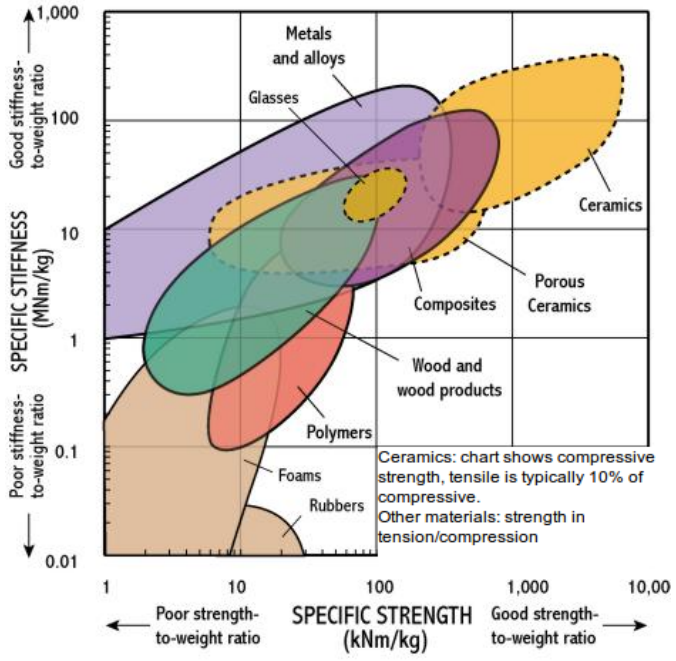

Figure 1.3: Specific stiffness vs specific strength graph

a weak and a strong material respectively (as we can see from Figure 1.3[1]).

The first part of the thesis is introductory, especially the first two chapters, where we explain what honeycomb structures are, the way they are produced and utilized. Not less important, we also give a small review on the existing works about them. In chapter 3 some basic notions of mechanics are given, which will be useful for reading this work. Already from the fourth chapter, we start with some considerations and observations about these cellular solids.

A numerical laboratory based on FE simulations on a representative volume element is presented in chapter 5. Through a parametrization of the stress tensor we are able to represent the yield surface of the cellular solid. We observe and discuss the plastic flow direction and the validity of the associative flow rule. Moreover, we use a non-classical procedure to find the yield surface through a mathematical fit to the one obtained by FE simulations. This is then implemented in chapter 6 and discussed in chapter 7, where we do some observations about the effect of the non-convexity of the yield limit.

In chapter 8 we face the small strain linear elastic problem with a homogenization approach which will be used later to get one of the main results. We also propose an algorithm, which we develop based on hardening of elastic-plastic beams, as alternative to the classical associative flow rule.

In the ninth chapter (9), we fit the elastic and plastic parameters so that the stress-strain curves are comparable to the ones obtained on the micro-scale. Finally, in the tenth chapter (10) we implement the system of equations and the algorithm in Mathematica, to obtain the evolution of the yield surface through the use of two state variables. Moreover, we write the algorithm in ABAQUS UMAT, as material model for an homogeneous 2D sheet of material, to see if it is capable to capture the localization of the deformations. Notice that, in almost every section, results given by numerical finite element simulations are presented to support and visualize the discussed topics.

[1]Figure 1.3 is taken from Cambridge University, Department of Engineering, Material selection and processing (see http://www-materials.eng.cam.ac.uk/mpsite/).

In the last chapter, we sum up the obtained results, underline the strengths and limitations of the used approach and finally we give an outlook and propose some step forward for next studies.

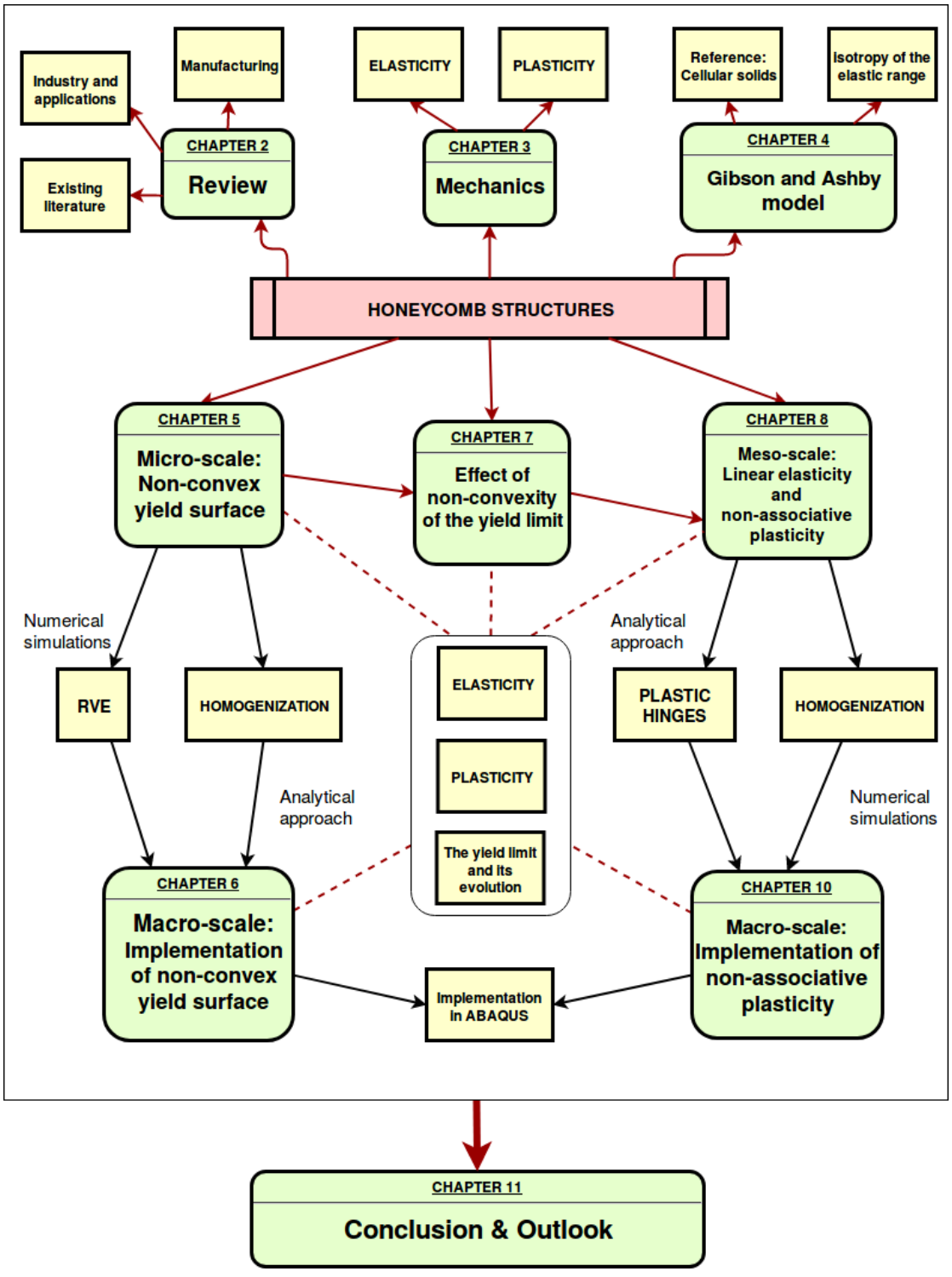

Figure 1.4: Logic scheme of the thesis

Chapter 2

Honeycomb structures: review, industry and manufacturing

2.1 Introduction

A cellular solid is one which is composed of a network of solid plates or beams which form the faces or the edges of cells. Such structures can have different shapes of cells like circular, triangular, squared or, in our case, hexagonal. Honeycomb structures (briefly called honeycombs) are indeed solids with a periodic cellular structure which gives them their main advantage of being very light but still highly stress resistant. This peculiarity is strictly connected to the relative density ratio, defined as the ratio between the structural density and the density of the core material (in our case polyethylene and aluminium), which also determines the failure mode of the structures, its manufacturing process and final use. Metallic honeycomb structures are produced mainly through two different processes: by expansion (the most used), where the sheets of metal are bound together by strips of glue and then expanded (Figure 2.3), and by corrugation, where the sheets of metal are first corrugated into half hexagons, and then glued together (Figure 2.2). Instead, thermoplastic material honeycombs are produced mainly by injection moulding, giving them a more regular structure. For a general overview on honeycombs, see, e.g., Ali and Jun [2014], Gibson and Ashby [1997], Masters and Evans [1996].
Honeycombs, and cellular solids in general, are often used as core materials for sandwich panels and shells for energy absorption, in particular for structural or packaging applications, for heat dissipation or vibration control. Moreover, their simple production processes make these structures very appealing from an engineering and industrial point of view.
In this chapter we will give a review of the works done on honeycombs so far, we will describe some of the manufacturing processes used to create metallic honeycomb panel cores and we will see which are the main applications for such structures.

2.2 State of the art

Honeycomb structures have always attracted the man both from a artistic point of view and an applicative, practical one. The first attempt of human to copy the perfection of

the bees' honeycomb, for decorative purposes, dates more than 3000 years back (Sacks [2014]). First scientists to be interested in the properties of honeycombs have been Galileo Galilei (Galilei [1638]), Robert Hooke and Charles Darwin (Darwin and Bynum [2009]), who described their characteristics of being very light and and resistant and of being able to optimize the amount of wax to be used by the insects.
Then, in 1914, honeycombs found their first application for structural purposes, when Höfler proposed them to build aircraft floor panels (Höfler and Renyi [1914]). From that moment they have become of great interest for engineers and scientists, who started to study the behaviour of such sandwich panels with honeycomb cores, made of different materials like paper, metal, thermoplastic, ceramics or composites (Fahey et al. [1961], Herbert [1960], Bardhan [1997], Vinson [1986]). In 1999, Hales proved that the bees' honeycomb is the most stable in nature, providing the maximal cell space with the minimal use of wax (Hales [2001]). This property makes them extremely appealing not only for engineering applications but also for medicine or biology (George et al. [2008], Tejavibulya et al. [2011]), if one considers them on smaller dimensions (nanometers scale).
As concerning engineering applications, in particular structural, architecture or aviation ones, different cell shape can be considered, based on the specific behaviour that one wants to obtain: for example, hexagonal, square and triangular shapes are all very resistant in supporting shear loads, while only the first two are also good at heat transfer (Wadley [2006], Hohe and Becker [1999], Gu et al. [2001]). In Torquato et al. [1998], an interesting analysis on the mechanical and transport properties of honeycomb structures with different cell shapes is made, while in Zhu and Mills [2000] a theoretical analysis for different core materials is made, based on the compression behaviour of the cellular solid.
As outcome of all these studies and many others (see also Wang and McDowell [2005], Kim and Christensen [2000]) the factors that mainly influence the mechanical response of honeycombs, are the material, the topology of the cell and the relative density. To test those properties, different kinds of experiments have been conducted both for in-plane and out-of-plane characteristics: for example in Papka and Kyriakides [1994, 1998a,b, 1999a] experimental results for in-plane crushing of honeycomb under uniaxial or biaxial loading conditions can be found, while in Foo et al. [2007], failure modes under tension are studied. Instead, in Pan et al. [2006], Grove et al. [2006], Hong et al. [2006] out-of-plane shear and compression tests are performed. Analytical and finite element results can be found in Pan et al. [2008] where out-of-plane shear is studied, or in Petras and Sutcliffe [1999], Alonso and Fleck [2009], Masters and Evans [1996] where also in-plane failure modes are considered.
During the work, more references will be given, based on the problem that we will be facing step by step. For a general, exhaustive review on honeycomb, see also Zhang et al. [2015], Wadley [2006].

2.3 Manufacturing and applications

2.3.1 Manufacturing

Since the last century, many different technologies to produce honeycomb structures have been developed (Du et al. [2012], Dempsey et al. [2005], Bitzer [2012]). Based on the final use that a honeycomb panel is destined to, and on the material used to produce it, there are several different ways of manufacturing such structures: corrugation, expansion, continuous production (see Figure 2.1), injection moulding or casting and extrusion.

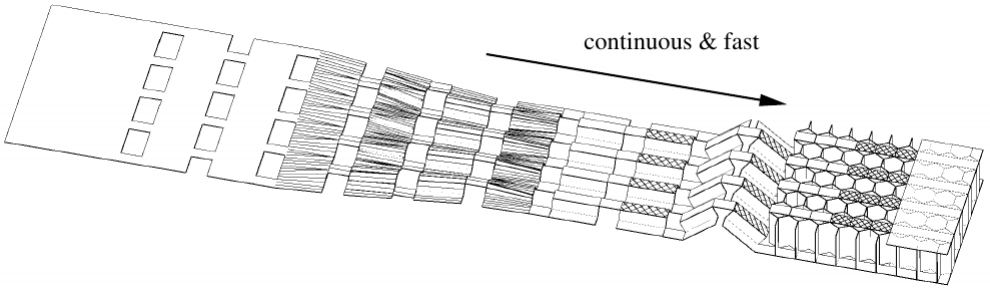

Figure 2.1: Manufacturing honeycombs through the continuous folding method (Pflug et al. [1999])

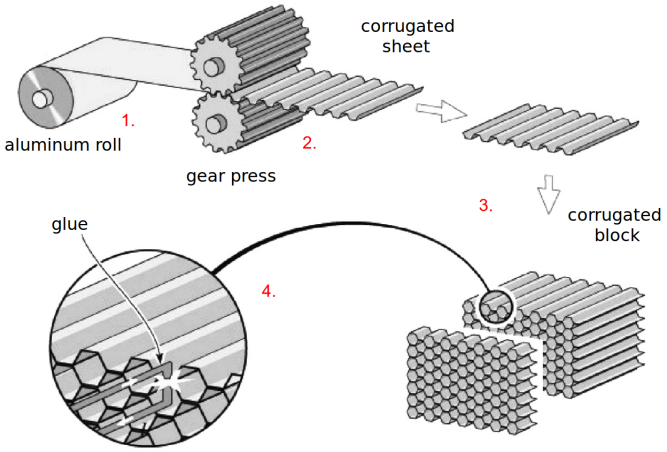

Figure 2.2: Manufacturing honeycombs through corrugation method (Wadley [2006])

We will explain the first two methods, which are, together with the third, the most commonly used to produce metallic honeycomb structures, and the injection moulding process, which is instead used to produce thermoplastic panels.

Corrugation (Figure 2.2)

1. The honeycomb starts as a rolled aluminum (or any metal) foil
2. the foil is gradually unrolled and passed through a gear press which gives it the shapes of half hexagons
3. the foils are cut and put together in a corrugated block
4. the layers are finally glued together.

Expansion (Figure 2.3)

1. The honeycomb starts as a rolled aluminum (or any metal) foil

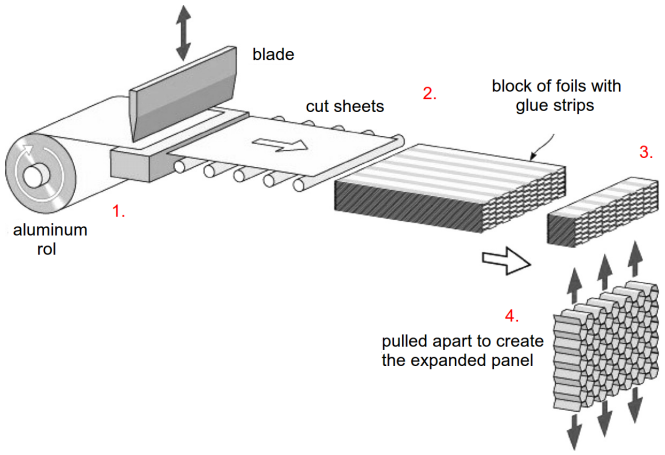

Figure 2.3: Manufacturing honeycombs through expansion method Wadley [2006]

2. the foil is gradually unrolled, cut and adhesive strips are applied to the obtained sheets
3. the foils are immediately glued together and then sliced
4. each slice is finally pulled apart to expand and create the panel.

In both methods, different ways of gluing the layers together can be used, based on the temperatures that the panel has to withstand. These are: adhesive and diffusion bonding, resistance welding, brazing and thermal fusion. The most commonly used is the adhesive bonding, which is cheap but still can resist to temperatures around 390 centigrades. The others are more expensive and are used in more peculiar applications, in the case the panel has to withstand temperatures above 400 centigrades.

Injection moulding (Figure 2.4)

1. Loading and melting: a screw gets the granulated material, which is loaded from a hopper on the top of the machine. The material is pushed and accumulated to the tip of the machinery and melted through heaters, during this process
2. the two parts of the mould are blocked together at the end of the barrel, where the plastic material is collected
3. a hydraulic pump pushes the melt through a sprue, into the pre-warmed mould (heating the mould prevents the early solidification of the material)
4. a lower pressure is kept during the cooling process in order to fill completely the mould when the material shrinks
5. pressure is released and the complete cooling of the mould is waited before its removal[1]
6. the mould is opened and the structure is removed.

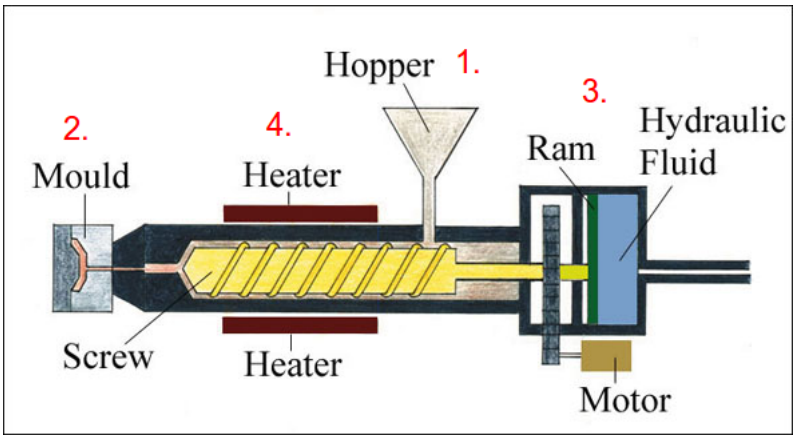

Figure 2.4: Manufacturing honeycombs through injection moulding method (http://www.technologystudent.com/watt/wattex.htm)

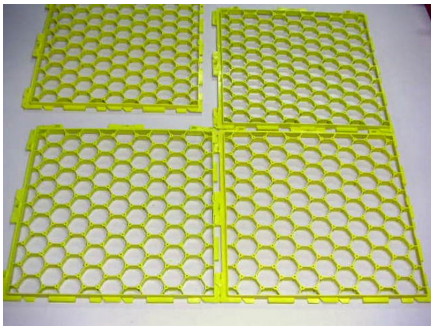

Figure 2.5: Polyethylene honeycomb structure (http://www.3cinterglobal.com/Plastics.htm)

Notice that this process is more resource and cost efficient than the previous ones. With injection, the structure obtained can be considered perfectly regular (see Figure 2.5), since there is not the double thickness of the wall where the metal sheets are glued together. For any desired specific characteristic that the core needs to have, it is sufficient to produce one mould, and used for the production of the panels.

For more details about manufacturing processes the reader could refer to Wadley [2006] and Bitzer [2012].

2.3.2 Applications

Thanks to their peculiar properties, honeycomb structures are widely used in many different applications. Indeed they are very light, but still sufficiently strong structures. Their composition allows the minimization of the weight and the material used to build them, still giving them the property of being shock resistant and efficient at absorbing energy. All this, makes such composite structures extremely appealing from an engineering point of view (Seepersad et al. [2004], Wadley [2006], Davalos et al. [2001]). Depending on the material used to build the core of the panel, honeycomb structures get

[1] This would be the ideal procedure. In reality complete cooling is not waited in order to increase the production and, sometimes, to obtain different polymeric microstructures.

different properties and therefore, different application areas. For example, metallic core honeycombs, are mainly used for structural applications in aircrafts (see Figure 2.6a), buildings, cars and so on. In particular, in aeronautics and aerospace applications, they are used to build secondary structures, which are important because they prevent the crushing of the part in case of failure.
Paper cores, instead, are used for packaging proposal (Figure 2.6b) and transport applications.
Since they are not completely filled by the material, thermoplastic honeycomb panels are used for thermal insulation, buoyancy (Figure 2.6f), and fluid directing (Chochua et al. [2002]), in addition to structural applications.
A part from the aforementioned classical uses, honeycombs cores, have recently found more modern applications: thanks to their shock absorbing capacity, they are employed in car components (Figure 2.6c), sportsgear and sport shoes (Figure 2.6d). Another important application, which is recently rising, is in bio-medicine, where the structure is made by bio-material, and is used in particular for replacing tissues, like bone (Figure 2.6e), liver or heart tissues (Engelmayr Jr et al. [2008], George et al. [2008], Gmeiner et al. [2015]).
A deep understanding of how these structures work is therefore necessary, in order to improve and optimize their use in all the aforementioned applications.

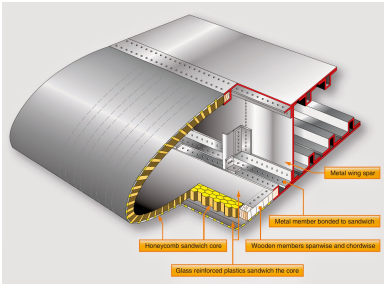

(a) Honeycomb composition of an aircraft wing

(b) Paper honeycomb panels used for packaging

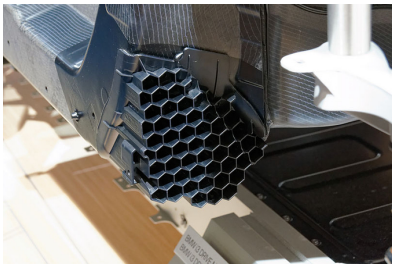

(c) Structure for crash absorption of a car

(d) Sole of a training shoe made of honeycomb for shock absorption

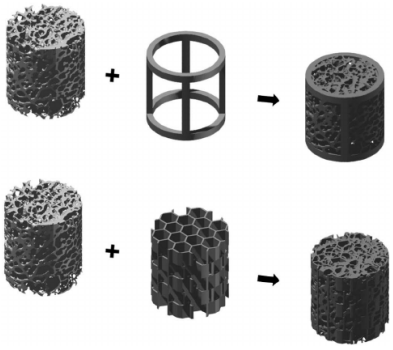

(e) Bone prosthesis made by shifted honeycomb structure (see Gmeiner et al. [2015])

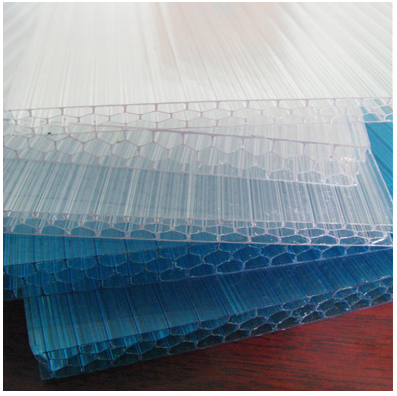

(f) Plastic honeycomb panel

Figure 2.6: Applications of different material honeycomb sutructures

Chapter 3

Mechanics

3.1 Introduction

The subject of mechanics has its origins with the Greeks way before A.D. 0. After a big gap in science (see Russo [2013]), then, scientists like Leonardo da Vinci and Galileo Galilei re-started the study of the subject, examining and describing simple objects and structures, followed by Robert Hooke, Isaac Newton, Daniel Bernoulli and Leonhard Euler who built the theoretical basis of continuum mechanics. Researchers like Cauchy, Navier, Timoshenko, Cosserat (see the classic works Cosserat et al. [1909], Timoshenko [1953], Timoshenko and Woinowsky-Krieger [1959]) and many others, gave the most contribution in developing the theories and models which are still now studied and used by mathematicians, physicists and engineers, not only for applications aimed in building structures or means of transport but also for economics, biology and social behaviours. The pioneering works of Piola, Kirchhoff, Toupin, Germain and Mindlin then introduced a new theory for continuum mechanics, more general, and able to describe the behaviour of complex materials, microstructured, such as fiber reinforced materials or foams (see Piola [1833], Toupin [1962], Mindlin [1964, 1965]). This theory is still an open subject and it is being recently applied to structures which are arising thanks to new technologies such as 3D printing, electro-spinning or foaming. In this chapter we try to briefly summarize the principles of classical continuum mechanics. We will introduce kinematics and dynamics of deformable bodies, present the principles of elasticity and plasticity with an overview on both small and large deformations.

3.2 Kinematics

A material body B is considered as consisting of material particles occupying a region of the Euclidean space. In order to describe the motion of such a body, we need to choose a reference placement at a certain time t_0, in which the vector $\mathbf{X}$ is the position vector of a material point P (see Figure 3.1). Every material point will correspond to its respective one in the actual or current placement, whose position vector will be $\mathbf{x}$. Let us consider a map $\mathbf{f}$ such that:

$$\mathbf{x} = \mathbf{f}(\mathbf{X}, t), \tag{3.1}$$

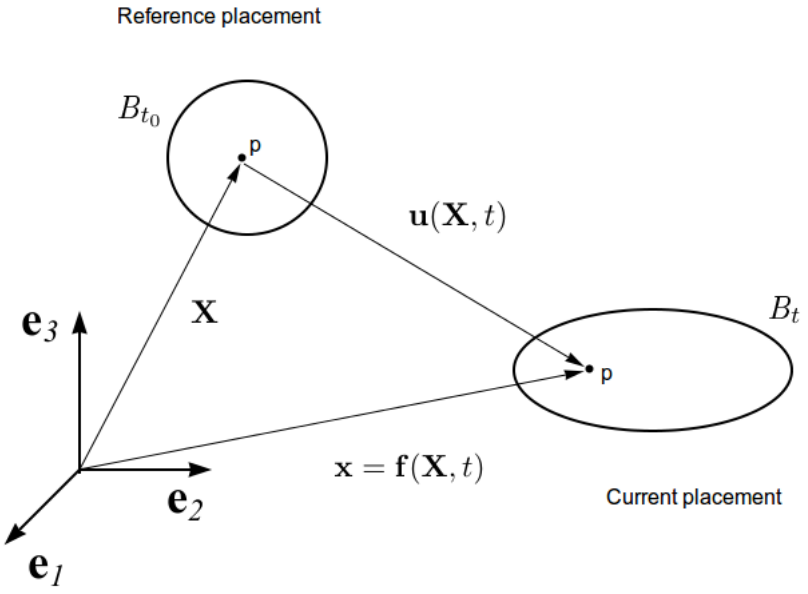

Figure 3.1: Material body in its reference and current configurations

i.e. $\mathbf{f}$ maps the position vector $\mathbf{X}$ of the reference placement, into the current position vector $\mathbf{x}$ at time t. Since at the reference time t_0 : $\mathbf{X} = \mathbf{f}(\mathbf{X}, t_0)$, we can define the displacement vector as:

$$\mathbf{u}(\mathbf{X},t) := \mathbf{f}(\mathbf{X},t) - \mathbf{f}(\mathbf{X},t_0) = \mathbf{f}(\mathbf{X},t) - \mathbf{X}. \tag{3.2}$$

The invertibility of the map $\mathbf{f}$ guarantees that at a fixed time t two material points do not occupy the same spatial point. This allows us to define physical quantities, ϕ, in its material coordinates and then transform them into spatial ones:

$$\begin{aligned}\phi_L(X_1,X_2,X_3,t) &= \phi_L(f_1^{-1}(x_1,x_2,x_3,t), f_2^{-1}(x_1,x_2,x_3,t), f_3^{-1}(x_1,x_2,x_3,t), t)\\ &=: \phi_E(x_1,x_2,x_3,t),\end{aligned} \tag{3.3}$$

where ϕ_L is the material or Lagrange representation, and ϕ_E is the spatial or Eulerian representation.
In order to describe the deformations of a body, the spatial derivatives of $\mathbf{x}$ and $\mathbf{u}$ have to be used. With all these ingredients, we can define the displacement gradient $\mathbf{H}$ and the deformation gradient $\mathbf{F}$:

$$\begin{aligned}\mathbf{F}(\mathbf{X},t) &:= \operatorname{Grad}\mathbf{f}(\mathbf{X},t) = \frac{\partial f_i}{\partial X_j}\mathbf{e}_i \otimes \mathbf{e}_j\\ \mathbf{H}(\mathbf{X},t) &:= \operatorname{Grad}\mathbf{u}(\mathbf{X},t) = \frac{\partial u_i}{\partial X_j}\mathbf{e}_i \otimes \mathbf{e}_j\\ &= \operatorname{Grad}(\mathbf{f}(\mathbf{X},t) - \mathbf{X}) = \operatorname{Grad}(\mathbf{f}(\mathbf{X})) - \operatorname{Grad}\mathbf{X} = \mathbf{F}(\mathbf{X},t) - \mathbf{I},\end{aligned} \tag{3.4}$$

where Grad stands for the derivative with respect to the material coordinates X_i. Notice that $\mathbf{F}$ contains both rigid body rotations and strains. Therefore, in order to exclude the

formers, we can write the deformation gradient in its polar decomposition:

$$\mathbf{F} = \mathbf{R} \cdot \mathbf{U} = \mathbf{V} \cdot \mathbf{R}, \tag{3.5}$$

where $\mathbf{U}$ and $\mathbf{V}$ are positive definite, symmetric, right and left (respectively) stretch tensors and $\mathbf{R} \in Orth^+$ is an orthogonal tensor. Then we can define the right and left Cauchy-Green tensors respectively as

$$\begin{aligned} \mathbf{C} &:= \mathbf{U}^2 = \mathbf{F}^T \cdot \mathbf{F} \\ \mathbf{B} &:= \mathbf{V}^2 = \mathbf{F} \cdot \mathbf{F}^T. \end{aligned} \tag{3.6}$$

A straightforward strain measure in the reference placement is Green's tensor, defined as

$$\mathbf{E}^G := \frac{1}{2}(\mathbf{F}^T \cdot \mathbf{F} - \mathbf{I}) = \frac{1}{2}(\mathbf{H} + \mathbf{H}^T + \mathbf{H}^T \cdot \mathbf{H}), \tag{3.7}$$

representing the change of angle between two line elements (for further details see Bertram and Glüge [2015]). Notice that $\mathbf{E}^G$ is not linear in $\mathbf{H}$ and, therefore, neither in $\mathbf{u}$. If we want to stick to linearity, we have to linearise Green's strain tensor, obtaining

$$\mathbf{E} := \frac{1}{2}(\mathbf{H} + \mathbf{H}^T) = \frac{1}{2}(\frac{\partial u_i}{\partial X_j} + \frac{\partial u_j}{\partial X_i})\mathbf{e}_i \otimes \mathbf{e}_j = \varepsilon_{ij}\mathbf{e}_i \otimes \mathbf{e}_j, \tag{3.8}$$

i.e. the symmetric part of the displacement gradient $\mathbf{H}$ (remember that this theory is valid only for small deformations).
The trace, or the spherical part, $\mathbf{E}^\circ = \frac{1}{3}\mathrm{tr}(\mathbf{E})\mathbf{I}$, of the (infinitesimal) strain tensor represents the dilatations (volumetric change) of the body, while its deviatoric part, $\mathbf{E}' = \mathbf{E} - \mathbf{E}^\circ$, represents the isocoric deformations or, in other words, the distortions.
In many cases, especially in the context of large deformations or viscous materials, the velocity at which the process is performed influences the result. Therefore we need to define the velocity gradient as follows:

$$\mathbf{L} := \mathrm{grad}\,\mathbf{v} = \frac{\partial \mathbf{v}(\mathbf{x}, t)}{\partial \mathbf{x}} = \dot{\mathbf{F}} \cdot \mathbf{F}^{-1}. \tag{3.9}$$

With the additive decomposition of $\mathbf{L}$ we can finally obtain the rate of deformation tensor:

$$\mathbf{D} = \frac{1}{2}(\mathbf{L} + \mathbf{L}^T) = \mathbf{D}^T, \tag{3.10}$$

i.e. its symmetric part, and the spin tensor or vorticity

$$\mathbf{W} = \frac{1}{2}(\mathbf{L} - \mathbf{L}^T) = -\mathbf{W}^T, \tag{3.11}$$

i.e. $\mathbf{L}$'s skew part.
As a remark, it is necessary to point out that the strain tensor is by no means unique. Indeed there exist many other strain tensors, like the ones after Alamansi, Biot or Henky (see Bertram [2015]).

3.3 Balance equations

3.3.1 Classification of forces

As classical Newton and Euler laws state, the motion of a body is due to externally applied forces. These can be divided into:

body forces or volume forces, which are indeed related to the volume or the mass of the body, as, for example, the weight or potential forces

surface forces or contact forces, which act on surfaces, either external or internal to the body.

To better understand this latter category, for external surface forces we mean the one which result from contact with other bodies. On the other hand, the internal surface forces are the ones which we find when cutting imaginary (Cauchy's cut) a body in two. If we assume that the contact forces are uniformly distributed into the body, we can define the stress vector, $\mathbf{t}(\mathbf{n}, \mathbf{x}, t)$ and the Cauchy's stress tensor as

$$\mathbf{t}(\mathbf{n}, \mathbf{x}, t) = \mathbf{T} \cdot \mathbf{n}, \tag{3.12}$$

which is a nine components tensor, describing a particular configuration of the deformed body at time t. Notice that we can write the stress tensor in its spectral form as follows

$$\mathbf{T} = \sigma_{ij} \mathbf{e}_i \otimes \mathbf{e}_j, \tag{3.13}$$

where σ_{ij} are the principal stresses and $\mathbf{e}_i$ is an orthonormal basis, such that, when $i = j$ all shear stresses are zero.
Like in the case of $\mathbf{E}$ we can decompose the stress tensor into

$$\begin{aligned} -p\mathbf{I} = \frac{1}{3}\mathrm{tr}(\mathbf{T})\mathbf{I} = \frac{1}{3}(\sigma_1 + \sigma_2 + \sigma_3)\mathbf{I} \quad &\text{spherical part (pressure)} \\ \mathbf{T}' := \mathbf{T} - \frac{1}{3}\mathrm{tr}(\mathbf{T})\mathbf{I} \quad &\text{deviatoric part.} \end{aligned} \tag{3.14}$$

As for the previous section, it is important to remark the existence of other definitions for the stress tensor as, for example, the ones by Piola and Kirchhoff (see sec. 3.3.2, 3.4.1).

3.3.2 Balance laws

As mentioned before, in continuum mechanics we can write balance relations which can involve either the entire body or a subsection of it. Therefore integral relations are necessary, both on the surface and on the volume. The relation between the two integral forms are given by Gauss theorem. In this way we can obtain balance laws of mass, momentum and moment of momentum, from the spatial point of view. These can be written, in their differential form, as:

$$\begin{aligned} \dot{\rho} + (\rho\nabla) \cdot \dot{\mathbf{u}} = 0 \quad &\text{Balance of mass} \\ \rho\ddot{\mathbf{u}} - \nabla \cdot \mathbf{T} - \rho\mathbf{b} = \mathbf{0} \quad &\text{Euler's first law of motion} \\ \mathbf{T} = \mathbf{T}^T \quad &\text{Euler's second law of motion,} \end{aligned} \tag{3.15}$$

where ρ and $\dot{\rho}$ are the body density and its material derivative with respect to time, and $\mathbf{b}$ is a body force density.
If we pull-back the previous relations to the reference placement, we can write them as:

$$\begin{aligned} \det(\mathbf{F}) = J = \frac{\rho_0}{\rho} \\ \rho_0 \ddot{\mathbf{u}} - \nabla_0 \cdot \mathbf{P}_I^T - \rho_0 \mathbf{b} = \mathbf{0} \\ \mathbf{F} \cdot \mathbf{P}_I^T = \mathbf{P}_I \cdot \mathbf{F}^T, \end{aligned} \tag{3.16}$$

where $\mathbf{P}_I$ is the first Piola-Kirchhoff stress tensor defined as

$$\mathbf{P}_I = J\mathbf{T} \cdot \mathbf{F}^{-T}, \tag{3.17}$$

and ρ_0 is the mass density in the reference configuration.

3.4 Constitutive laws

As the reader may have noticed, up to now we just mentioned general laws and mathematical relations, which can be applied to any body. Moreover, if we consider the 3D case, we can count 12 unknowns, against 6 equations given by the balance laws. We still miss 6 equations, exactly those equations which we need to characterize specifically the behaviour of the material we are dealing with. These are called constitutive laws, and will express the relations between the kinematical variables (like $\mathbf{F}$ or $\mathbf{E}$) and the dynamical ones (like $\mathbf{T}$ or $\mathbf{P}_I$). Nevertheless, these laws have to undergo some common principles like the one of determinism, of local action and invariance under superimposed rigid body motion.

3.4.1 Elasticity

One of the oldest, easiest but still most used constitutive relation is the linear elastic law. It was formulated by Hooke in 1676. He found linear Force-Displacement relations to be structure independent, concluding that it had to be a material property. Therefore, Hooke's law states the linear dependence between stresses and strains. We can write it through the linearised strain tensor $\mathbf{E}$ and Cauchy's stress tensor as

$$\mathbf{T} = \mathbb{K}[\mathbf{E}], \tag{3.18}$$

where $\mathbb{K}$ is the 4th-order elasticity tensor.
Another form of the previous law, which lives entirely in the reference placement, is written by means of the second Piola-Kirchhoff stress tensor. It states that the 2^{nd} Piola-Kirchhoff stress tensor is a function of the Cauchy-Green tensor (3.7)

$$\mathbf{P}_{II} = f(\mathbf{C}) = \mathbb{K}\left[\frac{1}{2}(\mathbf{C} - \mathbf{I})\right], \tag{3.19}$$

where

$$\mathbf{P}_{II} = J\mathbf{F}^{-1} \cdot \mathbf{T} \cdot \mathbf{F}^{-T} \tag{3.20}$$

is the 2^{nd} Piola-Kirchhoff stress tensor, which relates forces to areas, both in the reference placement. Notice that the tetrad $\mathbb{K}$ has, in principle, 81 entries, which are reduced to 21

independent components, thanks to major symmetry and left and right subsymmetries. These can be easily represented if one uses the Voigt notation which allows to write the stiffness tensor as a 6 by 6 matrix:

$$\mathbb{K} = K_{ijkl}\mathbf{e}_i \otimes \mathbf{e}_j \otimes \mathbf{e}_k \otimes \mathbf{e}_l = K_{\alpha\beta}\mathbf{B}_\alpha \otimes \mathbf{B}_\beta, \tag{3.21}$$

with

$$\begin{aligned} \mathbf{B}_1 &= \mathbf{e}_1 \otimes \mathbf{e}_1, \quad \mathbf{B}_4 = \frac{\sqrt{2}}{2}(\mathbf{e}_2 \otimes \mathbf{e}_3 + \mathbf{e}_3 \otimes \mathbf{e}_2) \\ \mathbf{B}_2 &= \mathbf{e}_2 \otimes \mathbf{e}_2, \quad \mathbf{B}_5 = \frac{\sqrt{2}}{2}(\mathbf{e}_1 \otimes \mathbf{e}_3 + \mathbf{e}_3 \otimes \mathbf{e}_1) \\ \mathbf{B}_3 &= \mathbf{e}_3 \otimes \mathbf{e}_3, \quad \mathbf{B}_6 = \frac{\sqrt{2}}{2}(\mathbf{e}_1 \otimes \mathbf{e}_2 + \mathbf{e}_2 \otimes \mathbf{e}_1). \end{aligned} \tag{3.22}$$

The stiffness matrix also tells us the symmetry class of the material, through the number of independent components contained (see chapter 4).

3.4.2 Plasticity

As in the classical theory for plasticity, we assume the decomposition of the strains $\mathbf{E}$ in its elastic and plastic parts:

$$\mathbf{E} = \mathbf{E}_e + \mathbf{E}_p. \tag{3.23}$$

Then, in order to model the plastic behaviour of any material, three main ingredients are necessary:

Elastic ranges within which the material presents elastic behaviour

Yielding and plastic flow which changes the elastic range

Hardening or softening which changes the yield limit

The boundary of the elastic range, ∂Ela represents the yield surface or yield limit, and could be represented by a tensor function $\Phi(\mathbf{T})$ such that:

- If $\Phi(\mathbf{T}) < 0$ then the material is still in the elastic range
- If $\Phi(\mathbf{T}) = 0$ the material is yielding
- If $\Phi(\mathbf{T}) > 0$ the material is out of the elastic range

Notice that the third case can not really be considered (unless one is dealing with some particular viscous material). Indeed, when the stress state reaches the yielding of the material, it pushes it forward, deforming plastically the body, and, at the same time, shifting its elastic range.

Yield limits

In order to write a yield criterion it is helpful to define an equivalent stress $\sigma_{eq}(\mathbf{T})$ which we will compare with the critical one σ_y, the yield stress. Then, the yield limit function,

in the dynamic variables Φ, will be:

$$\Phi(\mathbf{T}) = \sigma_{eq}(\mathbf{T}) - \sigma_y \tag{3.24}$$

In literature, there exist a huge amount of yield criteria, proposed by different scientists like Rankine, Mohr, Drucker, Prager, Hill and many others. Here we limit ourselves to the explanation of two of the most important yield criteria:

Tresca or maximum shear yield criterion: it compares the maximum shear stress τ_{max} with the one appearing in a simple tension stress at yielding

$$\Phi(\mathbf{T}) = \tau_{max}^2 - \tau_y^2 = \frac{1}{2}(\sigma_{max} - \sigma_{min})^2 - \tau_y^2. \tag{3.25}$$

Von Mises yield criterion, based on the J_2 theory: the equivalent stress depends only on the norm of the stress deviator, i.e. on its second invariant

$$\Phi(\mathbf{T}) = 3J_2 - \sigma_y^2 = \frac{3}{2}\mathbf{T}' \cdot\cdot \mathbf{T}' - \sigma_y^2 \tag{3.26}$$

Notice that both the presented models are independent from hydrostatic pressure, which motivates the dropping of the first invariant[1] ($J_1 = \mathrm{tr}\mathbf{T}$).

Plastic flow and hardening

As we mentioned in section 3.4.2, in order to have plastic deformations of the body, the state of the stress must stay on the yield surface. This is ensured by two conditions:

- The yield criterion is fulfilled
$$\Phi(\mathbf{T}) = 0 \tag{3.27}$$
- The loading condition is fulfilled
$$\dot{\Phi}_D \,|_{\mathbf{E}_p} = \frac{\partial \Phi}{\partial \mathbf{T}} \,|_{\mathbf{E}_p} \cdot\cdot\, \dot{\mathbf{T}} > 0 \tag{3.28}$$

When the two conditions hold, plastic flow occurs and, therefore, we need new relations to describe how the elastic ranges deform or, in other words, how the yield limit evolves. The general flow rule can be written as

$$\mathrm{d}\mathbf{E}_p = \mathrm{d}\lambda\, \mathrm{d}\mathbf{G}, \tag{3.29}$$

where $\mathrm{d}\mathbf{E}_p$ is the plastic strain increment, $\mathrm{d}\lambda$ is a plastic multiplier, and $\mathrm{d}\mathbf{G}$ is the plastic flow direction. Many material behaviours can be collected under the non-associative flow rule

$$\mathrm{d}\mathbf{E}_p = \mathrm{d}\lambda \frac{\partial q}{\partial \mathbf{T}}, \tag{3.30}$$

[1] This is incompressible plasticity and, as we will see later, it does not work for the effective model of the microstructured body.

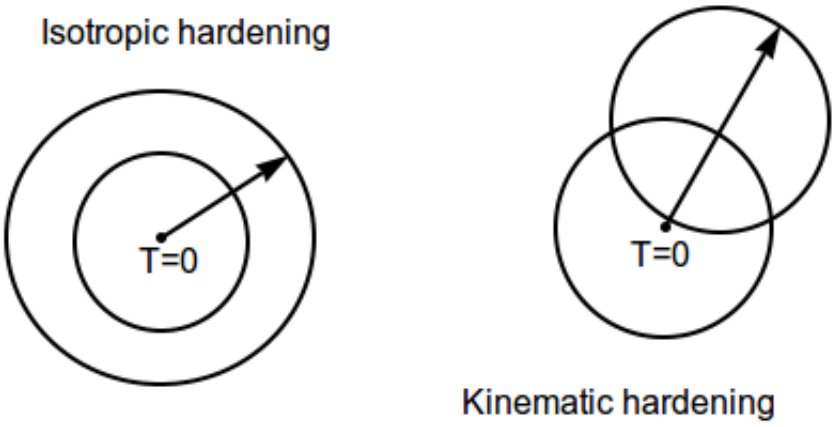

Figure 3.2: Evolution of the yield surface with isotropic and kinematic hardening

where q is a scalar function, called plastic potential. In particular, if q coincides with the yield function Φ, we get the associative flow rule, or normality rule

$$\mathrm{d}\mathbf{E}_p = \mathrm{d}\lambda \frac{\partial \Phi}{\partial \mathbf{T}}, \tag{3.31}$$

being $\partial\Phi/\partial\mathbf{T}$ normal to the yield surface.
Hardening (or softening) is introduced mainly by the accumulated plastic strain $\epsilon = \int \mathrm{d}\lambda = \int \lambda \mathrm{d}t$. The most simple models for hardening rules are **kinematic** and **isotropic** hardening. When we consider **kinematic hardening**, the yield surface is rigidly shifted in the stress space, whereas in **isotropic hardening**, the yield surface is blown up isotropically by some linear factor (see Figure 3.2).

Drucker's Postulate

In 1959 Daniel C. Drucker wrote a postulate with the aim of defining stable materials (see Drucker [1957] and also Drucker [1963]). He states that in order for the material to be stable, the following inequality must hold:

$$\oint (\mathbf{T} - \mathbf{T}_A) \cdot\cdot \, \mathrm{d}\mathbf{E} \geq 0, \tag{3.32}$$

where the integral is made on the whole cyclic process, which starts from the stress state $\mathbf{T}_A$. This must hold both for elastic and plastic processes (although not exceeding too much the yield stress). If we consider $\mathbf{T}_A = 0$, after some manipulation of (3.32) (see Bertram and Glüge [2015]) we get

$$(\mathbf{T}) \cdot\cdot \, \mathrm{d}\mathbf{E}_p \geq 0. \tag{3.33}$$

and it can be interpreted physically as the energy dissipated during the process.
Drucker's postulate has three main consequences, which one could use to ensure the stability of the studied material:

- the yield surface in the stress space must be convex

- associated flow rule (or normality) must hold
- $\mathrm{d}\mathbf{T} \cdot\cdot \mathrm{d}\mathbf{E} \geq 0$ must hold

Therefore, materials which present softening, buckling of the microstructure, non-convex yield surfaces or non-associative flow rules, are considered as unstable and, indeed, they often present difficulties when driving numerical analysis. We will encounter such a material behaviour during our work and we will deal with it using different approaches trying to overcome the instabilities in the most efficient way.

Chapter 4

Preliminary considerations and simulations

4.1 Introduction

In this chapter, we report some preliminary considerations and results on honeycomb structures. Approaching honeycombs for the first time, we make a short review of Gibson and Ashby's work on the small strain linear elastic problem and make some observation to support their results. Then, we set a boundary value problem (BVP) using the software ABAQUS, and perform simulations on a 10×10 cells structure, in order to see if we are able to reproduce the basic properties of a real one[1]. In particular, we would like to see the collapsing of rows and the corresponding stress-strain curve.

4.2 Considerations on the isotropy of the linear elastic behaviour of honeycombs

4.2.1 Gibson and Ashby's argument

Lorna J. Gibson and Michael E. Ashby in 1997 published a book called "Cellular solids" (see Gibson and Ashby [1997]). This is a collection of studies about all cellular solids, from polymeric foams to wood and so on. A couple of chapters of that book are entirely dedicated to honeycomb structures, which are, in fact, closed cells cellular solids. Here we report the main formulas, which may turn out to be useful during our next analysis. We will focus exclusively on the linear elastic behaviour. Let us consider the unit cell in fig 4.1. Notice that, in general, $h \neq l$, γ can be arbitrary and that the thickness t is doubled in real alluminum honeycombs core panels because of their fabrication process (see chapter 2).
The first important parameter is the relative density

$$\frac{\rho^*}{\rho_m} = \frac{t/l(h/l+2)}{2\cos\gamma(h/l+\sin\gamma)} \tag{4.1}$$

[1] As a first attempt we tried to use the software COMSOL with which we captured an unexpected auxetic behaviour of the structure (see Figure 8.2). Then, we switched to ABAQUS in order to have more freedom with the problem settings.

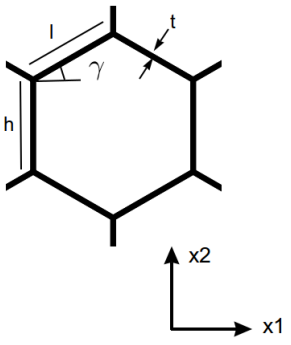

Figure 4.1: Unitary cell of hexagonal shape

where ρ^* is the density of the structure, while ρ_m is the density of the core material. If the relative density is low, also t/l is small so to ensure bending of the beams (in chapter 5 we will see that a higher t/l leads to a negative poisson ratio).
Limiting themselves to small linear elastic deformations, the authors made a force analysis and found the Young's moduli, shear modulus and Poisson's ratios, through balance of forces and moments of momentum:

Young's moduli in directions x_1 and x_2, respectively

$$\begin{aligned} \frac{E_1^*}{E_m} &= \left(\frac{t}{l}\right)^3 \frac{\cos\gamma}{(h/l+\sin\gamma)\sin^2\gamma} \\ \frac{E_2^*}{E_m} &= \left(\frac{t}{l}\right)^3 \frac{h/l+\sin\gamma}{\cos^3\gamma} \end{aligned} \tag{4.2}$$

Poisson's ratios

$$\begin{aligned} \nu_{12}^* &= \frac{\cos^2\gamma}{(h/l+\sin\gamma)\sin\gamma} \\ \nu_{21}^* &= \frac{(h/l+\sin\gamma)\sin\gamma}{\cos^2\gamma} \end{aligned} \tag{4.3}$$

Shear modulus

$$\frac{G_{12}^*}{E_m} = \left(\frac{t}{l}\right)^3 \frac{h/l+\sin\gamma}{(h/l)^2(1+2h/l)\cos\gamma} \tag{4.4}$$

For regular hexagons, where $h = l$ and $\gamma = 30°$ we obtain with easy calculations

Young's moduli

$$\frac{E_1^*}{E_m} = \frac{E_2^*}{E_m} = 2.3\left(\frac{t}{l}\right)^3 \tag{4.5}$$

Poisson's ratios

$$\nu_{12}^* = \nu_{21}^* = 1 \tag{4.6}$$

Shear modulus

$$\frac{G_{12}^*}{E_m} = 0.57\left(\frac{t}{l}\right)^3 = \frac{1}{4}\frac{E^*}{E_m} \tag{4.7}$$

meaning that the regular structure, under small elastic deformations, presents an isotropic behaviour. These formulas will be used later on in order to compute the material parameters for our numerical simulations.

4.2.2 Check of the stiffness matrix

In chapter 3 we just hinted to the material symmetry as the number of independent components of the stiffness matrix.
A simple and intuitive way of defining an isotropic material could be that its material properties are the same in all directions. To be a bit more accurate, let us consider a displacement field $\mathbf{u}(X)$ and a rotation tensor $\mathbf{Q}$, such that

$$\mathbf{u}'(X') := \mathbf{Q} \cdot \mathbf{u}(X) \Leftrightarrow \mathbf{u}(X) := \mathbf{Q} \cdot \mathbf{u}'(X')$$

where the apex $'$ denotes the rotated vector. Using the chain rule we can get the rotated displacement gradient and strain tensor

$$\mathbf{H}' = \mathbf{Q} \cdot \mathbf{H} \cdot \mathbf{Q}^T$$
$$\mathbf{E}' = \mathbf{Q} \cdot \mathbf{E} \cdot \mathbf{Q}^T.$$

Then, an elastic law is symmetric w.r.t. a rotation $\mathbf{Q}$ if

$$\mathbf{T}' = \mathbf{Q} \cdot \mathbf{T} \cdot \mathbf{Q}^T.$$

$\mathbf{Q}$ is a symmetry transformation of $\mathbf{T} = \mathbb{K} \cdot\cdot \mathbf{E}$ if

$$\mathbb{K} \cdot\cdot (\mathbf{Q} \cdot \mathbf{E} \cdot \mathbf{Q}^T) = \mathbf{Q} \cdot (\mathbb{K} \cdot\cdot \mathbf{E}) \cdot \mathbf{Q}^T. \tag{4.8}$$

If we write $\mathbb{K}$ in Voigt notation (see eq. (3.21)) and apply equation (4.8) we get that

$$\mathbb{K} \cdot\cdot \mathbf{E} = \mathbf{Q}^T \cdot (\mathbb{K} \cdot\cdot (\mathbf{Q} \cdot \mathbf{E} \cdot \mathbf{Q}^T)) \cdot \mathbf{Q}$$

for all symmetric tensors $\mathbf{E}$. Hence

$$\mathbb{K} = K_{ijkl} \mathbf{e}_i \otimes \mathbf{e}_j \otimes \mathbf{e}_k \otimes \mathbf{e}_l = K_{ijkl} (\mathbf{Q} \cdot \mathbf{e}_i) \otimes (\mathbf{Q} \cdot \mathbf{e}_j) \otimes (\mathbf{Q} \cdot \mathbf{e}_k) \otimes (\mathbf{Q} \cdot \mathbf{e}_l) = \mathbf{Q} * \mathbb{K} \tag{4.9}$$

where $*$ denotes the Rayleigh product[2]. For a deeper discussion about material symmetries please refer to Bertram and Glüge [2015], Coleman and Noll [1964]. For us it is sufficient to report here the stiffness matrix for isotropic elastic material in the Voigt notation (in the 2D case):

$$\mathbb{k} = \alpha \mathbf{I} \otimes \mathbf{I} + \beta \mathbf{I}_s \Leftrightarrow K_{ijkl} = \alpha \delta_{ij} \delta_{kl} + \beta (\delta_{ik} \delta_{jl} + \delta_{il} \delta_{jk}) = \begin{bmatrix} \alpha + 2\beta & \alpha & 0 \\ \alpha & \alpha + 2\beta & 0 \\ 0 & 0 & \beta \end{bmatrix} \mathbf{E}_i \otimes \mathbf{E}_j \tag{4.10}$$

where δ is the Kronecker delta. Now assume we have a symmetry rotating the structure by $\frac{\pi}{3}$ (fig. 4.2):

$$\mathbf{R}(\frac{\pi}{3}) = \begin{bmatrix} \cos(\frac{\pi}{3}) & -\sin(\frac{\pi}{3}) \\ \sin(\frac{\pi}{3}) & \cos(\frac{\pi}{3}) \end{bmatrix} \mathbf{e}_i \otimes \mathbf{e}_j, \quad i, j = 1, 2$$

[2]The RAYLEIGH product maps all basis vectors of a tensor simultaneously without changing its components

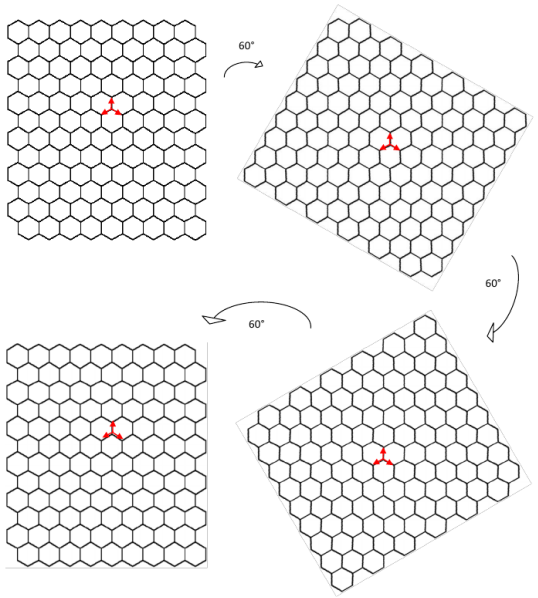

Figure 4.2: Six fold symmetry of the honeycomb structure

and impose the symmetry to the complete stiffness matrix $\mathbb{K}$:

$$\mathbf{R}(\frac{\pi}{3}) * \mathbf{C} = \mathbf{C}' \Leftrightarrow$$
$$C'_{ijkl} = R_{im}R_{jn}R_{ko}R_{lp}C_{mnop}\mathbf{e_i} \otimes \mathbf{e_j} \otimes \mathbf{e_k} \otimes \mathbf{e_l} =$$
$$\begin{bmatrix} c_{2222} & -2c_{1212} + c_{2222} & 0 \\ -2c_{1212} + c_{2222} & c_{2222} & 0 \\ 0 & 0 & c_{1212} \end{bmatrix} \mathbf{E}_i \otimes \mathbf{E}_j.$$

This matrix has the same structure as the isotropic one in equation (4.10) where $\alpha = -2c_{1212}+c_{2222}$ and $\beta = c_{1212}$. Therefore, the 2D hexagonal symmetry implies the isotropy of the stiffness matrix: it is symmetric and has only two independent parameters.

4.3 Simulations in ABAQUS

As we stated in the introduction, we now set a boundary value problem using the FE software ABAQUS. Let us consider the 10×10 cell structure, made of aluminium (for simplicity we use a database material; this simulation is just a representative one, with the aim of reproducing the real qualitative behaviour of a hexagonal cellular structure), of Figure 4.3. Large deformations are allowed and von Mises plasticity is considered.

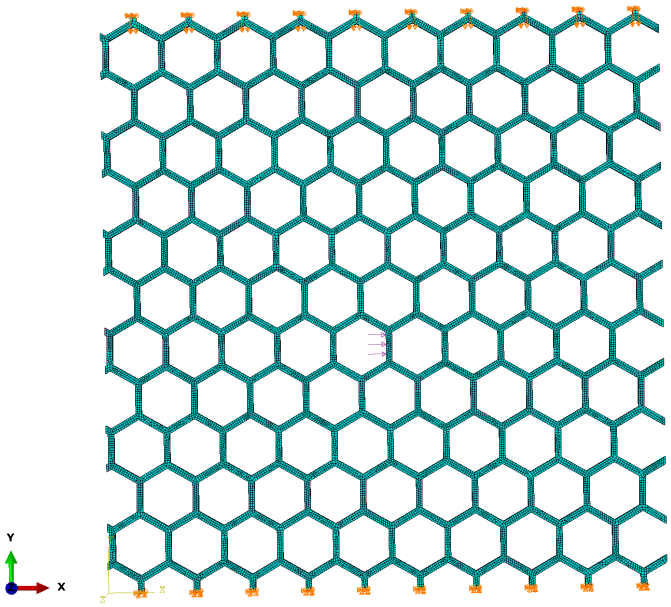

Figure 4.3: 10×10 cell honeycomb structure, with boundary conditions and mesh

The mesh is composed of 3D, 20-node, quadratic, isoparametric elements, with reduced integration. We constrain the bottom of the structure in the x_2 direction, and just a point in the x_1 direction in order to not have rigid body translation. We impose a negative displacement on the top, and periodic boundary conditions at the lateral sides. Because of stability problems, caused by the buckling of the bars, we give a small perturbation, applying some pressure in the x_1 direction on an arbitrary bar (pink arrows in the middle). We expect therefore the localization to start from that row (or its neighbouring ones). Moreover we consider hard, frictionless contact between the faces internal to the cells, in the case they touch. The result is shown in Figure 4.4.

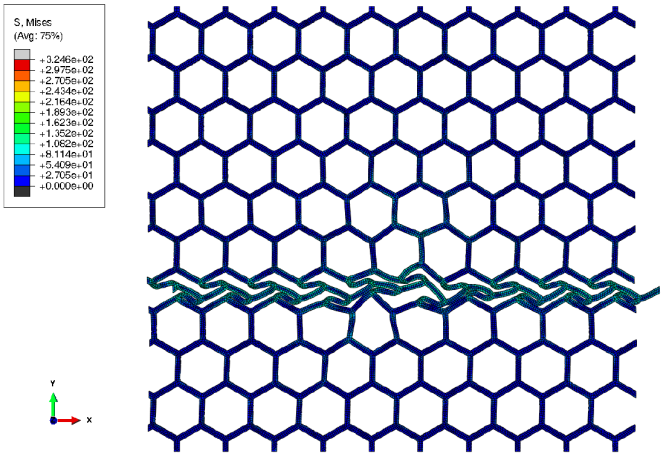

Figure 4.4: 10×10 cell honeycomb structure after a compression test in the x_2 direction.

We also report the stress-strain curve obtained by this test (Figure 4.5).

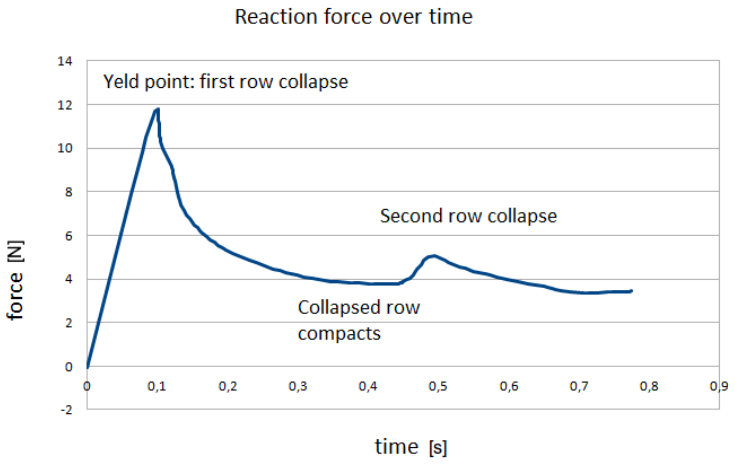

Figure 4.5: Time-force curve of the compression test in Figure 4.4. The time in the abscissa axes is proportional to the strain and the area under the curve to the energy dissipated.

From the Figure we see the initial, linear-elastic behaviour, which ends when the first row collapses. We observe a softening behaviour going on until the collapsed row touches the neighbouring one. Then the force grows again, until a second row starts to fail. This behaviour of softening and hardening, goes on until all the cells have collapsed (see Papka and Kyriakides [1994, 1998a]). After that, the compaction of the structure results in a steep monotonic growth the stress-strain curve. Unfortunately we are not able to observe this behaviour in our simulation, since the code fails to converge because of buckling problems.
This unusual behaviour is what makes such honeycombs panels so interesting: they can undergo large deformations at roughly constant stresses. From a structural engineering point of view it is noteworthy to have a model able to capture this behaviour in order to prevent the collapse, or even to intervene once it has already started. In this work, we try to understand this structures, both from a mechanical and geometrical point of view. It is difficult to find a global solution to the problem, but we achieve to obtain a simple, manageable model able to capture the main features of the structure.

Conclusions

We presented the Gibson and Ashby linear elastic model for regular honeycombs and checked again the isotropy of the structure in this range.
We implemented in ABAQUS a 10×10 cell structure with periodic boundary conditions and saw the rows collapsing and the respective stress-strain curve. We see that although it is possible to implement a real FE model, it is extremely expensive and complex, giving timing and convergence issues. This motivates the development of an effective model, able to give reasonable effective results, removing the complexity of the microstructure.

Chapter 5

Micro- macro-scale: the effective yield limit obtained by the representative volume element

5.1 Introduction

In this chapter, we approach the 2-D in-plane elastic-plastic problem. In particular, we focus on the modelling of the yield limit of the homogenized honeycomb structures. We perform finite element simulations for both elastic and plastic problems, taking into consideration the most convenient representative volume element for our goals. An analytic model, for the so obtained yield limit, is then developed by finding a best fit solution. The parametric study may be useful to properly understand the behaviour of honeycomb structures and can be generalized to other periodic cell structures and cellular solids.

5.2 Numerical study

5.2.1 Structure and representative volume element

As a first step in the investigation of the behaviour of honeycombs we need to set up a numerical laboratory which allows us to test the structure under different loading conditions, boundary constrains, mechanical and geometrical properties. To this aim, we have created, with the support of the codes in ABAQUS and Python, an algorithm that tests the selected elementary component under the desired loading conditions (see Appendix A). In this section, the characteristics of the core material, of the structure itself and of the elementary cell that can fit our needs, are presented.

Let us consider the structure made of aluminium or polyethylene, with an elastic-perfectly plastic material model, and J_2 plastic flow theory. In table 5.1 the used material parameters (Young's modulus E, Poisson's ratio υ, yield strength Y_s) and geometric dimensions of the regular hexagonal shape ($l = h = 1$) shown in Figure 4.1 are reported.
Already in Wilbert et al. [2011], Haghpanah et al. [2013, 2014] different elementary cells are examined to study the response of normal or hierarchical honeycomb structures by

Material	E	υ	Y_s	t	γ
Aluminium	68.97GPa	0.33	292MPa	0.216	$\pi/6$
Polyethylene	0.7GPa	0.3	30MPa	0.216	$\pi/6$

Table 5.1: Material parameters and hexagon dimensions

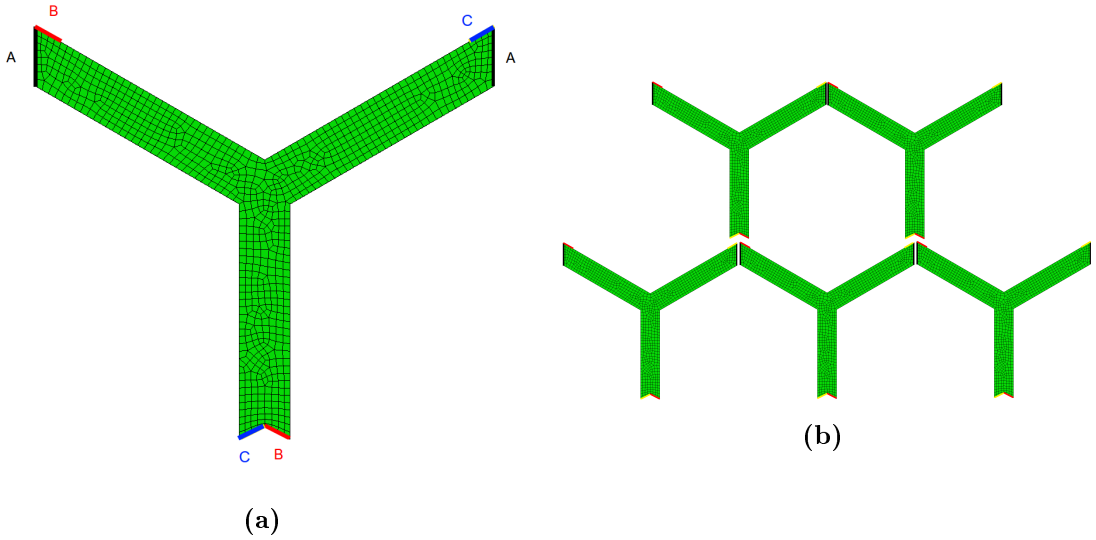

Figure 5.1: (A) Representative volume element with periodic boundary conditions; (B) Macrostructure made of RVE

finite element analysis. For our numerical simulation we select an elementary cell which allows us to reduce the computational time but, at the same time, permits to observe the deformations which the structure undergoes locally, i.e. at the cell level. We need a Representative Volume Element (RVE), the smallest element over which measurements can be made, and that will lead to results that can be extended to the macro-structure (Hill [1963]). It is depicted in Figure 5.1a: this (irreducible) unit cell is the smallest repeatable one. It is clear that any other configuration with this property will fit as well, therefore the minimal RVE is by no means unique. We choose the Y configuration for convenience of visualization and to better observe the deformation behaviour of periodic hexagonal cell. In Figure 5.1, the RVE with the boundary conditions are also shown: we imposed periodic displacements for the parts highlighted with the same colour and named by the same letter. In this way, we can rebuild the whole structure (Figure 5.1b). Notice that by confining ourselves to the smallest possible periodicity frame, we disregard plastic deformations that do not fit into this frame, see, e.g., Miehe et al. [2002]. Thus, we exclude the evolution of localization patterns that do not allow for the chosen frame of periodicity.

5.2.2 Parametrization of the stress state

We already mentioned the advantages that the selected elementary cell presents:

- It is the smallest element which can be extended periodically
- it has a simple geometry

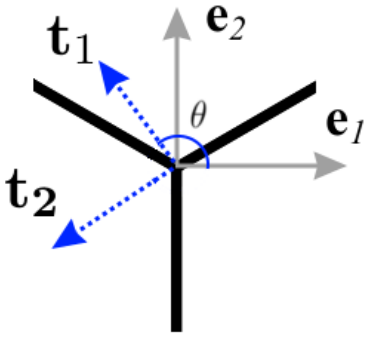

Figure 5.2: Parametrization of the stress state

- it requires little computational time
- it allows the visualization of the local deformations
- it is easy to manipulate.

However, to be able to fully exploit all these properties, we still need an equally simple language, which permits us the imposition of loads to the structure, without loosing the perception of what we are doing, and, at the same time, allows us to easily interpret and handle the results that we obtain. To that purpose we parametrize the plane stress-state by geometric variables and loading parameters, that could help us to keep in mind the structural features and, therefore, to understand the obtained outputs.
Figure 5.2 visualizes the parametrization of the selected stress state: we see in black the structure, in grey the chosen base vectors, and in dashed black the eigendirections of the stress tensor.
Keeping in mind that

$$\mathbf{T} = \begin{bmatrix} T_{11} & T_{12} \\ T_{12} & T_{22} \end{bmatrix} \mathbf{e}_i \otimes \mathbf{e}_j, \tag{5.1}$$

and that its eigenvectors can be written as

$$\mathbf{t_1} = \cos\theta\, \mathbf{e_1} + \sin\theta\, \mathbf{e_2}, \quad \mathbf{t_2} = -\sin\theta\, \mathbf{e_1} + \cos\theta\, \mathbf{e_2}, \tag{5.2}$$

we can write the stress tensor in its spectral form

$$\mathbf{T} = \lambda_1\, \mathbf{t_1} \otimes \mathbf{t_1} + \lambda_2\, \mathbf{t_2} \otimes \mathbf{t_2}, \tag{5.3}$$

where λ_1 and λ_2 are the principal stresses.
In this way we have already found our first parameter θ, which we will therefore call *orientation angle*, that relates the orientation of the imposed load to our structure.
The normalized stress tensor is

$$\mathbf{T}^* = \frac{\lambda_1}{\sqrt{\lambda_1^2 + \lambda_2^2}} \mathbf{t_1} \otimes \mathbf{t_1} + \frac{\lambda_2}{\sqrt{\lambda_1^2 + \lambda_2^2}} \mathbf{t_2} \otimes \mathbf{t_2}. \tag{5.4}$$

We impose the biaxiality condition as a perturbation of the monoaxial load, keeping $\lambda_1^2 + \lambda_2^2 = m^2$. In this way we have the limit cases when $\lambda_i = m$, which is uniaxial

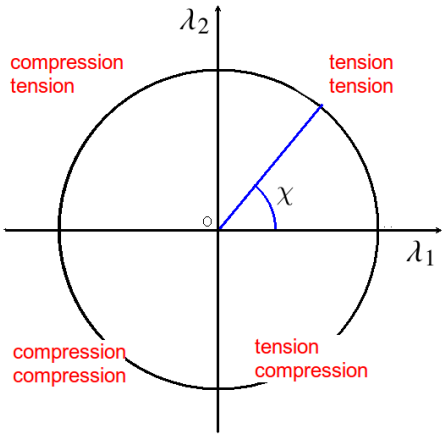

Figure 5.3: Load type depending on the angle χ (which determines the values of λ_1 and λ_2)

loading (in t_i direction), and $\lambda_1 = \lambda_2$ which is biaxial isotropic load. The *magnitude* m will be our second parameter.
The parameters θ and m are more or less straight forward since they come from the geometry and from a measure of the stress tensor.
Now we introduce a third parameter, χ, such that:

$$\lambda_1 = m\cos(\chi), \quad \lambda_2 = m\sin(\chi). \tag{5.5}$$

We call χ *biaxiality measure* angle: $\chi = n\pi/2$ means monoaxial load in $\mathbf{t_1}$ or $\mathbf{t_2}$ direction; $\chi = \pi/4 + n\pi$ means $\lambda_1 = \lambda_2$. With the variation of χ we change the type of load we impose to the structure (Figure 5.3). For the simulations, we discretized χ in steps of $\pi/36$ and θ in steps of $\pi/(6\cdot 20)$, we then increase m until significant plastic deformations are observed.

Preliminary results for the general response of loading can be seen in dell'Isola et al. [2016].

5.2.3 The yield limit on the macro scale

Although such structures present an initial isotropic linear response under small elastic deformations (see Gibson and Ashby [1997]), as soon as large deformations (elastic and plastic) are considered, the behaviour becomes non linear and even anisotropic (Beblo et al. [2015]). The study of the plastic behaviour of such structures is of great interest from an engineering point of view, since honeycombs are mainly used because of their capability of absorbing energy. This property is indeed given from the localization modes occurring during plastic deformations, both for in-plane loads (see for example Papka and Kyriakides [1998a, 1999a, 1998b], Asada et al. [2009], Papka and Kyriakides [1994], Karagiozova and Yu [2008]), and out-of-plane ones (Mohr and Doyoyo [2004a,b], Mohr [2006]). These local modes lead to the plateaux of the stress strain-curves, characteristic of such structures. In order to study the non-classical behaviour which is visible in plastic deformations, as first, one has to properly model the yielding of such structures. After formulating a yield criterion, a plastic flow rule is needed. A comparison between different yield surfaces for different cell forms of the honeycombs is given in Wang and McDowell [2005, 2004] by means of classical balance laws and a yield criterion based on stretching and bending of beams. In contrast to them, we want to formulate a yield criterion based

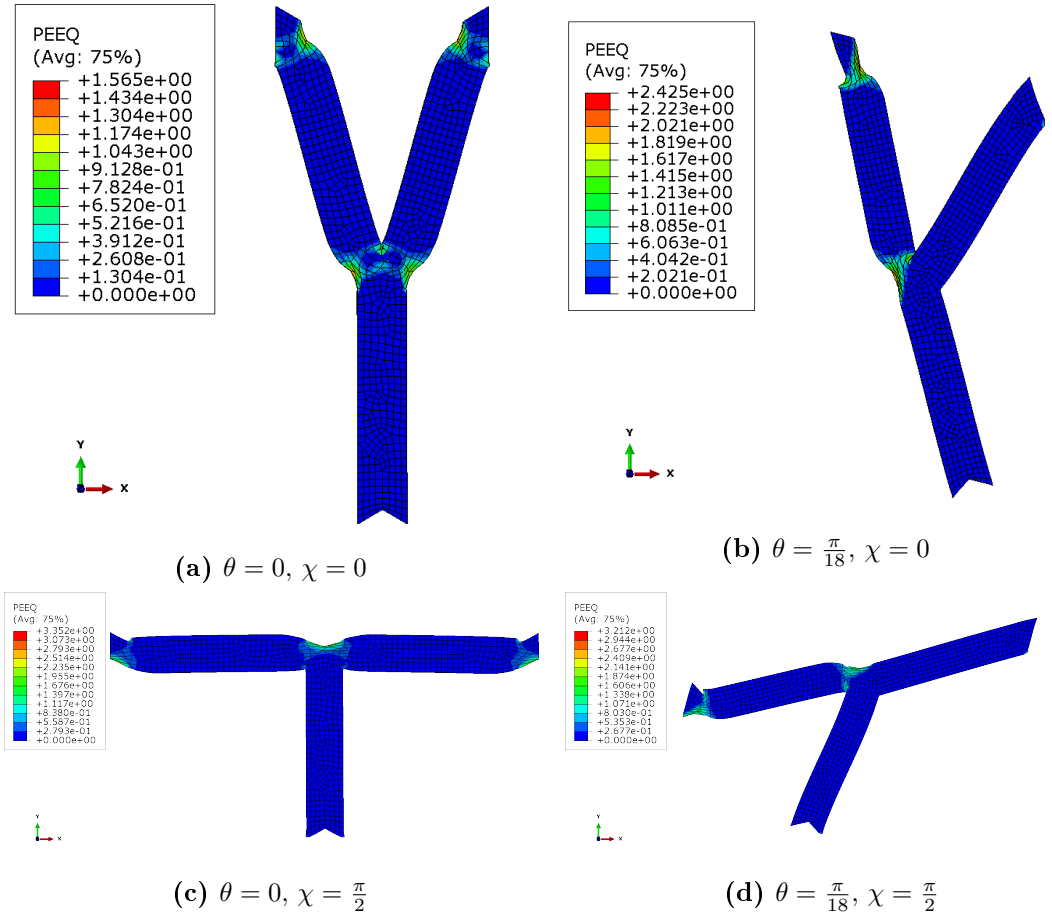

(a) $\theta = 0$, $\chi = 0$ **(b)** $\theta = \frac{\pi}{18}$, $\chi = 0$

(c) $\theta = 0$, $\chi = \frac{\pi}{2}$ **(d)** $\theta = \frac{\pi}{18}$, $\chi = \frac{\pi}{2}$

Figure 5.4: Final configurations of the RVE after different uniaxial simple tests. In the scale of colours the equivalent plastic strain is reported.

on phenomenological observation, which works for a general stress state. Due to the non-linear behaviour that the structure shows from the onset of the tests (see Figure 5.7), the classical criteria for the yield surface do not work here. Indeed, as we can see in Figures 5.4, 5.5 and 5.6, the RVE simulations indicate that yielding occurs only in specific parts of the structure, namely at the joints of the bars. This rather localized offset of yielding is hardly relevant on the macro-scale since it does not affect the yielding behaviour of the macrostructure. From the same set of figures we can also see how the bending of the bars is absent, while the axial elongation has a small contribution. This behaviour is well visible in Figures 5.5, from which we can also appreciate the isotropy of the biaxial test with the eigenvalues having the same magnitude ($\chi = \frac{\pi}{4}$, $\chi = \frac{3\pi}{4}$, $\chi = \frac{5\pi}{4}$): changing the orientation of the imposed load, the result does not change. We remark that these are just some, representative, simulations, from a total of 1440 (20 angles for $\theta \times 72$ angles for χ) for each material. We choose three groups, namely the simple uniaxial tests (Figures 5.4), isotropic biaxial tests (Figures 5.5) and mixed anisotropic biaxial tests (Figures 5.6) for the polyethylene material case (the qualitative behaviour and the final configuration for aluminium would be the same but with a different scale of equivalent plastic strain).

Therefore we need a non-local yield criterion to exclude such irrelevant local plastic deformation. Thereafter, we define that effective yielding occurs when 10% and 40%, for polyethylene and aluminium respectively, of the total stress power is dissipated in plastic deformation, resulting in reasonable values for the yield strength (see Bertram

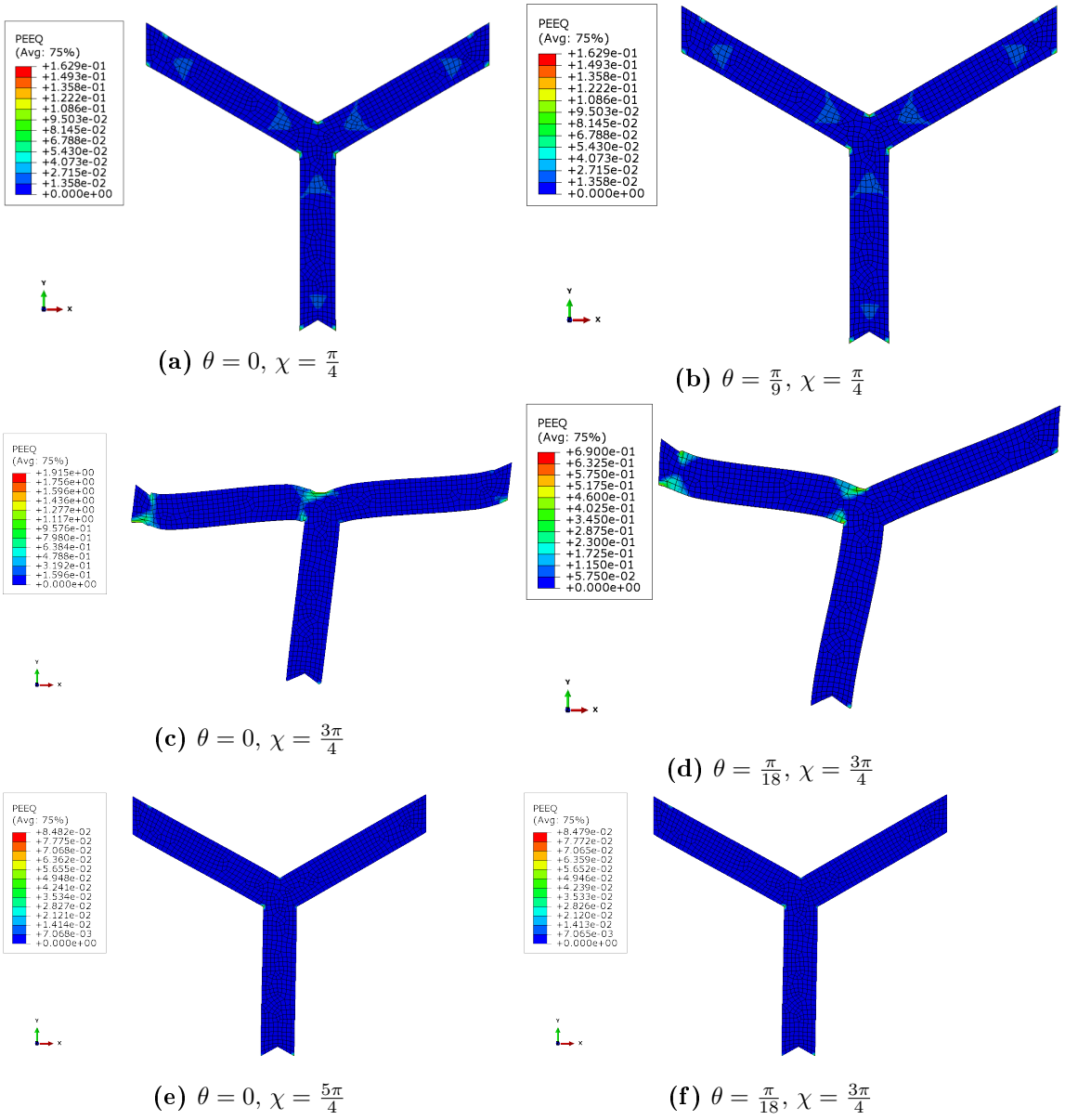

(a) $\theta = 0$, $\chi = \frac{\pi}{4}$ **(b)** $\theta = \frac{\pi}{9}$, $\chi = \frac{\pi}{4}$

(c) $\theta = 0$, $\chi = \frac{3\pi}{4}$ **(d)** $\theta = \frac{\pi}{18}$, $\chi = \frac{3\pi}{4}$

(e) $\theta = 0$, $\chi = \frac{5\pi}{4}$ **(f)** $\theta = \frac{\pi}{18}$, $\chi = \frac{3\pi}{4}$

Figure 5.5: Final configurations of the RVE after different isotropic biaxial tests. In the scale of colours the equivalent plastic strain is reported.

and Kraska [1999]). In order to determine the obtained yield limits for each test, we increase the parameter m until the ultimate loading is reached.

Implementation in ABAQUS with Python algorithm

In Section 5.2.1 we presented the elementary cell which we use for the numerical simulations. In Figure 5.1 we can already see the RVE with the mesh and boundary conditions. We use 20-nodes quadratic hexahedral isoparametric elements with reduced integration (ABAQUS notation: C3D20R), while we prescribe the periodic boundary conditions as

$$\overline{\mathbf{H}} \cdot (\mathbf{x}^+ - \mathbf{x}^-) = \mathbf{u}^+ - \mathbf{u}^-,$$

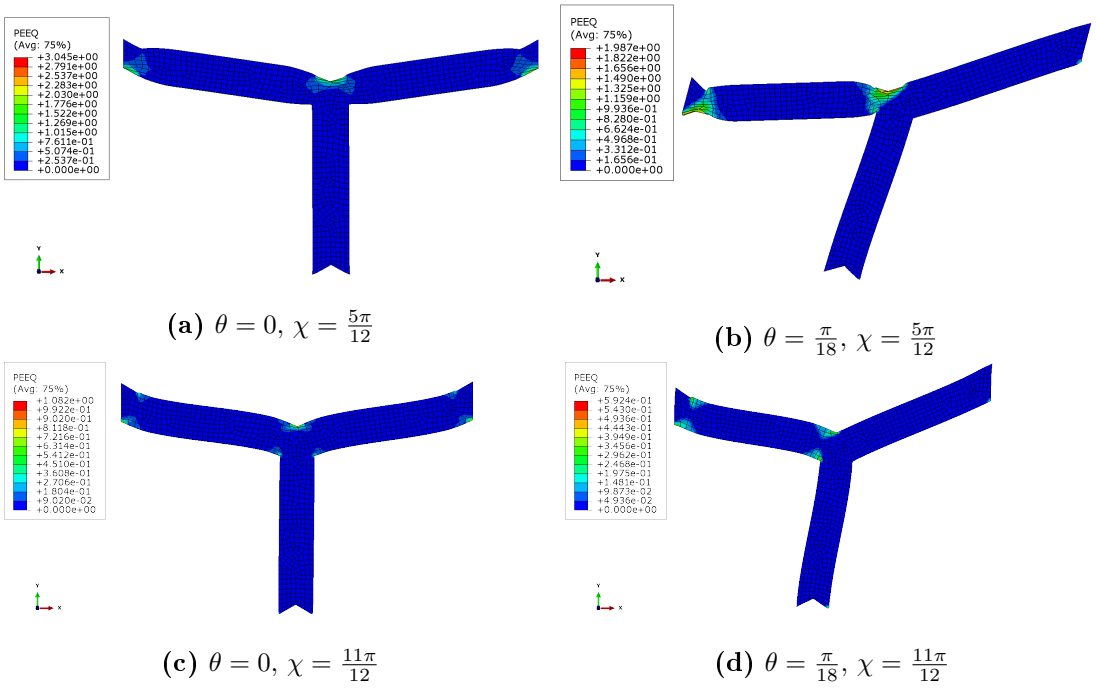

(a) $\theta = 0$, $\chi = \frac{5\pi}{12}$ **(b)** $\theta = \frac{\pi}{18}$, $\chi = \frac{5\pi}{12}$

(c) $\theta = 0$, $\chi = \frac{11\pi}{12}$ **(d)** $\theta = \frac{\pi}{18}$, $\chi = \frac{11\pi}{12}$

Figure 5.6: Final configurations of the RVE after different mixed biaxial tests. In the scale of colours the equivalent plastic strain is reported.

where $\overline{\mathbf{H}}$ is the average displacement gradient, for the coupled elements on the side faces, as highlighted in the Figure (5.1a). Finally, we impose biaxial loads, prescribing an average plane stress state, so to let the structure deform freely.
Notice that the loads are not imposed to any point on the RVE, but on 3 artificial (fictitious) nodes, outside of the Y shape. Each of the nodes has 3 kinematic and 3 dynamic degrees of freedom that correspond to the effective stresses and strains. Now, we want to perform stress driven tests but in a plane strain field, avoiding rigid rotations. We know that $\mathbf{H} = \mathbf{E} + \mathbf{W}$; In particular, when linear theory is considered the displacement gradient is the sum of a strain measure and a rotation. At this point two possibilities arise: either one lets $\mathbf{H}$ be completely free, allowing rotations, or constrains it to be symmetric and lets just the strains be free. We noticed that, if the rotations are allowed, strange instability effects arise, resulting in non monotonic stress-strain curves, and in extreme cases, the flipping of the RVE. In order to avoid this behaviour, but still obtain what we want, we prescribe the following

average stress

$$\overline{\mathbf{T}} = \begin{bmatrix} T_{11} & T_{12} & 0 \\ T_{12} & T_{22} & 0 \\ 0 & 0 & 0 \end{bmatrix}$$

average displacement gradient

$$\overline{\mathbf{H}} = \begin{bmatrix} free & free_{sym} & free_{sym} \\ free_{sym} & free & free_{sym} \\ free_{sym} & free_{sym} & free \end{bmatrix}$$

so to have plane strain solution, without rigid rotations[1].
Setting a looping algorithm in Python, we performed simulations for all angles $0 \leq \chi \leq 2\pi$ with steps of $\pi/36$ and $0 \leq \theta \leq \pi/6$ in steps of $\pi/(6 * 20)$. In Figure 5.7 the stress-strain responses, with the respective yield points, for both materials are shown: each group of curves show different loading conditions, for different angles θ. We can see that the general behaviour is quite similar for the two materials, except for the orders of magnitude of the stresses and strains. In both cases, the weakest response is given from the mixed loading condition, namely $\chi = \frac{3\pi}{4} = \frac{7\pi}{4}$, the strongest from the biaxial tension, $\chi = \frac{\pi}{4}$, while in between we have the biaxial compression, $\chi = \frac{5\pi}{4}$, in which the two direction of loading compensate each other. Moreover, we can notice that, for polyethylene, non-linearities arise already from the very beginning of the elastic part, and that, in general, its response is much weaker that the one of aluminium.

In Figures 5.8 and 5.9, we report the four cases of interest (for both materials), namely $\lambda_1 > 0$, $\lambda_2 > 0$ (tension-tension tests), $\lambda_1 < 0$, $\lambda_2 > 0$ (compression-tension tests), $\lambda_1 < 0$, $\lambda_2 < 0$ (compression-compression tests) and $\lambda_1 > 0$, $\lambda_2 < 0$ (tension-compression tests), where each point is the yield limit extracted from the respective test.
We observe that for the case $\chi = 0$ (simple tension test) the behaviour is very anisotropic, while it reduces to a perfect circle in the case $\chi = \pi/4$ (biaxial isotropic load). Looking at Figures 5.8 and 5.9 we can also estimate the different load magnitudes that the structure may support: we see that for compression-compression tests, the yield stress is 10 to 100 times smaller than in compression-tension and tension-tension tests. An exception is the isotropic compression-compression test ($\chi = 5/4\pi$) which instead shows a high resistance of the structure, comparable to the one in a tension-tension tests. Such behaviour can be explained with the simple observation that, if the stresses are of the same sign, they can balance each others' bending moments. On the other hand, if stresses are of opposite sign, the bending caused by one is increased by the other, therefore inducing a premature collapse (Gibson and Ashby [1997]). Notice that all these considerations may be generalized, if one thinks to uniaxial loads ($\lambda_1 = m$, $\lambda_2 = 0$), equally biaxial loads ($\lambda_1 = \lambda_2$) or inverse biaxial loads ($\lambda_1 = -\lambda_2$).
In all these cases we can recognise the hexagonal symmetry at $\pi/3$. Finally, we can already observe some differences between the behaviour of the two materials. We see that the response of polyethylene is much weaker than the one of aluminium. This also results on a less isotropic behaviour from the plastic material which, as we will see in the next paragraphs, will lead to a non-convex yield surface.

Once more, we want to explain the importance of having an appropriate model for these properties of the material. Indeed if one is able to predict the modes of collapse of such a structure, one is able to prevent or even modify them to obtain optimal behaviour for the purposes they are produced for. To this aim, the behaviour of the polyethylene structure is of major interest, since it is weaker and less classical, triggering the localization with more ease than in the aluminium structure.

5.3 Interpolated yield surface and flow direction

In this section we will see the yield surfaces obtained through the interpolation of all the yield points found as described in the previous sections. In this way we can get an impression of their shape. Since we are considering a 2D plane stress problem, and

[1] The entries denoted by "$free$" take the values resulting from the solution of the problem ("$free_{sym}$" are imposed to be symmetric), all the others entries are given

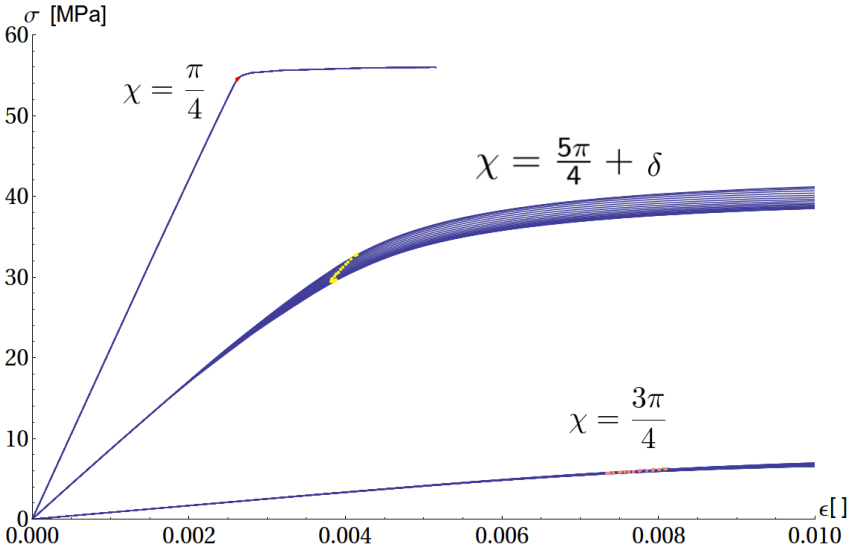

(a) Aluminium

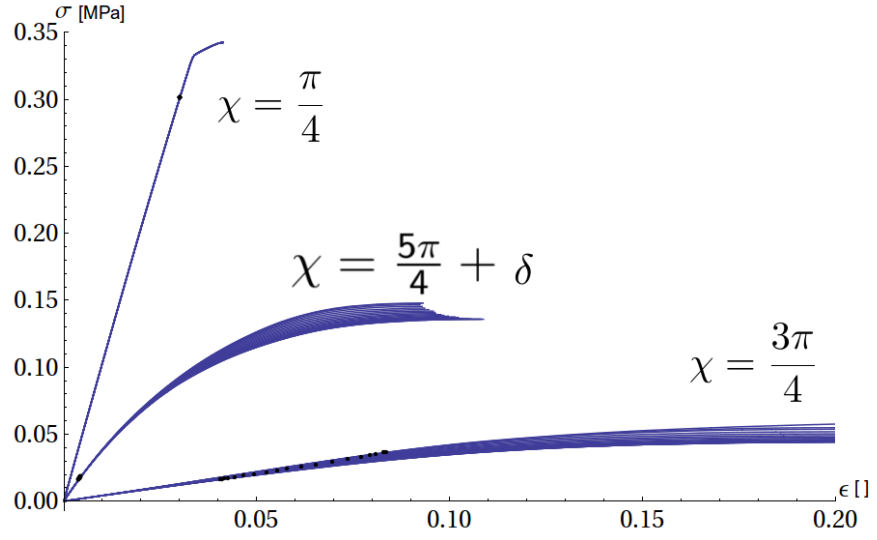

(b) Polyethylene

Figure 5.7: Stress-strain curves for aluminium and polyethylene, with yield points, for different types of tests

small strains, we can represent the yield points, in the three dimensional stress space, with T_{11}, T_{22} and T_{12} as perpendicular axes[2] (see Figure 5.10). Then we will make some considerations on the so found yield surfaces, and, in particular, we focus on the consequences of the non-convexity arising from the case of polyethylene, analysing its plastic flow direction.

Figure 5.10 show the interpolated yield surfaces for aluminium and polyethylene.

The continuous surfaces are obtained interpolating the yield points resulting from the numerical simulations. It is immediately visible the strong non-convexity at the extreme

[2]We can write the Cauchy stresses as

$$\mathbf{T} = T_{11}\mathbf{e}_1 \otimes \mathbf{e}_1 + T_{22}\mathbf{e}_2 \otimes \mathbf{e}_2 + T_{12}(\mathbf{e}_1 \otimes \mathbf{e}_2 + \mathbf{e}_2 \otimes \mathbf{e}_1) = T_{11}\mathbf{r}_1 + T_{22}\mathbf{r}_2 + T_{12}\mathbf{r}_3,$$

where $\mathbf{e}_i$ is a two dimensional orthonormal basis, and $\mathbf{r}_i$ is a three dimensional, orthogonal one.

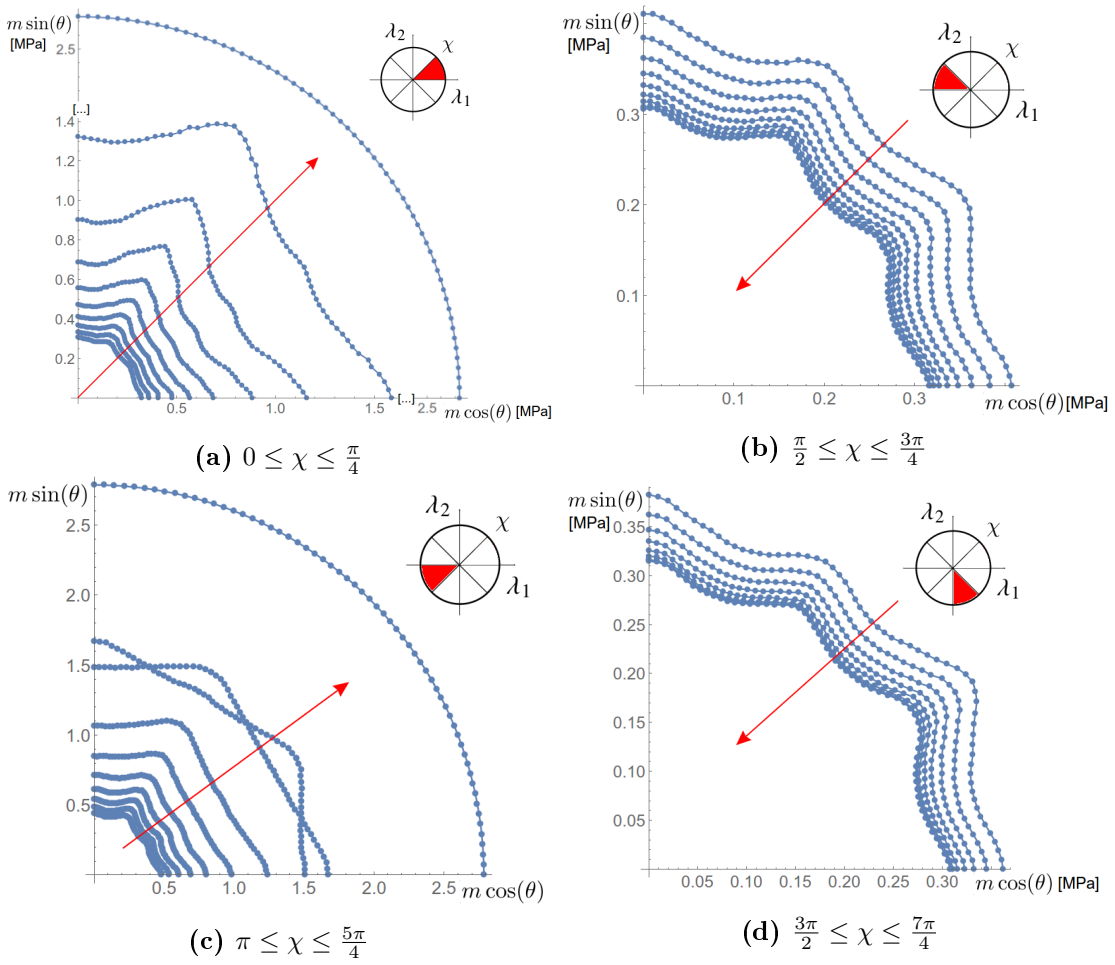

(a) $0 \leq \chi \leq \frac{\pi}{4}$ **(b)** $\frac{\pi}{2} \leq \chi \leq \frac{3\pi}{4}$

(c) $\pi \leq \chi \leq \frac{5\pi}{4}$ **(d)** $\frac{3\pi}{2} \leq \chi \leq \frac{7\pi}{4}$

Figure 5.8: Yield curves for different values of χ, increasing in the direction of the arrow, for aluminium.

ends of the shape, i.e. in the compression and tension areas, for the case of polyethylene, while we find almost symmetry in the response of the aluminium. We see that for both materials the three-fold symmetry from the perspective of the hydrostatic axes is well represented in the surface.

At this point natural questions arise: how does such a yield surface evolves? Is the normality rule applicable? In order to answer the first questions, one could set up simulations on cyclic loadings (as described in chapter 7), and see how, at each cycle, the residual plastic deformations influence the following yield point. For seek of completeness, we performed one cycle of loading in the uniaxial compression, polyethylene, case: as a starting point for the next set of simulations, we took the unloaded configuration after the uniaxial compression test. The most important result which we obtained is that, already at the first cycle, the six-fold symmetry of the yield surface is lost, as we can see in Figure 5.11.

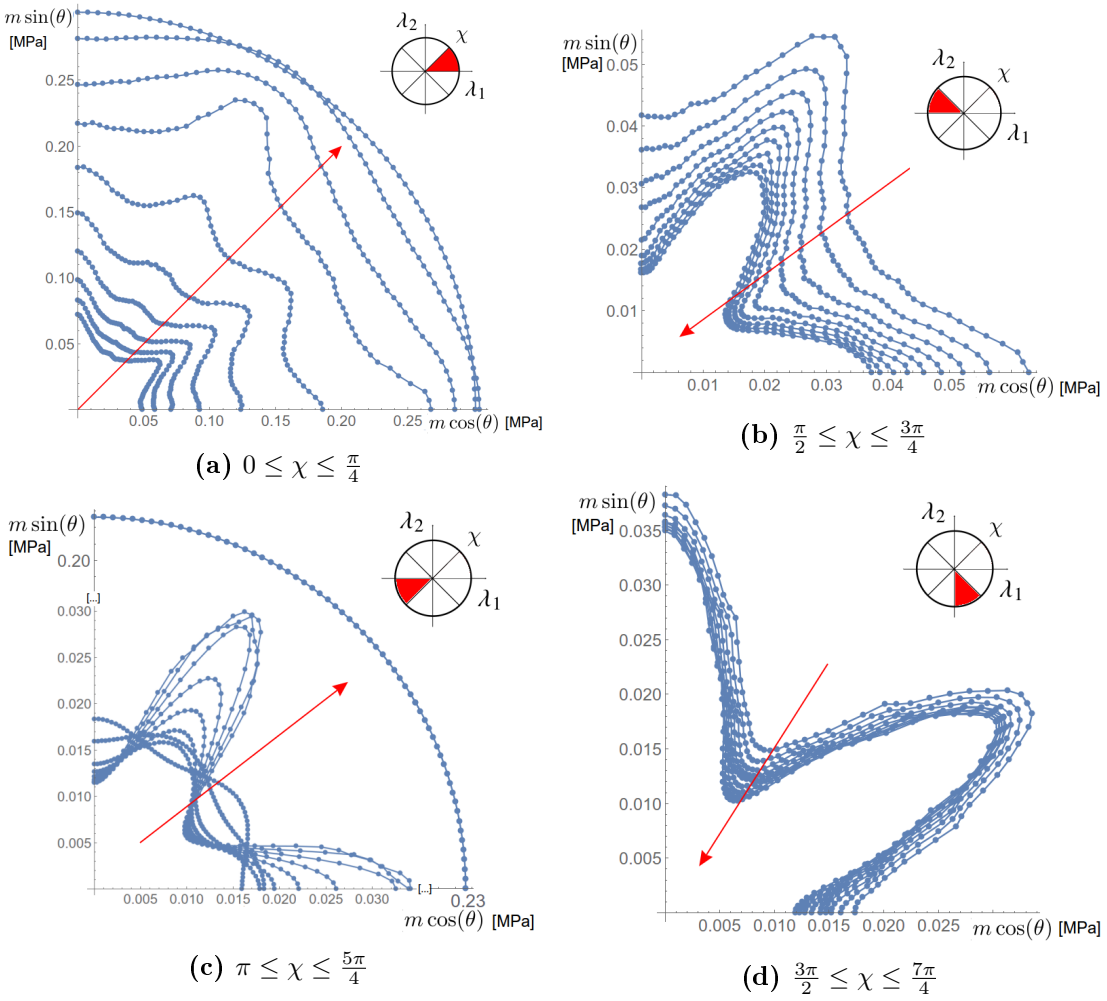

(a) $0 \leq \chi \leq \frac{\pi}{4}$ **(b)** $\frac{\pi}{2} \leq \chi \leq \frac{3\pi}{4}$

(c) $\pi \leq \chi \leq \frac{5\pi}{4}$ **(d)** $\frac{3\pi}{2} \leq \chi \leq \frac{7\pi}{4}$

Figure 5.9: Yield curves for different values of χ, increasing in the direction of the arrow, for polyethylene.

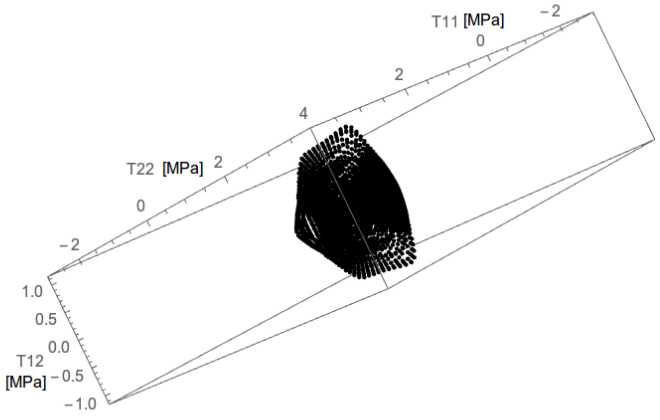

Figure 5.11: View, from the hydrostatic axes, of the yield points, in the stress space, after one cycle of loading

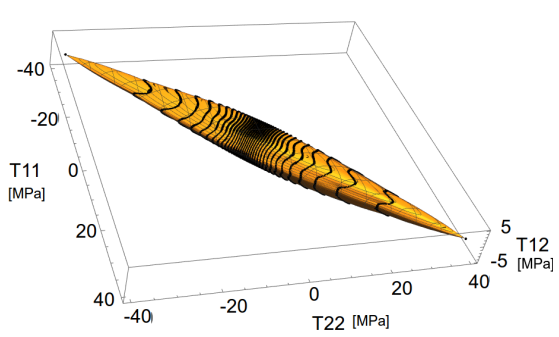

(a) Aluminium: general view

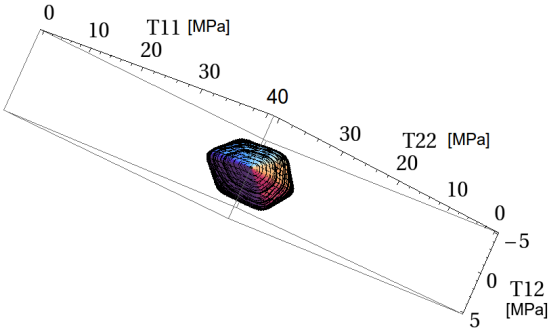

(b) Aluminium: hydrostatic axes view

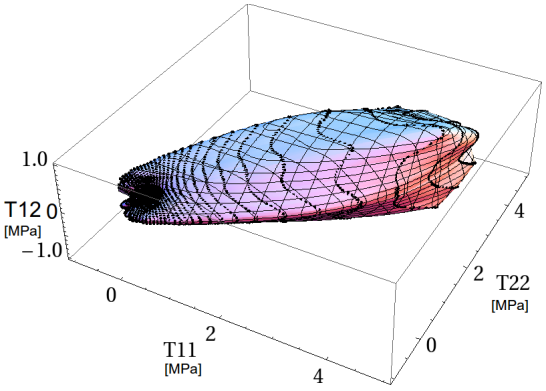

(c) Polyethylene: general view

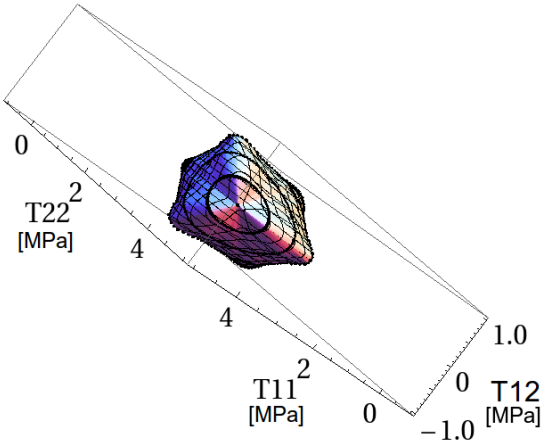

(d) Polyethylene: hydrostatic axes view

Figure 5.10: Numerical result for the yield surfaces, obtained interpolating the yield points of each simulation

Also, we can check if the associative flow rule holds. In this spirit we run a new set of simulations, from which we extract the plastic strain increment between two steps:

$$\Delta \mathbf{E}_p = \mathbf{E}_{p,n+1} - \mathbf{E}_{p,n}. \tag{5.6}$$

If we plot it as a vector in the stress space, using the yield surface as a starting point, we obtain the effective plastic flow direction, which we compare with the one obtained using the normality rule (3.31).

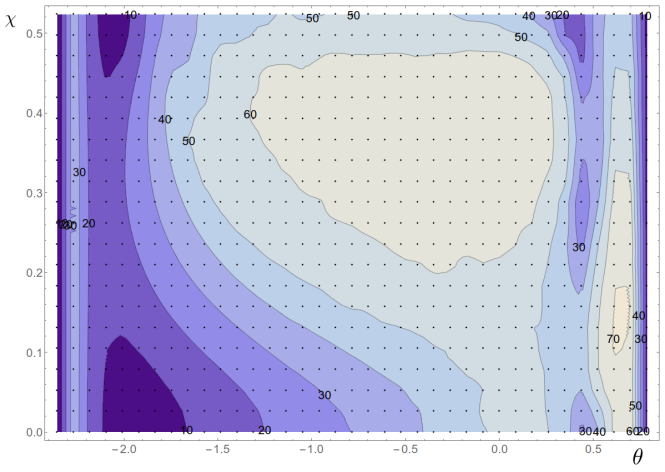

Figure 5.13: Distribution of the angle deviation in function of θ and χ

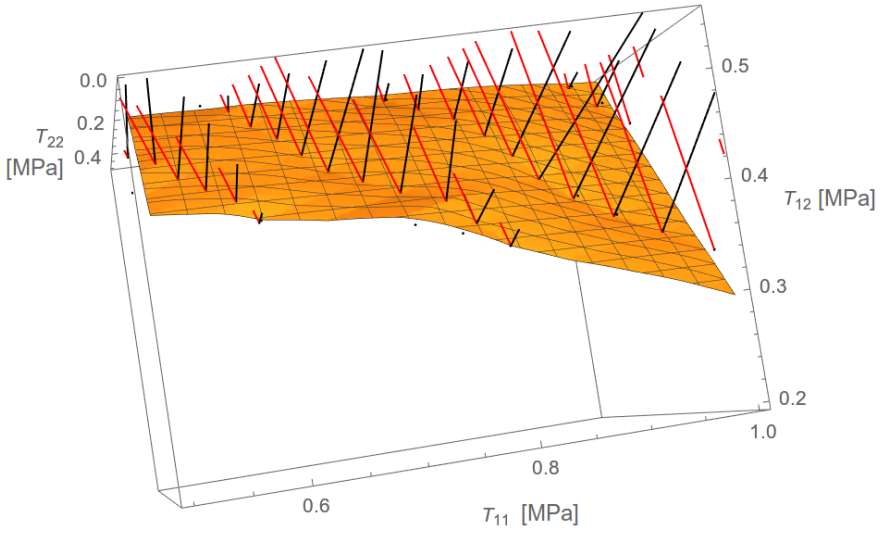

Figure 5.12: Normal versus effective flow direction in the case of a tension test, for polyethylene. In red: the real flow direction. In black: the normality rule flow direction

In Figure 5.12, we can see a slice of the polyethylene's yield surface, on which we plot the directions of the flow, computed with the normality rule (in black) and with the plastic strain increment (in red), in the case of a tension test. It is immediately clear that the two directions are very different, meaning that a non-associative flow rule is needed, to model the plastic behaviour. It is even more clear if we have a look at Figure 5.13: the diagram reports the angle deviation in function of the position on the yield surface in the stress space. The light blue colored parts have de highest value, reaching 70 degrees, in the areas of tension and compression (i.e. where the non-convexity is more evident).

This result indicates the need of a non-associative flow rule (Sumelka and Nowak [2015], Bigoni and Hueckel [1991], Lubarda et al. [1996]) which will be developed in chapter 8, starting from another length scale.

5.4 Mathematical fit of the yield surface

Up to now we performed numerical simulations on a representative element, which were able to give us the response of such structures under different loading conditions, and, from this, we could extract the yield limit. Now we present a mathematical expression for these yield limits, which we may use as a starting point for a plastic model for honeycombs. We see different ways of dealing with the elastic-plastic behaviour of honeycombs in Davini [2013], Asada et al. [2009, 2008], who use homogenization techniques such as Γ-convergence or the fully implicit homogenization scheme proposed in Asada and Ohno [2007], or in Karagiozova and Yu [2004] which describes and analyses different collapsing modes using a limit analysis approach.
For the aim of finding a good elastic-plastic model for any material or structure, first one has to determine the elastic range. This is bounded by the yield limit, which can be defined in the stress or strain space. Inside this elastic range, the behaviour is assumed to be elastic. On the other hand, when the stresses reach the yield limit, and if the loading condition is fulfilled, plastic flow occurs. This may change the current elastic range (see Bertram [2015]).

5.4.1 A non-classical approach to obtain the yield limit based on invariance requirements

To describe the complete yield behaviour of honeycombs, we use a non-classical approach, which is able to give a satisfying prediction of the response for every type of plane load. We want to get the yield criterion in the form

$$\Phi = \| \mathbf{T} \| - m_{crit}(\theta, \chi), \tag{5.7}$$

where the function $m_{crit}(\theta, \chi)$ complies with the invariance requirement with respect to both material symmetries (six fold, $m_{crit}(\theta, \chi) = m_{crit}(\theta + n\frac{\pi}{3}, \chi)$) and eigenvalues ordering ($m_{crit}(\theta, \chi(\lambda_1, \lambda_2)) = m_{crit}(\theta, \chi(\lambda_2, \lambda_1))$). The procedure can be summarized as follows:

- We start with a parametric ansatz for the magnitude of the yield stress:

$$m_{crit} = a(\chi) + b(\chi)\cos(6\,\theta), \tag{5.8}$$

  which is composed by an isotropic part $a(\chi)$ and an anisotropic one $b(\chi)$, multiplied by the term $\cos(6\,\theta)$, which captures the material symmetries shown by the structure. Thus, the invariance of the function with respect to the eigenvalue ordering, will be necessarily contained in the terms depending on χ. Notice that it is possible to add higher order terms, but this would increase the complexity of the function as well as the number of model parameters, while only giving a very small contribution to the precision of the representation of the yield limit. Therefore, we limit the structure of m_{crit} to only one anisotropic part;

- For numerical simulations with a constant χ and a parameter sweep for θ, we determine a best fit for $a(\chi)$ and $b(\chi)$. In this way we get different values of $a(\chi)$ and $b(\chi)$ for different angles χ which are the dots in Figures 5.15 and 5.16;

- Observing the trend of the parameter values, we write two functions for $a(\chi)$ and $b(\chi)$, depending on χ, still parametric, but with the least possible number of terms. Then we fit the parameters, p_i, $i = 1...n$, to the values of a and b from the first parameter fit (see Figures 5.15 and 5.16). Notice that in these functions, the invariance with respect to eigenvalues ordering is already contained. Indeed, the functions show interesting properties: they are both periodic of 2π, $a(\chi)$ is symmetric with respect to the vertical axes at $\pi/4$ (even function) while $b(\chi)$ is symmetric with respect to the point $(\pi/4, 0)$ (odd function). It is easy to show by geometric arguments that by inverting the eigenvalues ordering, the angles θ and χ would change in such a way that $m_{crit}(\theta^1, \chi^1) = m_{crit}(\theta, \chi)$;
- After writing $m_{crit} = a(\chi) + b(\chi)\cos(6\,\theta)$, we could iterate this process in order to get a better match to the numerical values, adjusting the 7 parameters and, eventually adding another exponential term to the isotropic part $a(\chi)$. The obtained functions with the numerical values are shown in Figures 5.15 and 5.16. We can already give an interpretation to $a(\chi)$ and $b(\chi)$ which goes beyond the isotropy meaning. Indeed, while $a(\chi)$ mainly gives the magnitude of the stresses, $b(\chi)$, tells us when the response is isotropic, and, what is more, its sign gives the very important information on the direction of the higher stress. Indeed we can notice, comparing Figures 5.15 or 5.16 with 5.8 or 5.9, that for $b < 0$ the higher stress is in $\theta = \pi/6 + n\pi/3$ direction, while, for $b > 0$ it is in $\theta = n\pi/3$ direction.

With such a construction, we are now able to get m depending only on θ and χ.
At this point, we still need to find a way to compare $m_{crit}(\theta, \chi)$ with $\mathbf{T}$. To this aim, we make use of Mohr's circle construction (Figure 5.14).
We write θ and χ depending on the components of $\mathbf{T}$ and compute $\| \mathbf{T} \|$:

$$\chi = \arctan\left(\frac{T_{11} - \sqrt{4T_{12}^2 + (T_{11} - T_{22})^2} + T_{22}}{T_{11} + \sqrt{4T_{12}^2 + (T_{11} - T_{22})^2} + T_{22}}\right)$$

$$\theta = \arctan\left(\frac{2T_{12}}{T_{11} + \sqrt{4T_{12}^2 + (T_{11} - T_{22})^2} - T_{22}}\right)$$

$$\| \mathbf{T} \| = \sqrt{T_{11}^2 + 2T_{12}^2 + T_{22}^2}.$$

The yield criterion is then given by the difference between the equivalent stress given by $\| \mathbf{T} \|$ and the previously computed yield stress $m_{crit}(\theta, \chi)$:

$$\Phi = \| \mathbf{T} \| - m_{crit}(\theta, \chi) \leq 0, \tag{5.9}$$

where $\Phi \leq 0$ indicates the elastic range.

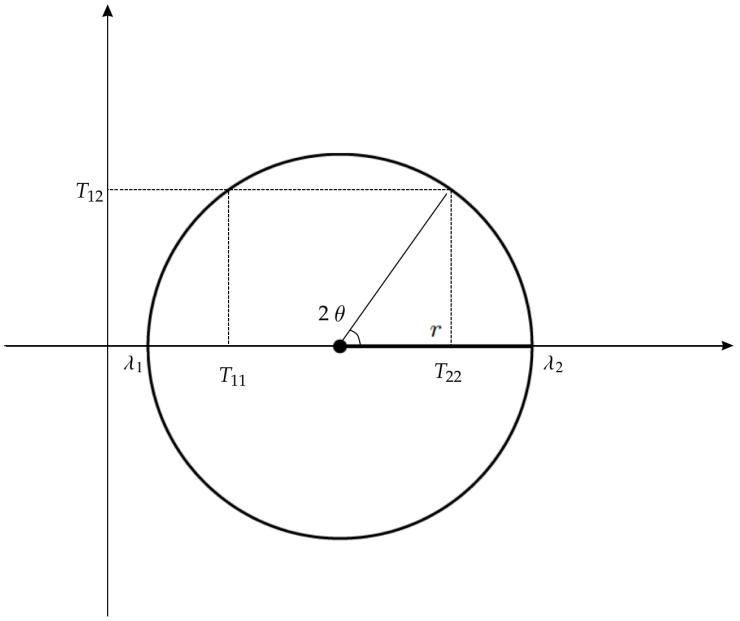

Figure 5.14: Mohr's circle represented by the components of **T**

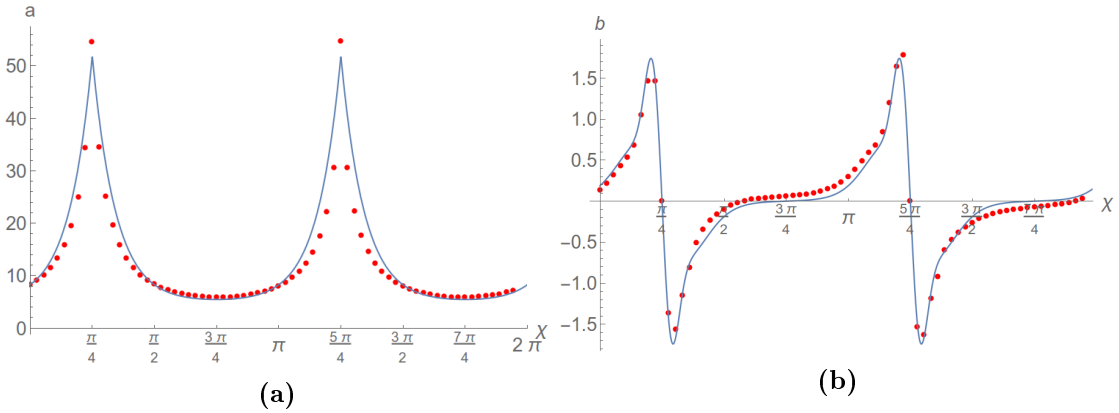

Figure 5.15: Numerical values for a and b (dotted) with the described fitting functions (in blue) $a(\chi) = p_1 + p_2 \cosh(p_3(\frac{\pi}{4} - \chi))$, with periodicity of π, and $b(\chi) = p_4 e^{p_5 \cos(\frac{\pi}{5}+\chi)^2} - p_6 e^{p_7 \cos(\frac{13\pi}{60}+\chi)^2} + p_4 e^{p_5 \sin(\frac{\pi}{5}-x)^2} + p_6 e^{p_7 \sin(\frac{13\pi}{60}+\chi)^2}$, for aluminium.

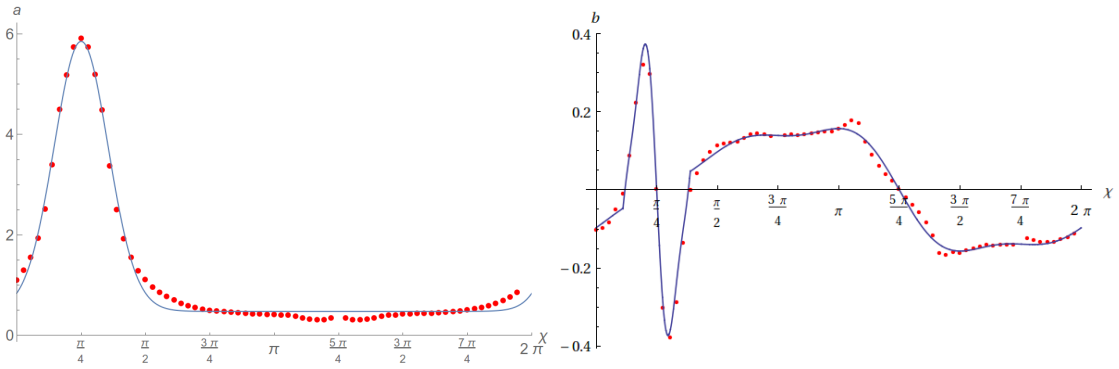

(a) **(b)**

Figure 5.16: Numerical values for a and b (dotted) with the described fitting functions (in blue) $a(\chi) = p_1 + p_2\, \mathrm{e}^{p_3(\cos(\frac{\pi}{4}-\chi))}$ and

$$b(\chi) = \begin{cases} p_4 \sin(p_5(\chi - \frac{\pi}{4})), & \text{if } \frac{\pi}{9} \leq \chi \leq \frac{7\pi}{18} \\ p_6 \sin(\chi - \frac{\pi}{4}) + p_7 \sin(3(\chi - \frac{\pi}{4})), & \text{if } \frac{7\pi}{18} < \chi \leq \frac{19\pi}{9} \end{cases}, \text{ for polyethylene.}$$

5.4.2 3D yield surface

With this approach, we are finally able to plot the three dimensional yield surface in the space of the stress tensor components.

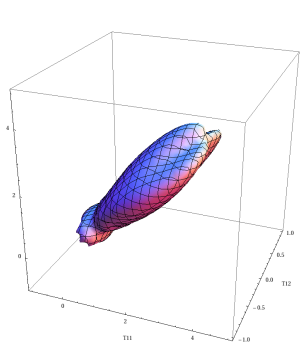

(a) 3D general view.

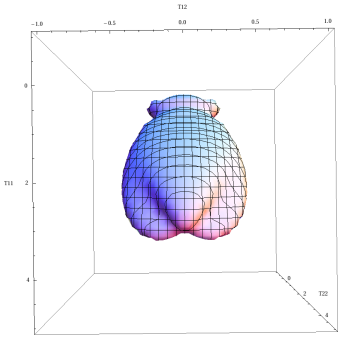

(b) Front view from the T_{22}, T_{12} plane.

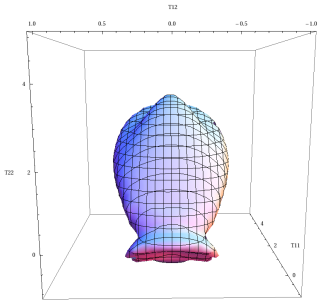

(c) Back view from the T_{22}, T_{12} plane.

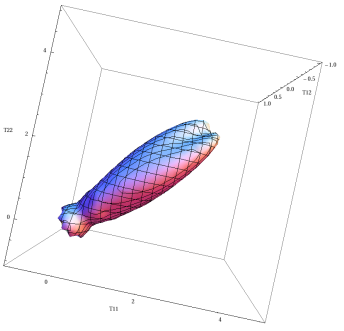

(d) Side view from the T_{11}, T_{22} plane.

Figure 5.17: 3D initial yield surface for polyethylene.

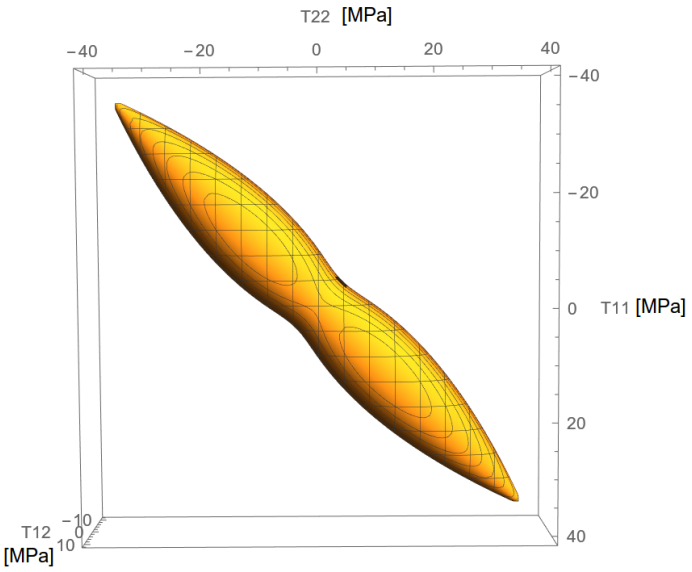

Figure 5.18: 3D initial yield surface for aluminium. Units: [MPa]

It is interesting to notice that the resulting surfaces appear for both materials to be non-convex. This observation is confirmed if one uses the relation

$$\Phi(v\mathbf{T}_1 + (1-v)\mathbf{T}_2) \leq 0, \quad \text{if } \Phi(\mathbf{T}_1) \leq 0 \ \wedge \ \Phi(\mathbf{T}_2) \leq 0 \quad \forall v \in [0,1]\,.$$

Indeed, this inequality does not hold for all points of the fitted surfaces, thus proving the non-convexity of the result.
Notice that in the case of aluminium (Figure 5.18) we did not consider the contribution of the function $b(\chi)$ since it is much smaller than the one of $a(\chi)$ (it is immediately visible comparing the order of magnitude on Figure 5.15a and 5.15b). Instead, in the case of polyethylene, $b(\chi)$ assumes more importance, since it is 0 in a few points and of a comparable magnitude to $a(\chi)$ in almost the whole interval. This results in the six fold symmetry, and the strong non-convexity at the ends of the surface, as visible in Figure 5.17.
It is important to not forget that this is a mathematical approximation of the yield surface of the two materials. Indeed, as we saw in the yield surfaces found through interpolation, while for aluminium the non-convexity results to be an artefact of the approximation, for the polyethylene the non-convexity is an actual property of the effective cellular solid.

Conclusions

We set up a numerical laboratory, with a convenient RVE and a simple parametrization of the stress tensor. With this tools we performed FE simulations which allowed us to find the effective yield surface for the honeycomb structure for both materials. The most important information arising from this is its non-convexity and all that we can deduce from its shape, i.e. the elongation along the hydrostatic axis and bigger magnitude in tension than in compression, in the case of polyethylene (strength differential effect),

as well as its plastic compressibility. We could also make some important observations: the plastic deformations localize at the joints; the bending of the bars is hardly present; there is no plastic deformation coming from the elongation of the bars. Notice that all these features, will be used later on to make assumptions for the analytical model.
Although we can already learn a lot from the results obtained, the parametrization has a big weakness: as soon as the symmetry of the structure breaks, e.g. when first plastic yielding occurs, it can not be used any more. In other words, the nice symmetry properties are lost during the plastic deformation process, and a more general approach is needed.

Chapter 6

Macro-scale I: ABAQUS implementation of the non-convex yield surface with a study of flow rules

6.1 Introduction

In the previous chapter we found an expression for the yield criterion that is able to describe qualitatively the initial yield behaviour of a honeycomb structure. It is important to remark that, as soon as yield occurs, the symmetry given from the regular geometry of the cellular solid is broken (see chapter 5 Figure 5.11). Therefore, all the arguments used to parametrize the stress tensor and to build the mathematical formulation of the yield criterion are lost. A method that can be used to determine the way the yield surface evolves could be to cyclically load and unload the structure: for each loading test one should reach the elastic limit, then release the body, and after this, repeat the whole procedure explained in chapter 5. After a single specific iteration, one would just have the consecutive elastic range, after the yielding due to a very particular loading condition. This means that, to have an exhaustive description of the plastic behaviour of the structure, one should perform a huge amount of numerical simulations just to extract an even bigger number of data, ending up with a very small quantity of understanding. This approach, although very accurate and complete, is not convenient for many reasons. Instead, in this first attempt, we use the expression for the yield surface found in the previous chapter, for the case of polyethylene, which appears to be more anisotropic, non-symmetric and non-convex. This is valid to describe the initial yield behaviour of the homogenized continuum, therefore we try to apply different flow rules, together with hardening, to see which one is able to better capture the localization of the strain.

6.2 Implementation in ABAQUS

ABAQUS/Standard (and also Explicit) has an interface called UMAT (or VUMAT) which allows the user to implement general constitutive equations. When none of the

existing material models included in ABAQUS material library can accurately represent the behaviour of the material to be studied, then a UMAT can be used to create one's own material. Through this interface, material models of any complexity can be defined and tested with advanced structural elements, complex loading conditions, contact and friction and so on. It is also extremely convenient if one wants to model materials which present instabilities or localization phenomena.
Now, let us consider a homogeneous 2D square, with eight-node plane stress mesh elements (ABAQUS denomination: CPS8). We set the boundary value problem fixing the bottom elements and imposing a displacement on top. From the classical von Mises yield criterion, we modify the UMAT, adding personalized subroutines, increasing gradually the complexity of the model implemented. Therefore, we start implementing the yield surface found with the equation (5.9) and we equip it with the associative flow rule (eq. 3.31) or a flow rule accounting for a stress decomposition into isocoric and volumetric part (eq. 6.4); finally we add isotropic hardening as

$$\Phi = \| \mathbf{T} \| - \lambda \, m_{crit}(\theta, \chi), \tag{6.1}$$

where λ is a multiplying factor, scaling isotropically the yield surface, or with a hardening rule acting locally on the yield surface (eqs. 6.2 and 6.3). Notice that this last approach is empirical, based on the observation of the effective behaviour of the structure, i.e. an initial softening behaviour, when the rows collapse one after the other, and hardening when compactification happens (refer to chapter 1 for the general explanation).
For the complete UMAT file, please look at the Appendix B.

Von Mises yield surface with associative flow rule

As a reference solution, we consider the classical von Mises yield limit (eq. 3.26), together with the associative flow rule (eq. 3.31), shown in Figure 6.1:

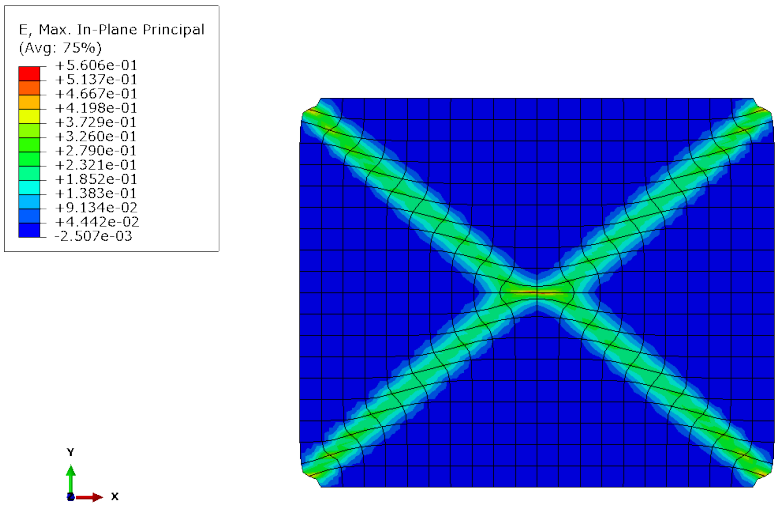

Figure 6.1: Final configuration of a squared sheet of polyethylene after a compression test. In the scale of colours the largest eigenvalue of the absolute strain.

Honeycomb plastic model with associative flow rule

In this section we report the results of the implementation of the yield surface found in chapter 5. We consider a homogeneous material which yields following the presented criterion. We further assume the validity of the associative flow rule and enrich the model with isotropic hardening, equation (6.1), and distortional hardening, equations (6.2) and (6.3).
Figure 6.2 reports the final configuration of a structure, with the yield criterion (5.9) equipped with the associative flow rule.

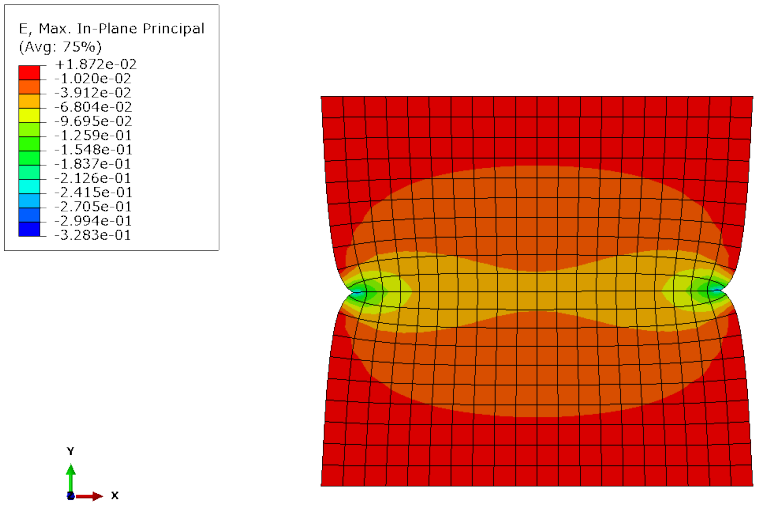

Figure 6.2: Final configuration of a homogenized honeycomb structure, where associative flow rule is applied.

We already see the unstable behaviour of the material, which presents a recess in the middle.
If we add isotropic hardening (see the Appendix B) the result changes slightly:

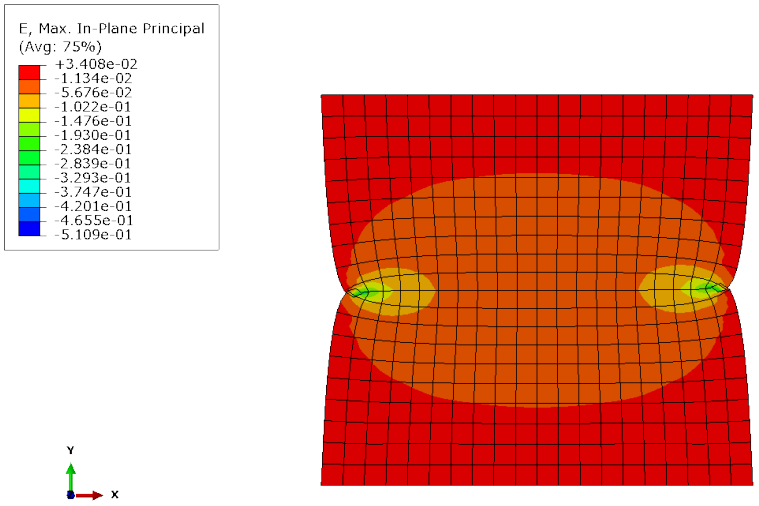

Figure 6.3: Final configuration of a homogenized honeycomb structure, where associative flow rule is applied and isotropic hardening is considered.

We see that the strains are distributed less homogeneously. The recession on the sides is less evident than in the previous case and the general response is stiffer. In both cases, the final configuration results are qualitatively wrong: indeed, while expanding laterally, as we can see from both experimental and numerical results presented in the previous chapters, the body shows lateral contraction, up to superimposition of the mesh, when further displacement is imposed.
Finally we implement a distortional hardening that acts locally on the yield surface. As we explained before, with this method, we would like to capture the softening-hardening behaviour that honeycomb structures show when plastic deformations occur, especially during plastic compression. To this purpose we add a term $c(\mathbf{T}, \boldsymbol{\varepsilon})$ to the magnitude of the yield stresses so that:

$$\Phi = \| \mathbf{T} \| - (m_{crit}(\theta, \chi) + c(\mathbf{T}, \boldsymbol{\varepsilon}))$$

The function $c(\mathbf{T}, \boldsymbol{\varepsilon})$ has the following form:

$$c(\mathbf{T}, \boldsymbol{\varepsilon}) = f(\frac{\mathrm{tr}(\mathbf{T} \cdot \boldsymbol{\varepsilon})}{\| \mathbf{T} \|}) g(\chi(\mathbf{T})), \tag{6.2}$$

with

$$\begin{aligned} f(x) &= \begin{cases} (x - 0.4)^4 - 0.4^4, & \text{if } x \geq 0 \\ 0, & \text{if } x < 0 \end{cases} \\ g(\chi) &= e^{(\frac{-(\chi-\pi)^2}{2\pi/36})} + e^{(\frac{-(\chi-3/2\pi)^2}{2\pi/36})}, \end{aligned} \tag{6.3}$$

where we wrote $f(x)$ instead of $f(\frac{\mathrm{tr}(\mathbf{T}\cdot\boldsymbol{\varepsilon})}{\|\mathbf{T}\|})$ for simplicity.
The function $f(x)$ (Figure 6.4) is built so that it triggers localization through softening, until the 80% of the total deformation is reached, and compactification through hardening, afterwards. $f(x) < 0$ for strains $x < 0.8$ therefore the material will present a softening behaviour, while in the opposite cases we will have hardening.

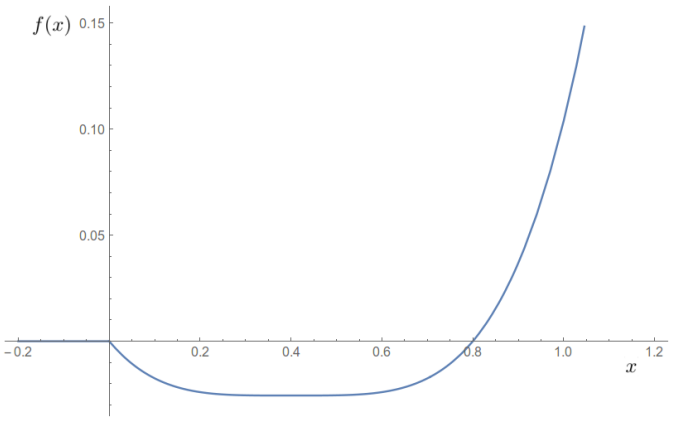

Figure 6.4: Tuning equation $f(x)$.

Its argument $\frac{\mathrm{tr}(\mathbf{T}\cdot\boldsymbol{\varepsilon})}{\|\mathbf{T}\|}$ is the plastic strain component which is in the same direction of $\mathbf{T}$, so that, the described behaviour only happens when you keep loading always in the same direction. On the other hand, this softening-hardening phenomenon, is mostly visible when the structure is subject to compression. That is where the function $g(\chi)$ enters.

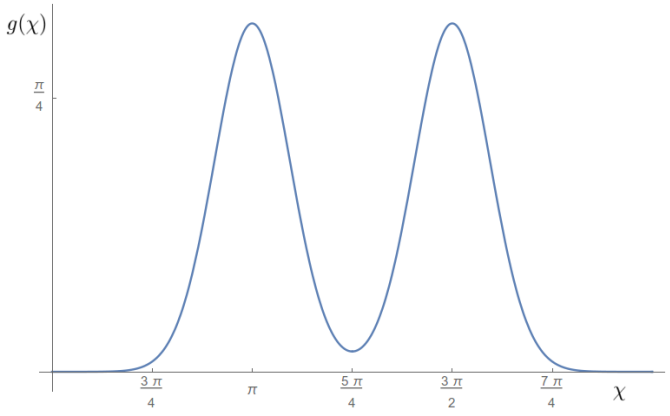

Figure 6.5: Bell equation $g(\chi)$.

$g(\chi)$ is a bell function which tells when the behaviour captured by $f(x)$ is more effective. For example, in the cases of pure compression when $\chi = \pi, 3/2\pi$, we have a big contribution of hardening, and $f(x)$ has a big effect on the yield surface. The overall action is well visible in the following figure:

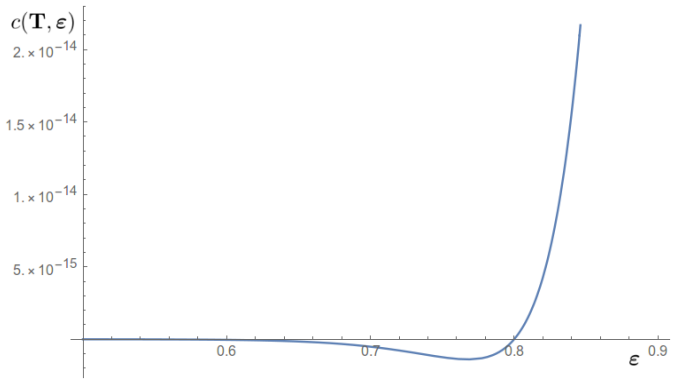

Figure 6.6: Combination of tuning and bell equations: $c(\mathbf{T},\varepsilon)$

where the function $c(\mathbf{T},\varepsilon)$, in the case of compression, is reported. The material behaviour will be softened for strains $0.6 <\| \boldsymbol{\varepsilon} \|< 0.8$, when the rows crash adjacently to each other, and hardened after it, when all the rows have collapsed and compacted. After implementing such a distortional hardening in ABAQUS, we find, for the same boundary value problem as in the previous cases, the following final configuration:

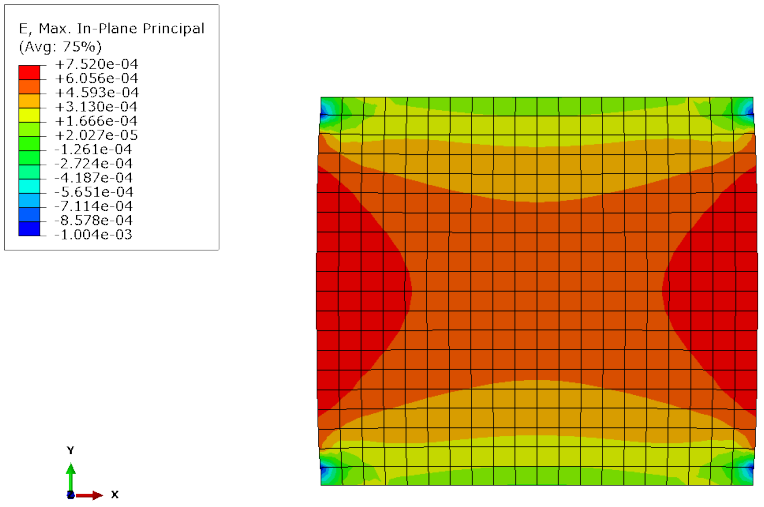

Figure 6.7: Final configuration of a homogenized honeycomb structure, where associative flow rule is applied and distortional hardening is considered.

On one hand we do not have any more instability problems and singularities in the solution, but, on the other, we see that the localizing behaviour is practically disappeared.

Honeycomb plastic model with stress tensor decomposition flow rule

The last set of simulations that we run, are based on a different flow rule, which we again equip with isotropic or distortional hardening. For this case, we decompose the stress tensor into its deviatoric and dilatoric part. This will allow us to control how much of

the strain is dispersed in the isotropic volumetric change of the body (pressure sensitive material), and how much is used for the shape change. The flow rule will be:

$$\dot{\boldsymbol{\varepsilon}}_p = \lambda(s_1\mathbf{T}' + s_2\mathbf{T}^\circ), \tag{6.4}$$

where $\mathbf{T}^\circ = \frac{1}{2}\text{tr}(\mathbf{T})\mathbf{I}$ is the volumetric part (dilatoric) and $\mathbf{T}' = \mathbf{T} - \mathbf{T}^\circ$ is the deviatoric part (see eq. (3.14)). The parameters s_1 and s_2 serve to tune the two contributions and are such that $s_1/s_2 = 10e^{\|\boldsymbol{\varepsilon}\|} + 1$. This function, which looks like the one in Figure 6.8, makes the deviatoric contribution considerable at the beginning of the deformation, while it becomes asymptotically equal to the dilatoric one, at large strains.

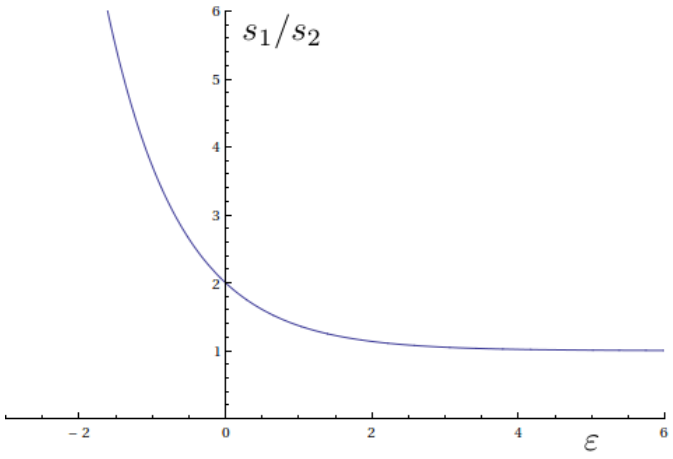

Figure 6.8: Equation tuning the dilatoric and deviatoric contributions of $\mathbf{T}$: $s_1/s_2 = 10e^{\|\boldsymbol{\varepsilon}\|} + 1$

In the Appendix B all this modifications to the UMAT file of ABAQUS can be found and are further explained step by step.
As first case, we implement our yield criterion together with the presented non-associative flow rule:

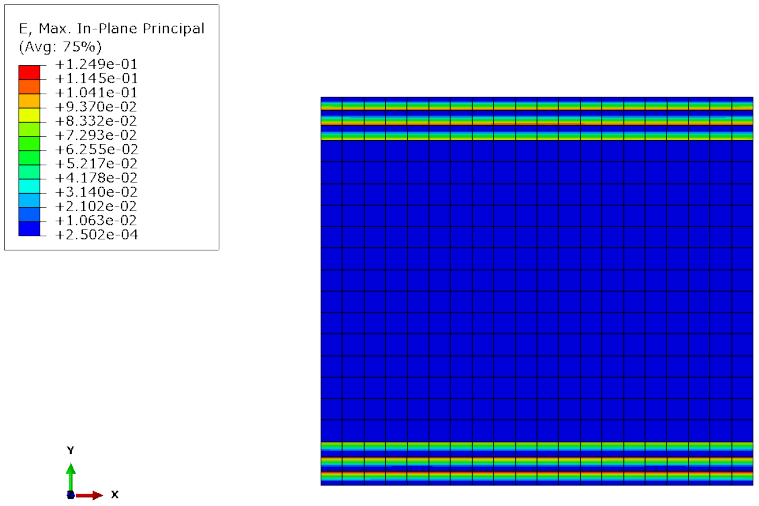

Figure 6.9: Final configuration of a homogenized honeycomb structure, where non-associative flow rule is applied.

Then we add isotropic hardening:

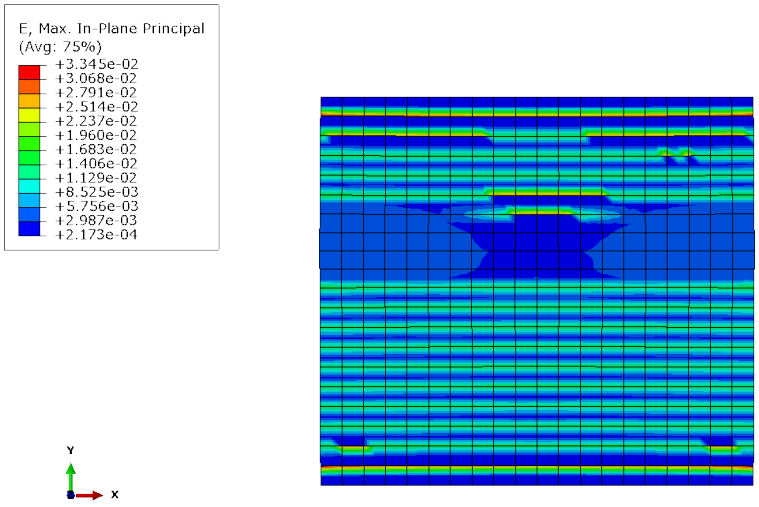

Figure 6.10: Final configuration of a homogenized honeycomb structure, where non-associative flow rule is applied together with isotropic hardening.

And finally the more complicated model with additional distortional hardening:

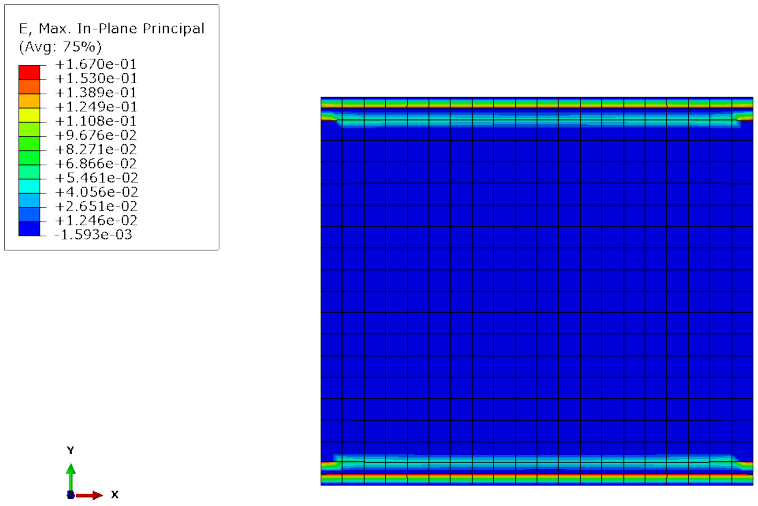

Figure 6.11: Final configuration of a homogenized honeycomb structure, where non-associative flow rule is applied and distortional hardening is considered.

From this set of results we can appreciate a more homogeneous distribution of the strains. We see that the lateral sides of the polygon remain parallel, contrarily to what happened in the previous cases (Figures from 6.2 to 6.7). We notice a small concentration of strains in the upper and lower parts of the body. The last (Figure 6.11), more complicated model, finally, does not bring any new informations about the strain distribution, which is, once more, localized close to the upper and lower boundaries.

Conclusions

We implemented the mathematical fit of the yield surface of the previous chapter in a UMAT subroutine. We tested the behaviour of the body with associative and non-associative flow rules and isotropic and distortional hardening. We conclude that knowing $\Phi(\overline{\mathbf{T}})$ is not enough to catch the plastic behaviour of the structure, since associative plasticity does not work. Although we can see that softening triggers the localization, all the study is kept on a very empirical level. To determine the flow rule and the evolution of the yield surface, either one performs a huge number of numerical simulations and experiments, or some more efficient approach has to be considered. We will see in chapter 8 that the second option leads to better results, is easier to manage and to understand.

Chapter 7

Study of the effect of non-convex yield limit

7.1 Introduction

In section 3.4.2, we presented Drucker's postulate with its features and consequences. However, we did not specify for which class of materials this rule holds. Although Drucker's postulate is used to reduce the functional freedom of the plastic behaviour of many materials, there are some materials which violate Drucker's postulate. In particular, those which exhibit non-convex yield limits. It is often the case for microstructured materials, which present internal buckling and instabilities. In this chapter, we want to analyze and discuss whether the convexity of $\Phi(\mathbf{T})$ actually reflects any effective material property. We start from an isotropic, Mises-like, yield limit, which we perturb in order for it to become non-convex. Two parameters will control the amplitude and number of wiggles that we create. After setting up the model, we will present some study cases, in order to see how the non-convexity of the yield limit influences the qualitative material behaviour.

7.2 The model and its extension

7.2.1 Base model

As base model, we use again the two dimensional one presented in chapter 5. We write the Mieses-like yield limit as:

$$\phi(\mathbf{T}) = \sqrt{2} \parallel \mathbf{T}' \parallel - \sigma_k^{tension} \leq 0 \tag{7.1}$$

where $\mathbf{T}'$ is the stress deviator (for more detail please read Glüge and Bucci [2017]). The yield limit defined above, has the shape of a cylinder with elliptical base, in the stress space (as we already did in chapter 5)(see Figure 7.1).

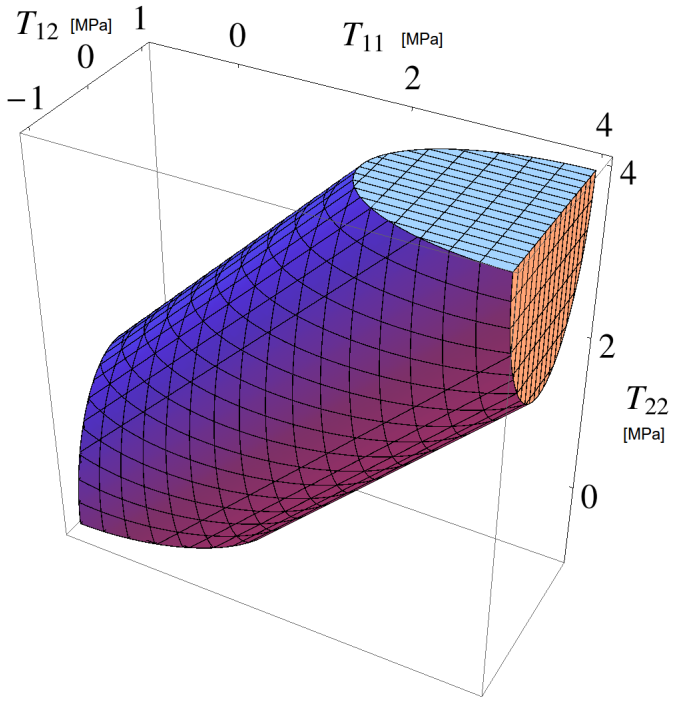

Figure 7.1: Mises cylindrical yield surface in the stress space

7.2.2 Extension of the model

Now, we will consider the base model described in the previous section, and equip it with wiggles. To do so, we start describing the base ellipse in polar coordinates. We consider the stress tensor in the base $\mathbf{r}_i$ and rotate it so that the hydrostatic axis of the cylinder, becomes $\alpha\mathbf{r}_1$:

$$\mathbf{v} = \mathbf{Q} \cdot \mathbf{T}$$
$$\begin{bmatrix} v_1 \\ v_2 \\ v_3 \end{bmatrix} = \begin{bmatrix} \cos(-\pi/4) & -\sin(-\pi/4) & 0 \\ \sin(-\pi/4) & \cos(-\pi/4) & 0 \\ 0 & 0 & 1 \end{bmatrix} \begin{bmatrix} T_{11} \\ T_{22} \\ T_{12} \end{bmatrix}. \tag{7.2}$$

The yield limit becomes

$$\phi(\mathbf{T}) = \sqrt{v_2^2 + 2v_3^2} - \sigma_k. \tag{7.3}$$

If we make σ_k a function of the angle in the $\mathbf{r}_1$-plane, i.e. $\sigma_k = \sigma_k(1+a\cos(n\arctan(v_2/v_3)))$, we are able to introduce n wiggles of amplitude a, on the yield limit. In order to get the polar form of the yield function, we set $\phi(\mathbf{T}) = 0$ and substitute $v_2 = r\sin(\gamma)$ and $v_3 = r\cos(\gamma)$. Then:

$$r(\gamma) = \sigma_k \frac{1 + a\cos(n\gamma)}{\sqrt{2\cos(\gamma)^2 + \sin(\gamma)^2}}, \tag{7.4}$$

where we can use the parameters a and n to control the convexity of the function[1]. In the following, we will consider $n = 3$, which gives $-1/19 \leq a \leq 19$ for the yield limit to be convex in the stress space.

[1] In order to be convex, a polar function with $r > 0 \forall \gamma$, has to satisfy the following condition: $r(\gamma)^2 + 2r'(\gamma)^2 - r(\gamma)r''(\gamma) \geq 0$

7.3 Simulations and results

Simulations setting

In order to run simulations with the proposed model, we implement it as a subroutine in ABAQUS UMAT. Notice that, as the yield limit is non-convex, not all small step sizes are admissible, as the corrector step may become non-unique. Therefore we consider as an upper bound for the step size the smallest curvature radius encountered on the surface (see Figure 7.2).

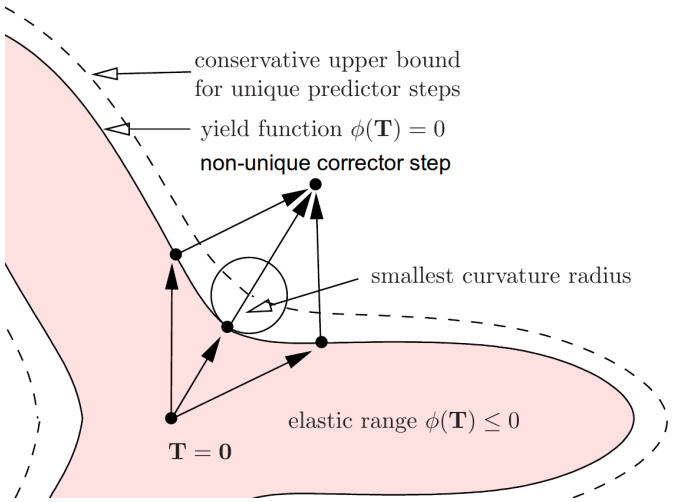

Figure 7.2: Representative three-fold symmetry yield limit, with the relative smallest admissible curvature radius in order to have uniqueness of the solution.

We use a simple simulation to compare with the others in which we impose the wiggles. We consider an homogeneous square of side length l on which we impose a simple shear deformation displacing the upper side by $l/10$, while the remaining two are free, and the lower side is fixed. Additionally to the simulation results, we will plot the yield limit projected parallel to the hydrostatic axis, in a $(T_{22} - T_{11}/\sqrt{2}) - T_{12}$ plane (Figure 7.3c). In the same graph we plot a density histogram with all the stresses met at the end of the finite element simulation, and a line, which shows the accumulated plastic deformations.

Results

In the following pictures we see the reference simulation (7.3) and two set of results obtained increasing (7.4) and decreasing (7.5) the yield stress in the T_{12} direction, respectively. As we can see already from Figure (7.3a) shear bands appear, starting from the corners, where the stress accumulates, while the rest of the deformation remains quite homogeneous. As we learn from the coloured histogram 7.3c, the plastic deformations are predominant in the direction corresponding to a shear combined to a hydrostatic pressure. It is also clear that the direction in which plastic deformations evolve, is normal to the yield limit.

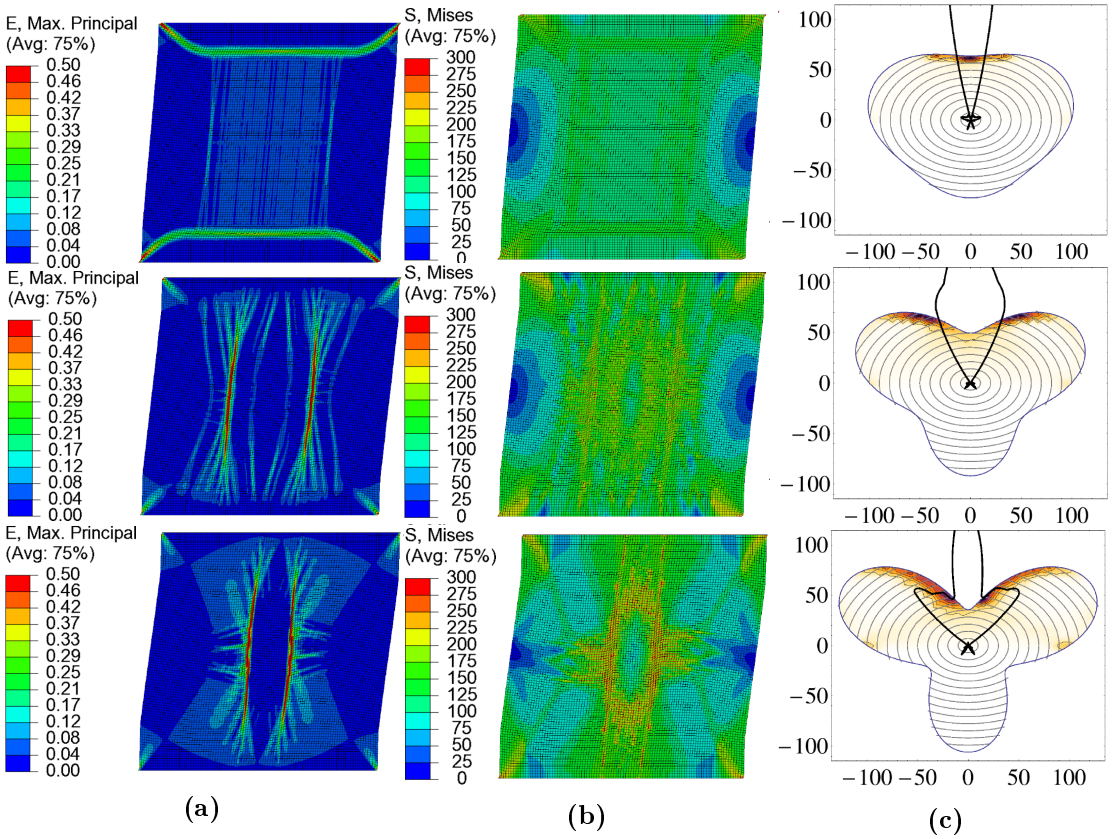

Figure 7.4: Shear test simulation run increasing the wiggle amplitude: $a = 0.1, 0.3, 0.5$. From left to right: (A) largest eigenvalue of the absolute strain, (B) equivalent von Mises stress, (C) yield limit, density histograms of the stresses and accumulated plastic deformations.

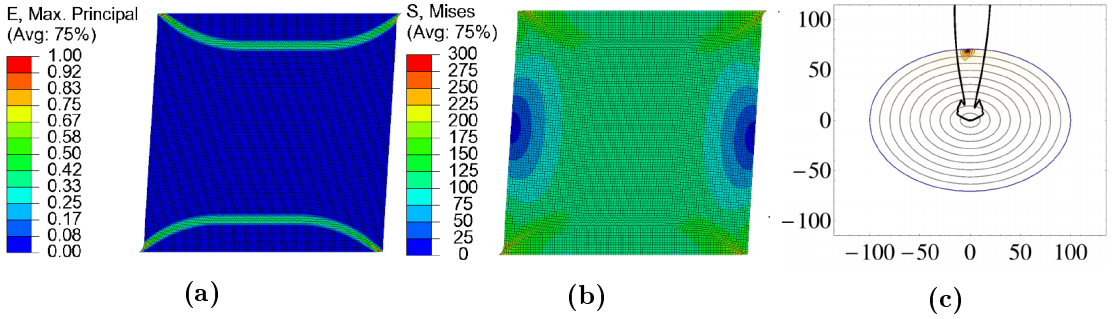

Figure 7.3: Reference shear test simulation run with the Mises yield criterion. From left to right: (A) largest eigenvalue of the absolute strain, (B) equivalent von Mises stress, (C) yield limit, density histograms of the stresses and accumulated plastic deformations.

On the other hand, when we increase the yield stress in T_{12} direction, Figure 7.4, two stress concentrations appear, increasing in the same direction where the bulges develop. Also the plastic deformation accumulates in the same region, in agreement to the fact that the normals to the surface coincide with the largest accumulation of strain. This behaviour becomes more evident when increasing the amplitude of the wiggles (or bulges).

Finally, we analyse the case in which we decrease the yield stress instead of increasing (Figure 7.5). This modification will have the opposite effect of the former, on the shape

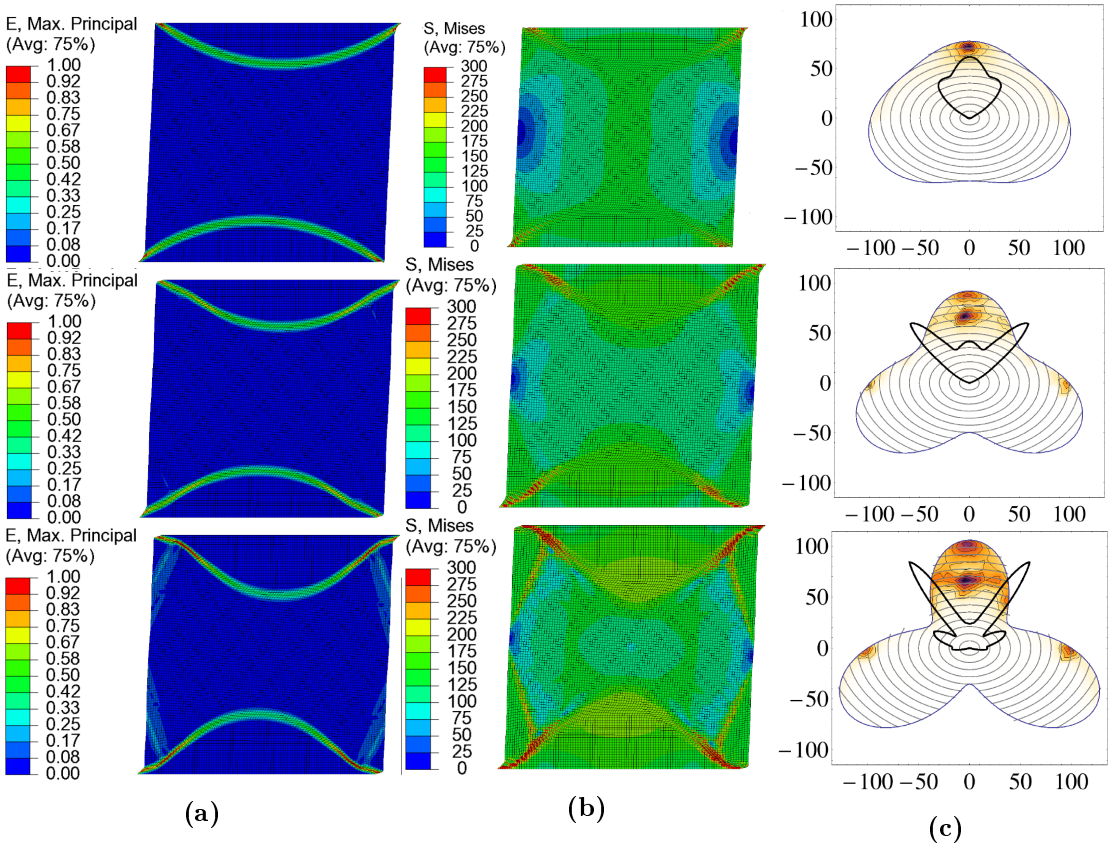

Figure 7.5: Shear test simulation run decreasing the wiggle amplitude: $a = -0.1, -0.3, -0.5$. From left to right: (A) largest eigenvalue of the absolute strain, (B) equivalent von Mises stress, (C) yield limit, density histograms of the stresses and accumulated plastic deformations.

of yield limit. As we can see, shear bands are still forming, going inside the body as we decrease the value of a (7.5a). They neither disappear, nor change direction, as it happened in the previous case. Moreover, the predominant shear stresses decrease, which is also in contrast with the former cases. Eventually, the accumulated plastic strain develops in non-trivial patterns. We see that the behaviour of the structure, especially regarding the shear band formation, is not strictly related to the (non-)convexity of the yield limit. Indeed, strain localization areas are already visible in the case of the von Mises yield limit. The interested reader is invited to refer to Glüge and Bucci [2017], where more outputs are reported and where we also perform cyclic simulations and others, close to the limit case of loss of convexity.

Conclusions

After setting up a simple initial boundary value problem, with a 2D von Mises elastic-plastic material model, we modified it equipping the yield surface with bumps so to obtain a non-convex, anisotropic yield function. In all the cases we observed the localization of the strain which appears to be unrelated (or slightly) to the amplitude of the bumps. Instead, the material anisotropy appears to be responsible for the observed behaviour. We conclude that the non-convexity of the yield function does not affect the qualitative

behaviour of the material in the two dimensional case under study, therefore it does not reflect any material property.

Chapter 8

Meso-scale: the analytical approach to linear elasticity and non-associative plasticity

8.1 Introduction

Non-associative flow rules have always been of great interest not only in the field of geomechanics, when studying granular materials or rocks (Maier and Hueckel [1979], Tejchman [2013]), but also when dealing with microstructured materials like composites, reinforced materials or conrete (Lei and Lissenden [2007], Taherizadeh et al. [2011]). Non-associativity was always connected somehow to anisotropy of the material, both as the effect and the cause of it (Jiang et al. [2012], Manzari and Yonten [2014]). In the case of honeycomb structures, since we assume linearity between $\mathbf{T}$ and $\mathbf{E}$ and an initial isotropic elastic behaviour (see chapter 4), the anisotropy is caused by the growth of plastic deformations (see chapter 5).
In this chapter we will approach the structure from another scale level: we will consider the system of three bars, connected by elastic-plastic springs (see Figure 8.1).

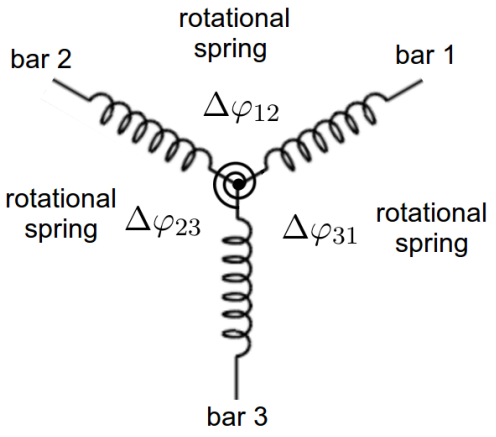

Figure 8.1: Schematic representation of the bar system with springs

The bars will be assumed to be only extensible and periodic boundary conditions will be imposed at the end of each. We will see that the system of equations is closed, and an analytical solution to the stress-strain problem can be found. Therefore, we will build an algorithm which considers a threshold for the variation of the angles, after which the angle variations will be decomposed in elastic and plastic part. The main issue when developing the algorithm is to find out a way to distribute the plastic deformations through the three angles. To this aim, we observe the stress-strain curves found in chapter 5 and compare them with the moment-curvature ones obtained by the analysis of bending beams. We find out that they have the same effective hardening behaviour, even if in the micro-scale model simple plasticity was assumed. Moreover, from the argument of Considére, we know that the plastic hardening resulting from the homogenization plays the main role in the deformations of the bars, until necking occurs. This will allow us to assume that the deformations evolve symmetrically at the joint of the bars, so that when one angle increases of $\Delta\phi_p$ the other two decrease of $\Delta\phi_p/2$ each. Therefore we introduce the formation of plastic hinges, after the threshold angle is surpassed. This results in a simple algorithm, that is able to capture both elastic and plastic behaviour of the microstructured body. As a straightforward outcome of the presented model, we observe a new yield surface, less exhaustive than the one in chapter 5 (the non-convexity is lost) but still catching its main features (symmetry, orientation), and, most important, how it evolves depending on only two scalar plastic state variables.

8.2 Homogenization approach to elasticity

As we learnt in the previous sections, there exist no standard methods to model non-associative plasticity, especially when talking about homogenized continua. Therefore we want to find a simple approach, which is able to capture the main features of our structure. The case of polyethylene non-associativity already motivates us to look for an alternative method which can be adapted to any honeycombs. We want to develop a general procedure that holds for both material cases and that can be extended to all desired materials. To this aim, we use a homogenization approach which considers a system of three extensible bars. We apply the balance of forces and moments, and consider different constitutive equations, describing the behaviour of the bars and the angles between them.

Homogenization of the elastic problem

In this section we try to obtain an analytical homogenized model for the linear elastic behaviour of the honeycomb. We will consider a "Y" shaped system of bars (shown in Figures 8.1 and 8.3) as the smallest repeatable one, which can build the hexagonal shape, if a certain periodicity is assumed (as we did in chapter 5). On this element we will define local quantities which will be related to the average quantities considering the integration over the volume. Notice that from now on we will neglect the existence of the out-of-plane dimension. Our study is completely driven with only two dimensions, which allows us the use of plane stresses without buckling problems in the "z" direction. From a model point of view, using plane stresses or strains does not make a difference, since Hooke's law is valid in both cases. What changes is the stiffness/compliance matrix on the macro scale, influenced by the difference of the stiffness of the bars. In fact, one

can easily observe that in the case of plane stresses, the stiffness of the beam is lower than in the case of plane strains, due to the fact that there are no restrictions on the lateral straining (in the out-of-plane direction). The final aim of the whole procedure is to obtain a homogenized relation able to describe the behaviour of such a structure as if it was a continuum. To this purpose we will adopt a systematic approach which can be outlined as follows:

1. we define average, homogeneous, deformation quantities (using average field theory method, see Hori and Nemat-Nasser [1999], Miehe et al. [2002], Miehe and Koch [2002]): $\overline{\mathbf{H}}$ effective displacement gradient;
2. we define local kinematic quantities which are related to the average deformations;
3. we define local dynamic quantities conjugate to the local kinematic quantities;
4. we introduce constitutive equations between local kinematic and dynamic quantities for the single honeycomb cell;
5. we define effective dynamical quantities from the local ones: $\overline{\mathbf{T}}$ effective Cauchy stresses;
6. we obtain a constitutive homogeneous law $\overline{\mathbf{T}}(\overline{\mathbf{H}})$.

During the whole procedure we will pay particular attention to the number of degrees of freedom (DOF) that we give to the structure and to the number of equations that we write do describe its behaviour.
Since we would like to keep the model the most general as possible, we will consider the structure made of extensible beams. In this way we are able to describe a wider class of honeycomb structures, just through the modification of the bending or axial modulus. Indeed all the already existing models (Gibson and Ashby [1997], Papka and Kyriakides [1998a, 1999b], Wang and Cuitiño [2000]) just focus on the bending properties of the elements, considering classical slender Euler-Bernoulli beams. In this way they ignore the interesting behaviour that the structure shows if one does not neglect the axial deformation. In fact, if instead one considers a thick beam, the axial deformation would be the main contribution to the average deformation[1], leading to an auxetic behaviour of the structure (see Figure 8.2), with a negative Poisson ratio. Moreover, as the plastic deformations concentrate at the joints of the bars, plastic bending along the bars does not contribute to the effective plastic behaviour (as we saw for example in Figure 5.4).

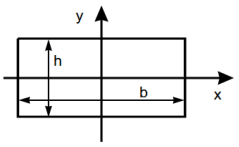

[1] The bending stiffness is proportional to: $I = \frac{bh^3}{12} \propto h^3$; The extension stiffness is proportional to: $A = bh \propto h$

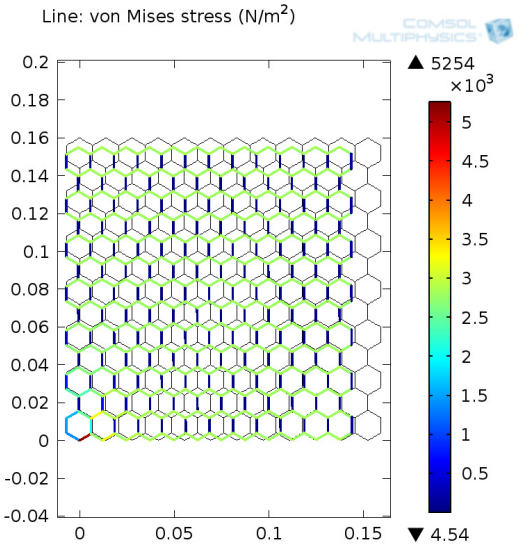

Figure 8.2: A preliminary simulation run with the software COMSOL. In this picture we see the effect of a high bending stiffness versus a low axial one. The thick beams tend to elongate or shorten rather than bend, conferring the peculiar auxetic behaviour to the structure. In black: the reference displacement. In colours: the deformed displacement with von Mises stress.

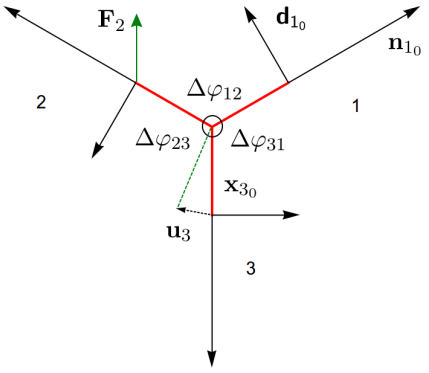

Figure 8.3: RVE system of bars

Local kinematics and dynamic quantities and geometry definition

In the range of small deformations we define:

- the local displacement at the end of the bars 1,2,3

$$\begin{aligned} \mathbf{u}_1 &= \{u_{11}, u_{12}\} \\ \mathbf{u}_2 &= \{u_{21}, u_{22}\} \\ \mathbf{u}_3 &= \{u_{31}, u_{32}\}; \end{aligned} \tag{8.1}$$

- the initial positions of the endpoints of the beams

$$\begin{aligned}\mathbf{x}_{1_0} &= \{\frac{\sqrt{3}}{2}l, \frac{1}{2}l\}\\ \mathbf{x}_{2_0} &= \{-\frac{\sqrt{3}}{2}l, \frac{1}{2}l\}\\ \mathbf{x}_{3_0} &= \{0, -l\};\end{aligned} \tag{8.2}$$

- the initial normal and tangential vectors to the displacement

$$\begin{aligned}\mathbf{n}_{1_0} &= \{\frac{\sqrt{3}}{2}, \frac{1}{2}\}\\ \mathbf{n}_{2_0} &= \{-\frac{\sqrt{3}}{2}, \frac{1}{2}\}\\ \mathbf{n}_{3_0} &= \{0, -1\}\\ \mathbf{d}_{1_0} &= \{-\frac{1}{2}, \frac{\sqrt{3}}{2}\}\\ \mathbf{d}_{2_0} &= \{-\frac{1}{2}, -\frac{\sqrt{3}}{2}\}\\ \mathbf{d}_{3_0} &= \{1, 0\};\end{aligned} \tag{8.3}$$

- the forces applied to each beam

$$\begin{aligned}\mathbf{F}_1 &= \{F_{1_1}, F_{1_2}\}\\ \mathbf{F}_2 &= \{F_{2_1}, F_{2_2}\}\\ \mathbf{F}_3 &= \{F_{3_1}, F_{3_2}\};\end{aligned} \tag{8.4}$$

- the initial plastic deformation of the angles

$$\Delta\varphi_{ij_p} = 0; \tag{8.5}$$

Notice that the subscripts refer to the bars and not to any vectorial relation, unless the quantities are explicitly decomposed, and that the center of the bar system is fixed at $\{0, 0\}$.
Since we want to get the homogenized behaviour of the structure, we need a scale transition from the local, bars scale, to the large, continuum scale. We start our analysis considering extensible bars, joint by rotational springs (see Figure 8.1), subject to local forces. Periodicity is imposed through the balance of forces and moments of momentums (automatically satisfied since they are linearly dependent). Moreover, for any final configuration the bar system can assume, periodicity will be always automatically satisfied by its geometrical properties, as we can see, for example, in Figure 8.4.

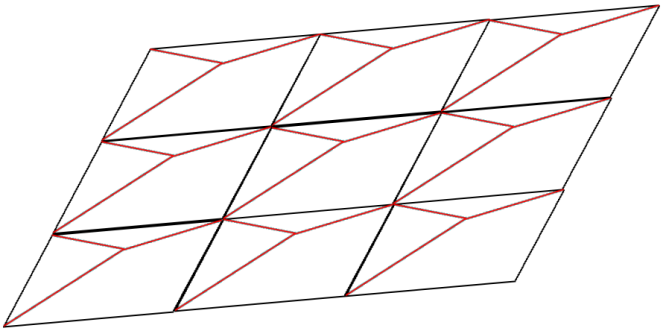

Figure 8.4: Periodicity of the bar system

Since the boundary of the unit cell, $\partial\Omega$, is piecewise continuous, the normal vectors to the displacement, $\mathbf{n}$, at the corners are computed as the average between the limit vectors normal to the two converging sides. The tangential vector, $\mathbf{d}$, is then the unit vector perpendicular to the normal, see Figure 8.3. Remind that the subscripts in the equations indicate the related bar rather than the components of the vectors (only in equations (8.6) and (8.10) vector components are explicit and written with smaller subscripts).

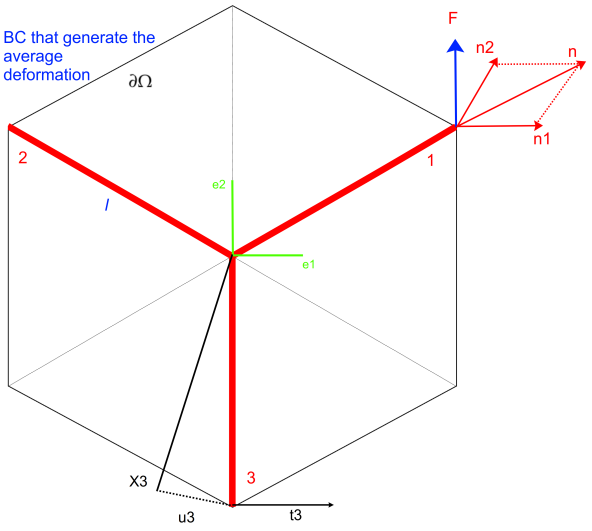

Figure 8.5: Y shape unitary cell with the construction of the outer normal at the corner

Homogenization procedure

1. We start defining the average displacement gradient as (see Hori and Nemat-Nasser [1999], Miehe et al. [2002])

$$\overline{\mathbf{H}} = \frac{1}{V}\int_{\Omega} \mathbf{u} \otimes \nabla \, \mathrm{d}V = \frac{1}{V}\int_{\partial\Omega} \mathbf{u} \otimes \mathbf{n}_0 \, \mathrm{d}A = g(\mathbf{u}_1 \otimes \mathbf{n}_{1_0} + \mathbf{u}_2 \otimes \mathbf{n}_{2_0} + \mathbf{u}_3 \otimes \mathbf{n}_{3_0}) = \\ = g \sum_{0}^{3} \mathbf{u}_i \otimes \mathbf{n}_{i_0} \tag{8.6}$$

where $\mathbf{u}_i$ is the local displacement at the end of each bar, $\mathbf{n}_{i_0}$ the respective initial outer normals and g is a scaling factor arising from the geometrical properties ($g = 3\frac{\sqrt{3}}{2}[\text{mm}^{-1}]$). The second integral is obtained by applying Gauss theorem, while the sum is due to the fact that the problem is a discrete one (only 3 bars).

2. Balance equations of forces and moments applied to each bar, $\mathbf{F}_i$:

$$\begin{aligned} \sum \mathbf{F}_i &= \mathbf{F}_1 + \mathbf{F}_2 + \mathbf{F}_3 = 0 \\ \sum \mathbf{F}_i \cdot \mathbf{d}_{i_0} &= \mathbf{F}_1 \cdot \mathbf{d}_{1_0} + \mathbf{F}_2 \cdot \mathbf{d}_{2_0} + \mathbf{F}_3 \cdot \mathbf{d}_{3_0} = 0 \end{aligned} \tag{8.7}$$

3. Constitutive equations:

$$\begin{aligned} c_{elo} \underbrace{\mathbf{u}_i \cdot \mathbf{x}_{i_0}}_{\Delta l} &= \mathbf{F}_i \cdot \mathbf{x}_{i_0} \\ c_{rot}\, \Delta\varphi_{ij_e} &= (\mathbf{F}_i \cdot \mathbf{d}_{i_0} - \mathbf{F}_j \cdot \mathbf{d}_{j_0})l \\ \forall i, j &= 1, 2, 3, \end{aligned} \tag{8.8}$$

where the first equation considers the elongation of the beams, with elastic modulus c_{elo} [N/mm] and the vectors $\mathbf{x}_{i_0}$ denote the initial positions of the bars. Instead, the second equation considers the rotational springs between the bars (with modulus c_{rot} [N mm], since $\mathbf{d}$ is normalized and therefore dimensionless), as a linear relation for the variations between the angles, namely

$$l\Delta\varphi_{ij} = \varphi_j - \varphi_i = \mathbf{u}_j \cdot \mathbf{d}_{j_0} - \mathbf{u}_i \cdot \mathbf{d}_{i_0}, \tag{8.9}$$

where l is the length of the bar.

4. We define the average stress (see again Miehe et al. [2002], Hori and Nemat-Nasser [1999]) as[2]

$$\begin{aligned} \overline{\mathbf{T}} &= \frac{1}{V}\int_{\partial\Omega} \mathbf{t} \otimes \mathbf{x}\, dA = g(\mathbf{t}_1 \otimes \mathbf{x}_{1_0} + \mathbf{t}_2 \otimes \mathbf{x}_{2_0} + \mathbf{t}_3 \otimes \mathbf{x}_{3_0}) = \\ &= g\sum_0^3 \mathbf{F}_i \otimes \mathbf{x}_{i_0} \end{aligned} \tag{8.10}$$

5. Solving the system of equations (4 in eq. (8.6) + 3 in (8.7) + 5 from eq. (8.8) and (8.9)= 12) in the variables $\mathbf{F}_1, \mathbf{F}_2, \mathbf{F}_3, \mathbf{u}_1, \mathbf{u}_2, \mathbf{u}_3$ (for a total of 12 variables) we can finally get a relation in the form of

$$\overline{\mathbf{T}} = \overline{\mathbf{T}}(\overline{\mathbf{H}}). \tag{8.11}$$

The solution for the problem can be found in the Appendix C.

[2] To prove the validity of the relation, the following chain of argument can be used:

$$V\overline{\mathbf{T}} = \int_V \mathbf{T}\cdot\mathbf{I}\,\mathrm{d}V = \int_V \nabla\cdot(\mathbf{T}^T\otimes\mathbf{x})\,\mathrm{d}V = \int_{\partial V}\mathbf{n}\cdot(\mathbf{T}^T\otimes\mathbf{x})\,\mathrm{d}A = \int_{\partial V}\mathbf{t}\otimes\mathbf{x}\,\mathrm{d}A =$$
$$\int_{\partial V}(\bar{\mathbf{t}}-\tilde{\mathbf{t}})\otimes\mathbf{x}\,\mathrm{d}A = \int_{\partial V}\bar{\mathbf{t}}\otimes\mathbf{x}\,\mathrm{d}A - \int_{\partial V}\tilde{\mathbf{t}}\otimes\mathbf{x}\,\mathrm{d}A = \int_{\partial V}\bar{\mathbf{t}}\otimes\mathbf{x}\,\mathrm{d}A$$

where we used Gauss theorem from the volume to the surface integral and Cauchy theorem to go from the average stress tensor to the local tractions. Then we used the decomposition of the stress field into its homogeneous and fluctuation parts ($\mathbf{t} = \bar{\mathbf{t}} + \tilde{\mathbf{t}}$), from where we get $\int_{\partial V}\tilde{\mathbf{t}}\otimes\mathbf{x}dA = 0$ (see Glüge [2013] eq. 33) if Hill-Mandell condition applies.

Notice: from our model we can get the one of Gibson and Ashby [1997] since, in both models, all the dependencies are linear. Nevertheless, our model is richer because we also consider the extension of the bars (see the second equation of (8.8)).

8.3 Modelling plasticity through plastic hinges

In the previous section, we built a homogenized model for linear elasticity. Now we want to present the plastic one which we develop using an algorithm considering the formation of plastic hinges at the bar's joints. The model is based on the assumption that the plastic deformations, that in our case will be represented by the plastic angle variations, distribute symmetrically on the bars. In the next two paragraphs we will present the rationale that led us to make this assumption. It is based on the observation of the stress-strain curves of the FE simulation, in particular, on their similarities with the bending moment-curvature relation of beams, which present hardening in the effective model, even though not present in the material model. This, together with some observations based on the Considére argument (which he used to model plastic necking), will lead to the conclusion of the symmetric distribution of the plastic deformations in our model. Once again, the whole reasoning is done on three different scale levels: the micro-scale, where von Mises material is considered, the meso-scale, where the beam model is used, and the macro-scale where the hexagonal cell honeycomb is considered. We will see that passing from one scale to the other we obtain different effects, namely the plastic hardening, going from the Mises material to the beam model, and the symmetric angle distribution, going from the beam to the macro structure.

8.3.1 Analysis of the bending moment-curvature relation of beams

In chapter 5, we have studied the RVE problem, assuming von Mises plasticity on the micro-scale. Nevertheless, if we observe the stress-strain curves obtained after FE simulations, we see that the effective model presents some hardening, with a smooth transition from the linear elastic range to the plastic one, which is the reason why we had to use the energy criterion to find the yield point. In that moment we did not stop to ask ourselves, why does this happens. This is the same behaviour that one obtains analysing the bending moment-curvature relation of a simple beam.
Let us assume a slender Euler-Bernoulli beam, with homogeneous, isotropic, linear elastic, perfectly plastic material properties, equal in tension and compression. Moreover let us consider beams whose plane sections remain plane (so that the strain is proportional to the distance from the neutral axis), whose neutral axis passes through the centroid of the rectangular cross section (so that the stress-strain distribution is symmetric) and on which symmetric load (bending moment) is applied. Then, the stresses and strains distributions inside the beam cross section are shown in Figure 8.6: in the first graph, 8.6a, the bending moment did not exceed the elastic regime, therefore, stresses are still linear; in the second one, 8.6b, the yield limit is reached and the outer fibres of the beam plasticize; the stresses present the inelastic region, corresponding to the perfectly plastic behaviour which we assumed; finally, in the last one, 8.6c, the entire section of the beam has plasticized and only inelastic stresses are present (in reality there will always be a small elastic range close to the neutral axes).

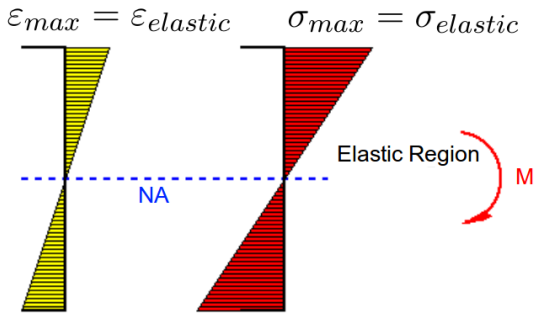

(a) Only elastic deformations

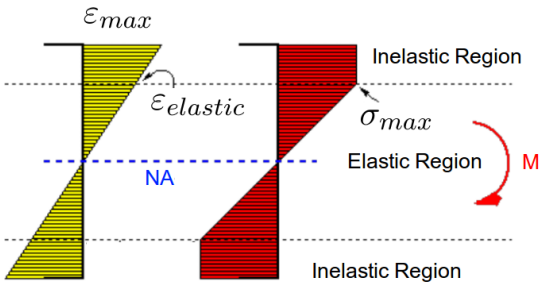

(b) Elastic and plastic deformations

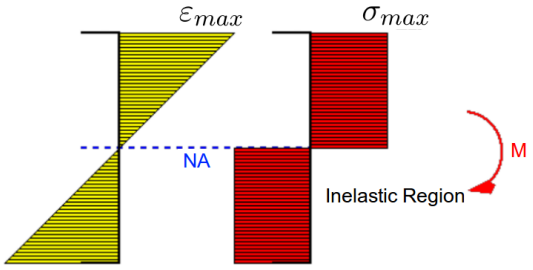

(c) Only plastic deformations

Figure 8.6: Strain and stress distribution in a symmetrically bended beam

Once analysed the stresses and strains distributions in the cross section of the beam, on a micro-scale level, we can try to build the model and find the bending moment-curvature ($M-\kappa$) relation of the homogenized material. Let us consider the beam section of Figure 8.7, where h and b are the dimensions of the rectangular cross section, z is the distance from the neutral axes, z_p is the distance at which plastic strains occur and dA is a small element of area.

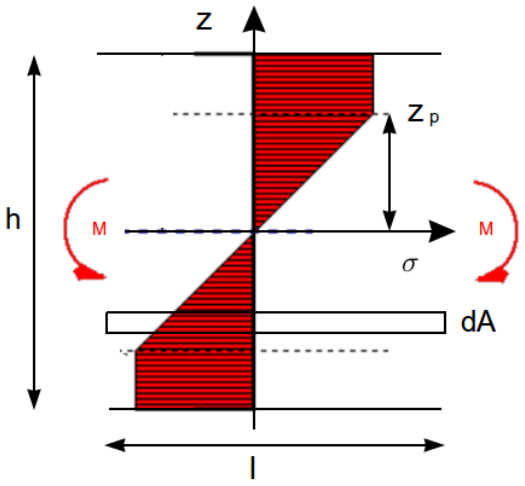

Figure 8.7: Beam cross section with elastic and plastic stress distribution

If we consider the case when just elastic deformations appear (Figure 8.6a), the bending moment is:

$$M = \int \sigma z \mathrm{d}A = \int E\varepsilon z \mathrm{d}A = \int E\kappa z^2 \mathrm{d}A, \tag{8.12}$$

where we used: the Hooke's equation $\sigma = E\varepsilon = E\kappa z$, and Bernoulli's $\varepsilon = \kappa z$, the Young's modulus E and the curvature κ. Since $\mathrm{d}A = b\mathrm{d}z$ we can write:

$$M = \int_{-h/2}^{h/2} E\kappa z^2 b \mathrm{d}z = E\kappa \frac{h^3 b}{12} = EI\kappa, \tag{8.13}$$

where we recognize $I = \frac{h^3 b}{12}$ as the second moment of area for a rectangular cross section. As expected the bending moment is linear in the curvature.
Now let us consider the case in which part of the beam section has plasticized: as shown in Figure 8.7, the linear elastic part is from 0 to z_p and the plastic one, from z_p to $h/2$. Then the bending moment is divided in two parts:

$$M = 2\int_0^{z_p} \sigma z \mathrm{d}A + 2\int_{z_p}^{h/2} \sigma_y \mathrm{d}A, \tag{8.14}$$

where σ_y is the yield stress (we consider twice the same contribution in the integral instead of the full one, because of symmetry). As we did before, we transform and solve the integrals:

$$\begin{aligned} M = 2E\kappa b \int_0^{z_p} z^2 \mathrm{d}z + 2\sigma_y b \int_{z_p}^{h/2} z \mathrm{d}z = 2\frac{\sigma_y}{z_p} b \left[\frac{1}{3}z^3\right]_0^{z_p} + 2\sigma_y b \left[\frac{1}{2}z^2\right]_{z_p}^{h/2} = \\ \sigma_y b \left(\frac{2}{3}z_p^2 - z_p^2 + \frac{1}{4}h^2\right) = \sigma_y h^2 b \left(\frac{1}{4} - \frac{1}{3}\frac{z_p^2}{h^2}\right) = \\ 12\frac{\sigma_y I}{h}\left(\frac{1}{4} - \frac{1}{3}\left(\frac{z_p}{h}\right)^2\right). \end{aligned} \tag{8.15}$$

Writing the solution in terms of the curvature $z_p = \frac{\sigma_y/E}{\kappa}$ (from the Bernoulli hypothesis $\kappa = \varepsilon/z$), we get the quadratic relation between the bending moment and the curvature, resulting in the curve shown in Figure 8.8.

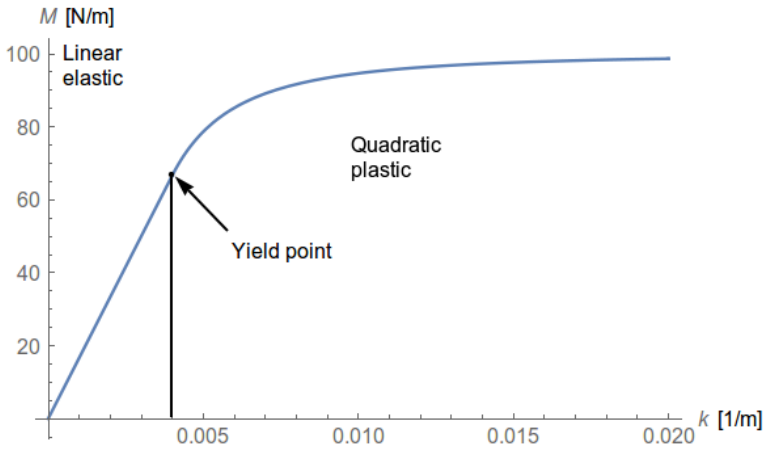

Figure 8.8: Bending moment-curvature relation of the loaded rectangular section beam

Even if there is a smooth transition between elastic and plastic regime, it is easy to find the yield point. Indeed, the first time the beam yields is when $z_p = h/2$ resulting in the bending moment $M_y = \frac{2I\sigma_y}{h}$. On the other hand, the beam is completely plastic when $z_p = 0$ giving the result $M_p = \frac{3I\sigma_y}{h} = \frac{3}{2}M_y$.
Also in this case we see that the effective model presents plastic, **asymptotic hardening**, despite we assumed simple von Mises plasticity, that there is **not a clear point of yielding** in the curve and that the one found analytically is very close to the 10% of change in the curve slope.

8.3.2 The Considére argument

In 1885 Considére wrote about plastic instability concerning necking in bars under tensile tests (Considère [1885]). He wrote that initially, strain hardening compensates for reduction in area and that necking begins when the increase in stress due to decrease in the cross-sectional area is greater than the increase in load bearing capacity of the specimen due to work hardening. That is when instabilities arise. Now, let us consider a specimen under tensile test (Figure 8.9):

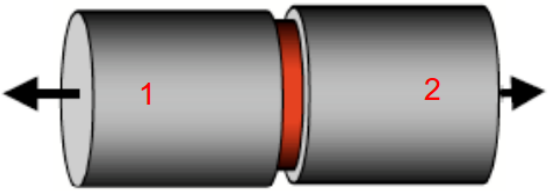

Figure 8.9: Bar specimen under tensile test

We know from the previous theory of plastic bending (8.3.1) that even if the material is assumed to be perfectly plastic, in the effective model there will always be some hardening contribution, due to stress redistribution. If the two parts (Figure 8.9) have exactly the same stress-strain curve it immediately follows that the deformations distribute symmetrically, with respect to the middle line, on sides 1 and 2. Instead, if they have slightly different curves (which is more likely in reality, even if the material is the same), first the weakest will start to harden, as soon as its yield point σ_{y_1} is reached. Nevertheless, as we can see in Figure 8.10, the stresses will continue to increase until also the second part reaches its limit stress, σ_{y_2}. At this point both will harden at the same time and again (dotted red line), the deformations will be symmetric.

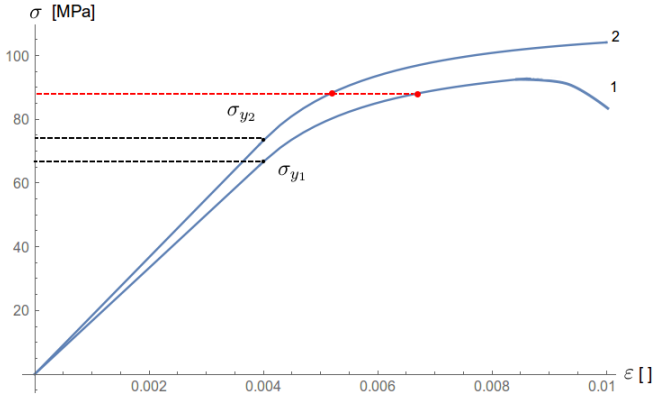

Figure 8.10: Stress-strain curves with hardening, of the two sides of the same specimen

This behaviour will hold until softening takes place. Then the localization of strain starts and necking causes the cross section area to be too small which finally results in the fracture of the specimen.

8.3.3 The plastic hinges model

We will now use all the considerations made in the previous subsections to build a plastic model of the three bars system, based on the symmetric distribution of the deformations (which in our case will be considered as angle variations).
Usually, in structural mechanics, plastic hinges are used to describe the part of a beam where the plastic bending occurs. When a certain value of the moment is passed, transition from elastic to ideally plastic is assumed. The plastic hinge model then allows rotations of the bars at a constant plastic moment. In our case, the yielding moment is described by the second equation in (8.8). Then, we consider the total variation of the angle as:

$$\Delta\varphi_{ij} = \Delta\varphi_{ij_e} - \Delta\varphi_{ij_p}, \tag{8.16}$$

i.e. composed from an elastic, reversible, part $\Delta\varphi_{ij_e}$ and a plastic one $\Delta\varphi_{ij_p}$. Moreover, the additional equation

$$\Delta\varphi_{31_p} = -\Delta\varphi_{12_p} - \Delta\varphi_{23_p} \tag{8.17}$$

can be considered, meaning that the sum of the angle variation is always 0. Equation (8.17) eliminates one degree of freedom, which leaves the plastic problem depending only on two plastic state variables.

At this point the following algorithm is used, in order to find the plastic angles and, therefore, the final configuration of the bars structure:

- Initialize the parameters, equations (8.1) to (8.5)
- Given an average displacement gradient $\overline{\mathbf{H}}$, we divide the path to reach the desired value in m steps, each of them representing a small time increment ($t_m = m\Delta t$)
- Compute $\Delta\varphi_i \quad i = 1, 2, 3$ trough equations (8.6) to (8.10), assuming always the step to be elastic.
- Set an elastic limit in terms of a maximum elastic change of angle, $\Delta\varphi_y$. When this yield angle is exceeded by any one of the three angles between the beams, plastic hinges form in the structure.
- Start decreasing the angle that plasticized by a small δ, which we distribute symmetrically to the other two angles (see paragraphs 8.3.1 and 8.3.2), until it is again in the elastic range. For example, suppose the angle $\Delta\varphi_{12} > \Delta\varphi_y$, then

$$\begin{aligned} \Delta\varphi_{12_e,n+1} &= \Delta\varphi_{12_e,n} - \delta \\ \Delta\varphi_{23_e,n+1} &= \Delta\varphi_{23_e,n} + \delta/2 \\ \Delta\varphi_{31_e,n+1} &= \Delta\varphi_{31_e,n} + \delta/2 \end{aligned} \tag{8.18}$$

- The difference between the actual total $\Delta\varphi$ and the elastic part, will be the updated plastic variation angles

$$\Delta\varphi_{ij_p,n+1} = \Delta\varphi_{ij,n+1} - \Delta\varphi_{ij_e,n+1} \tag{8.19}$$

As we can see in Figures 8.11, with this simple algorithm, the final configuration that the system of bars takes, is plausible and corresponds to our predictions, if one, for example, compares them with the FE simulations of the RVE, in chapter 5.

Conclusions

In this chapter we derived a mechanism-based plasticity model for honeycombs, pointing out once more the need of a different approach to the problem. Therefore, starting from beam theory and hardening arguments, we built a bar model, which is able to reproduce:

- the elastic elongation of the bars;
- the localization of the deformation at the bars joints by introducing there elastic-plastic hinges;
- the symmetric distribution of the deformations when plastic hinges appear.

We see that the algorithm output gives final configurations for the bar system that emulate the ones found in chapter 5 for different prescribed displacements. In chapter 9 we will compare the stress-strain curves resulting from the algorithm with the once resulting from the FE model and observe more interesting properties arising from the developed model. Notice that we are still working on a meso-scale level, where we still consider the cellular structure. In the next chapters we will see what is the effective behaviour resulting from this model.

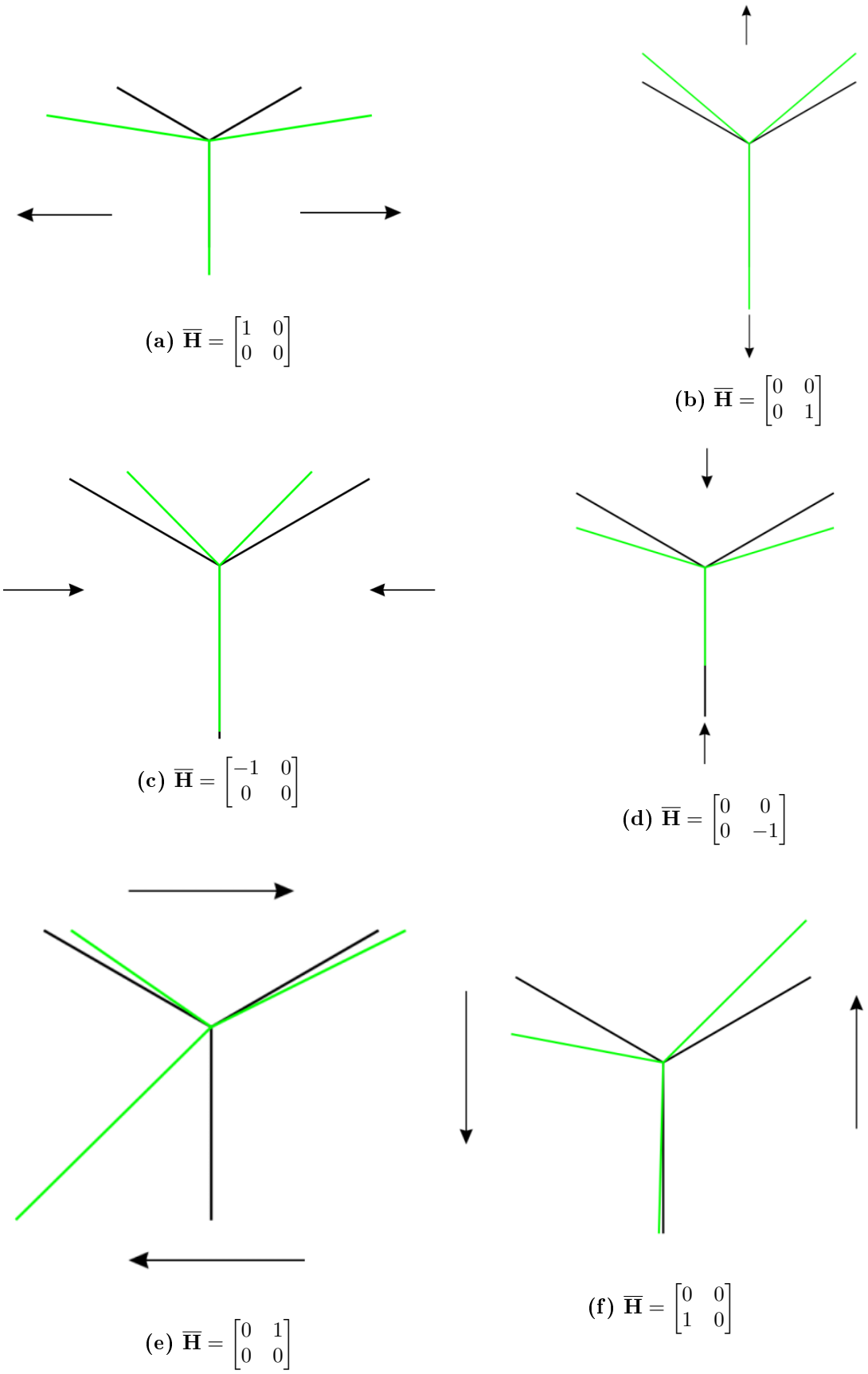

(a) $\overline{\mathbf{H}} = \begin{bmatrix} 1 & 0 \\ 0 & 0 \end{bmatrix}$

(b) $\overline{\mathbf{H}} = \begin{bmatrix} 0 & 0 \\ 0 & 1 \end{bmatrix}$

(c) $\overline{\mathbf{H}} = \begin{bmatrix} -1 & 0 \\ 0 & 0 \end{bmatrix}$

(d) $\overline{\mathbf{H}} = \begin{bmatrix} 0 & 0 \\ 0 & -1 \end{bmatrix}$

(e) $\overline{\mathbf{H}} = \begin{bmatrix} 0 & 1 \\ 0 & 0 \end{bmatrix}$

(f) $\overline{\mathbf{H}} = \begin{bmatrix} 0 & 0 \\ 1 & 0 \end{bmatrix}$

Figure 8.11: Initial (black) and final (green) configurations of the bar system, after different displacement driven tests

Chapter 9

Validation of the model

9.1 Introduction

In chapter 8 we built a model, based on an algorithm, in which different parameters, elastic and plastic, such the stiffness modulus and the yield angle, appear. In a first moment they were assumed to be unitary for simplicity. In this chapter we will see how to calibrate those parameters comparing a simple tension test from the bar model to the same test driven on a numerical simulation with the RVE. Once obtained acceptable values, we use them in other tests and compare the stress-strain curves and the final configurations with the ones from the FE model.

9.2 Calibration

Before being ready to validate our model and compare it with the RVE one, we need to adjust our material parameters to the effective ones. To do that, first of all we have to adapt our code for the bar model such that we can conduct stress driven tests, as the ones done in the FE simulation. The easiest way to accomplish this requirement is to keep our strain driven algorithm and use it in a Newton scheme. Given a stress tensor, the Newton iteration will find the strain tensor such that, through the algorithm, will give as output the prescribed stress tensor. Now we can take the data from one RVE simulation, for example a simple tension test in the x_2 direction, and use them to calibrate the model's parameters so that the stress-strain curves match. To do this we can consider two approaches:

- The **physical** calibration, in which we consider the physical meaning of the c_{elo} and c_{rot} moduli. As they are elastic constants, we fit them considering only the elastic range of the test. We do it in such a way that, given a stress value, the strains in the x and y directions from the two models (RVE and bar) coincide. Finally we adjust the plastic parameter $\Delta\varphi_y$. With this procedure we can see the curves fit in Figures 9.1a and 9.2a with the respective material parameters.
- The **empirical** calibration, in which we treat the variables simply as fitting parameters, and therefore we just find the values which lead to best curve fit. With this kind of calibration we notice some interesting features of c_{elo} and c_{rot}. In

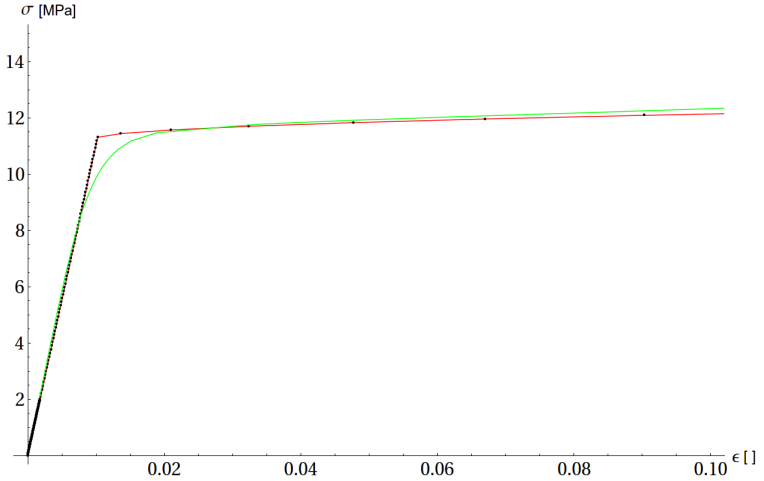

(a) $\Delta\varphi_y = 0.0094,\ c_{elo} = 23.529 * 10^3,\ c_{rot} = 0.696 * 10^3$

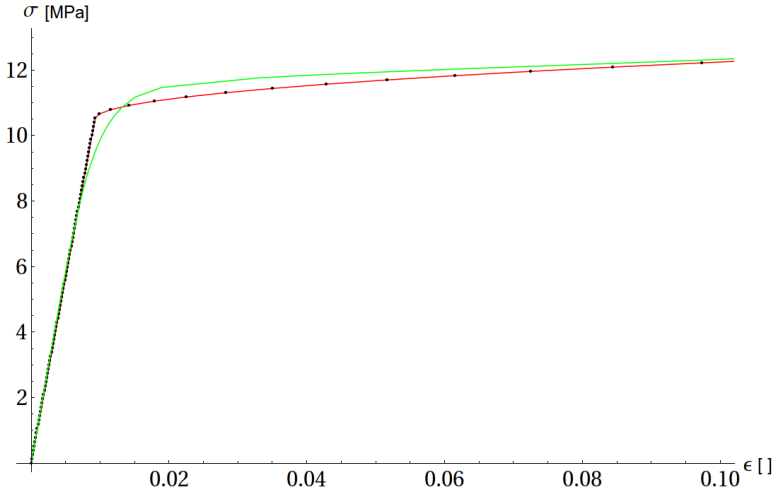

(b) $\Delta\varphi_y = 0.0078,\ c_{elo} = 7.156 * 10^3,\ c_{rot} = 0.784 * 10^3$

Figure 9.1: In red physically and empirically obtained stress strain curves for tension test in y-direction, fitted on the one from RVE simulation in green, for aluminium

fact, we see that, while both control the slope of the linear part, the former is also responsible for the hardening behaviour of the curve (the smaller c_{elo} the more hardening we have), and the latter for the yield point. The best fit curve can be seen in Figures 9.1b and 9.2b, with the respective material parameters.

We see that in both cases, the empirical fit can capture better the behaviour of the curve, since we have more freedom to modify the parameters. Moreover we notice that, because of the non-linear behaviour that the polyethylene shows since the very beginning, the fit results to be harder than in the easier material case of aluminium. Nevertheless, the approximation is good for both materials and is able to catch the main information from the curves, namely the non defined yield point and the hardening behaviour when plastic deformations start.

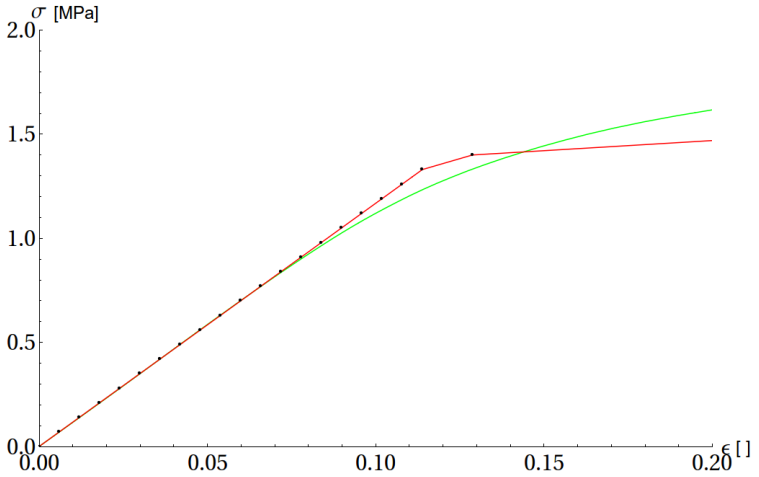

(a) $\Delta\varphi_y = 0.098,\ c_{elo} = 0.078 * 10^3,\ c_{rot} = 0.008 * 10^3$

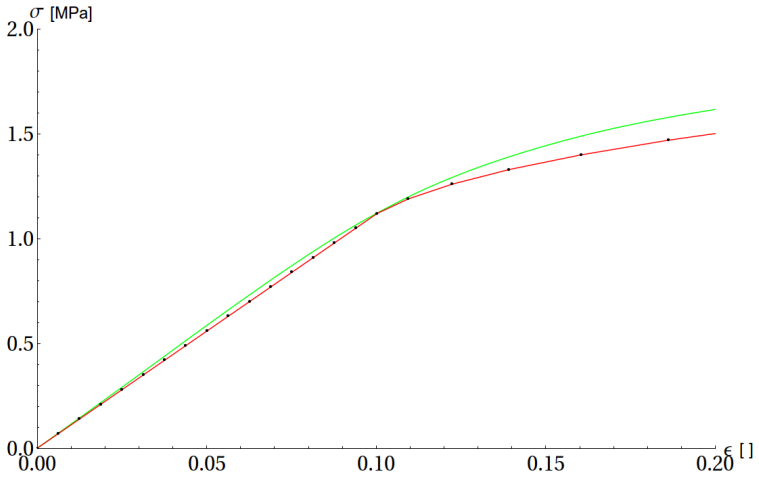

(b) $\Delta\varphi_y = 0.035,\ c_{elo} = 0.019 * 10^3,\ c_{rot} = 0.018 * 10^3$

Figure 9.2: In red physically and empirically obtained stress strain curves for tension test in y-direction, fitted on the one from RVE simulation in green, for polyethylene

9.3 Validation

After calibrating the curves, fitting them on the one obtained from a tension test made on the RVE, we are now ready to see if the model responds correctly to the other tests. We do this still comparing the stress-strain curves obtained from the same tests done using the bar model and the FE simulations. The validation results are shown in Figures 9.3, 9.4, 9.5 and 9.6. From Figures 9.3 and 9.5 (aluminium case) we notice that the model is able to capture very well the curve behaviour both with the physical and empirical fit; in particular we see that, while the physical fit approximates perfectly the linear elastic part, being less precise regarding the yield point and plastic zone, the empirical fit does it very well, but looses precision for the case in red of Figure 9.3b ($\chi = \pi/4$). Instead, concerning the polyethylene (Figures 9.4 and 9.6) we see that the fit matches perfectly only few cases, especially the physical one. We see that the empirical fit in Figure 9.6b captures perfectly both the elastic and plastic part, except for the case $\theta = \pi/5$ for which the model response is weaker than the RVE one. In general, we notice that the model works much better for the aluminium case, which is stiffer and fully linear in the elastic

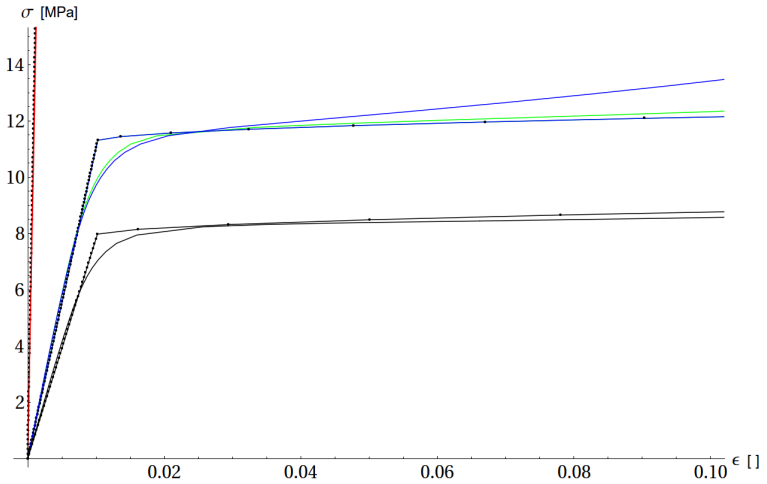

(a) Physical

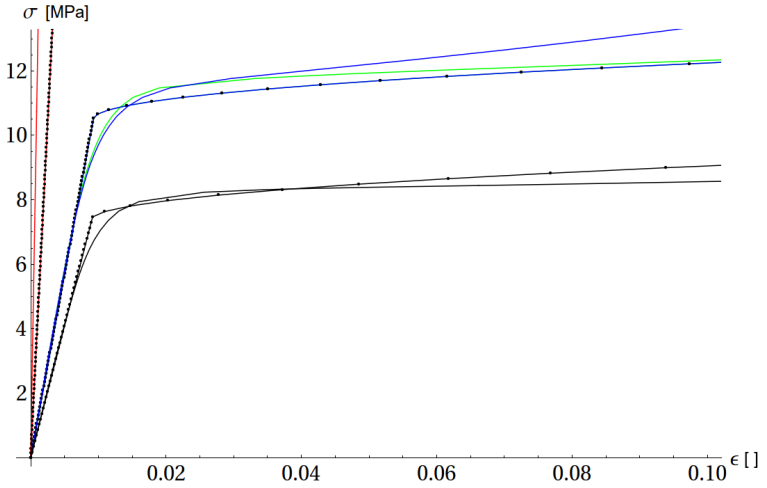

(b) Empirical

Figure 9.3: Curve fits, with dots, for different RVE simulation tests, with constant $\theta = 0$, for aluminium: in green $\chi = 0$, in red $\chi = \frac{\pi}{4}$, in blue $\chi = \frac{\pi}{2}$, in **black** $\chi = \frac{3\pi}{4}$

part, than for polyethylene which presents non-linearities since the very beginning (we already noticed this in chapter 5, figure 5.7b).

Conclusions

In this chapter we compared the stress-strain curves obtained from the RVE simulations and through the bar model algorithm. We see that the model is able to capture quite well, qualitatively and quantitatively, the behaviour of the cellular solid, both for aluminium and polyethylene material cases. In particular, the model is able to reproduce the two most important properties of the effective material:

- first of all, in both models, we find out that there is not a clear yield point appearing in the average stress-strain curves;
- straightforward, we see that in both cases, the effective model presents hardening, even though on the micro-scale level, simple von Mises plasticity was assumed;

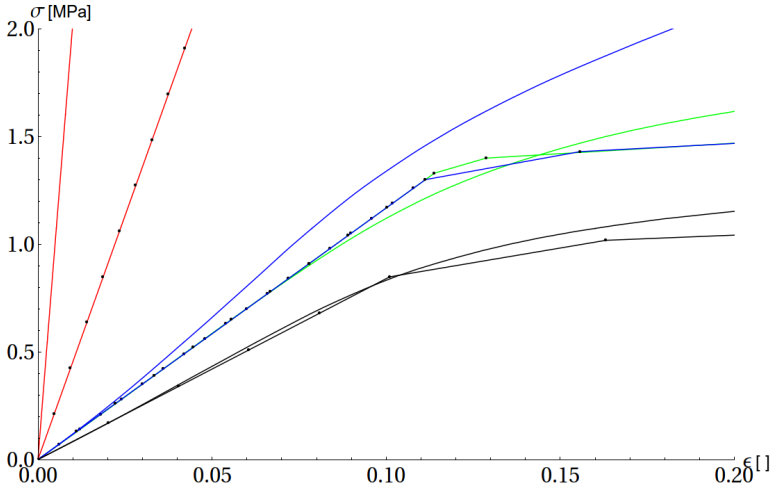

(a) Physical

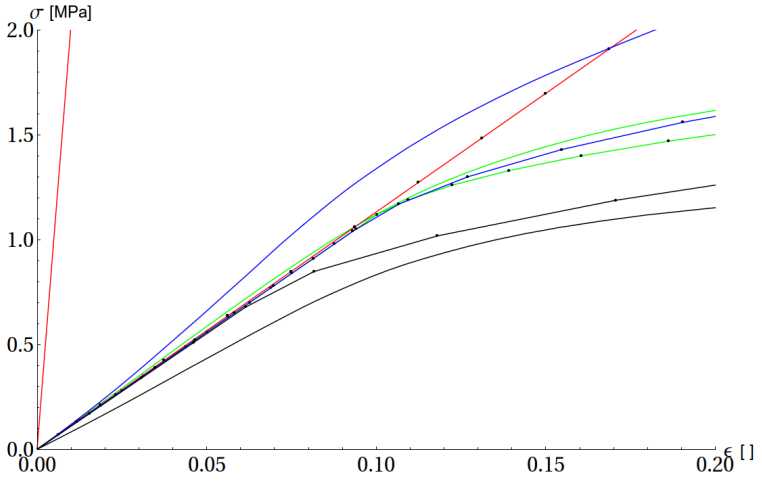

(b) Empirical

Figure 9.4: Curve fits, with dots, for different RVE simulation tests, with constant $\theta = 0$, for polyethylene: in green $\chi = 0$, in red $\chi = \frac{\pi}{4}$, in blue $\chi = \frac{\pi}{2}$, in **black** $\chi = \frac{3\pi}{4}$

These two features are the same which one can observe in the analysis of the bending moment-curvature relation of a beam, as we saw in section 8.3.1.
Next step will be to see what is the effective behaviour resulting from this model when applied to a homogeneous material.

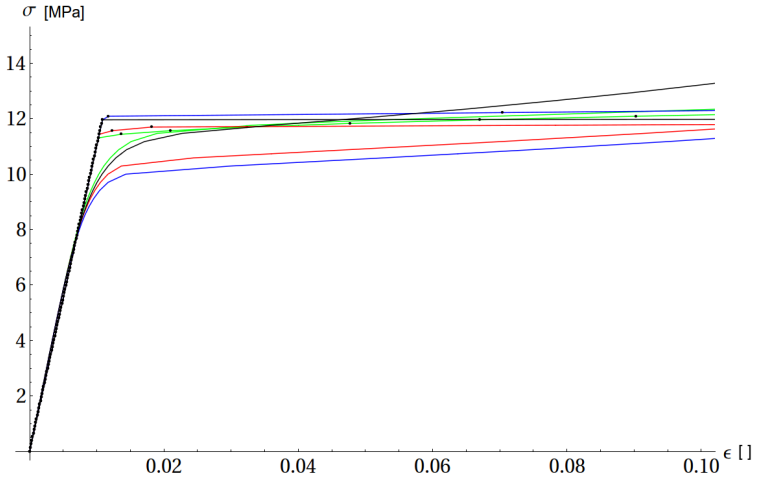

(a) Physical

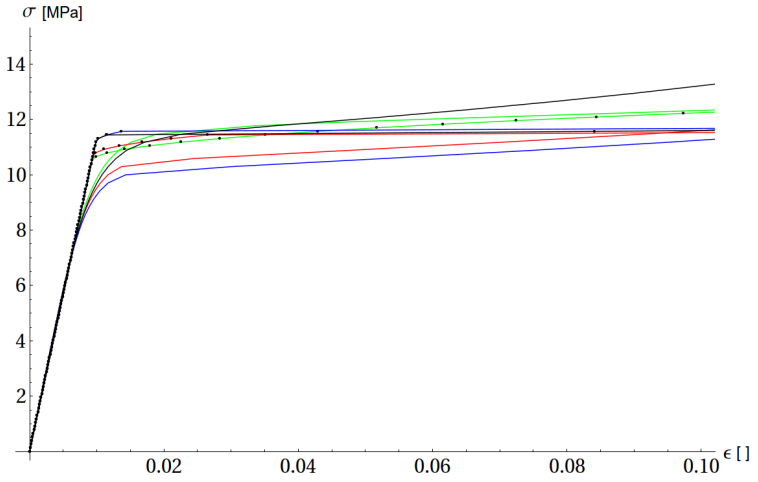

(b) Empirical

Figure 9.5: Curve fits, with dots, for different RVE simulation tests, with constant $\chi = 0$, for aluminium: in green $\theta = 0$, in red $\theta = \frac{\pi}{20}$, in blue $\theta = \frac{\pi}{10}$, in **black** $\theta = \frac{\pi}{5}$

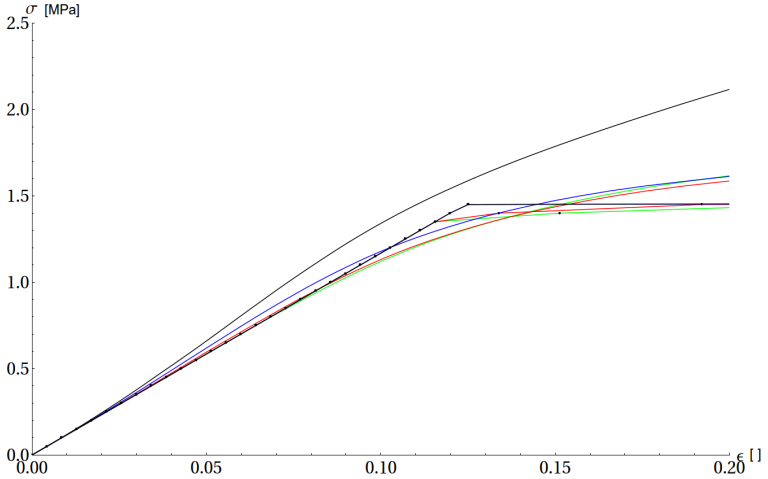

(a) Physical

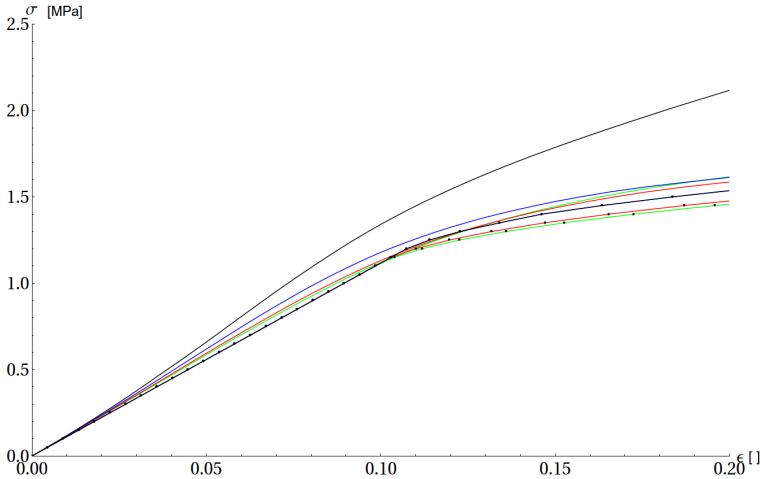

(b) Empirical

Figure 9.6: Curve fits, with dots, for different RVE simulation tests, with constant $\chi = 0$, for polyethylene: in green $\theta = 0$, in red $\theta = \frac{\pi}{20}$, in blue $\theta = \frac{\pi}{10}$, in **black** $\theta = \frac{\pi}{5}$

Chapter 10

Macro-scale II: yield surface and ABAQUS implementation of the meso-scale approach

10.1 Introduction

Up to now, we always focused on our elementary cell, trying to get a behaviour which could correspond to the one observed in a real cell from a honeycomb panel. Nevertheless, the final aim of this work is to forget about the internal structure, and treat the medium as a continuum, still observing the peculiar behaviour of the cellular solid (i.e. strain localization, pressure sensitivity). As a first step into the macro-scale level, we will see the effective yield surface arising from the model on which we plot the plastic flow direction. Two plastic state variables will be sufficient to allow us to study the evolution of the yield surface and confirm that an associative flow rule can not be applied and that neither isotropic, nor kinematic hardening work. Then we will apply all what we learnt, to perform finite element simulations. In order to do this, we build our material model in an ABAQUS UMAT file, in which we implement the plastic model developed in the previous sections, with a more efficient predictor-corrector step approach.

10.2 Evolution of the yield surface

10.2.1 Change of the elastic range

In section 8.2 we set and solve the elastic-plastic problem of the three bars RVE. If we consider equations (8.7), (8.8) and (8.10) we are able to plot the yield surface corresponding to the problem, posed with this new approach, in the stress space. Using the balance of forces and moments

$$\begin{aligned} \sum \mathbf{F}_i &= \mathbf{F}_1 + \mathbf{F}_2 + \mathbf{F}_3 = 0 \\ \sum \mathbf{F}_i \cdot \mathbf{d}_{i_0} &= \mathbf{F}_1 \cdot \mathbf{d}_{1_0} + \mathbf{F}_2 \cdot \mathbf{d}_{2_0} + \mathbf{F}_3 \cdot \mathbf{d}_{3_0} = 0, \end{aligned} \tag{10.1}$$

and the average stress

$$\overline{\mathbf{T}} = g(\mathbf{t}_1 \otimes \mathbf{x}_{1_0} + \mathbf{t}_2 \otimes \mathbf{x}_{2_0} + \mathbf{t}_3 \otimes \mathbf{x}_{3_3}),$$

we can find the expression of the forces in terms of stress components

$$\begin{aligned} F_{11} &= (2\sqrt{3}T_{11} + \sqrt{2}T_{12})/6 & F_{12} &= (\sqrt{6}T_{12} + 2T_{22})/6 \\ F_{21} &= (-2\sqrt{3}T_{11} + \sqrt{2}T_{12})/6 & F_{22} &= (-\sqrt{6}T_{12} + 2T_{22})/6 \\ F_{31} &= -(\sqrt{2}T_{12})/3 & F_{32} &= -(2T_{22})/3. \end{aligned} \tag{10.2}$$

Now, let us recall the constitutive equation for the angle variation (the second of the set of equations (8.8))

$$c_{rot}\, \Delta\varphi_{ij_e} = (\mathbf{F}_i \cdot \mathbf{d}_{i_0} - \mathbf{F}_j \cdot \mathbf{d}_{j_0})l. \tag{10.3}$$

Remembering the Hesse normal form to express a plane in the $\mathbf{R}^3$ Euclidean space, $\mathbf{r} \cdot \mathbf{n} = k$ (where $\mathbf{r}$ is a set of vectors describing all points lying on the plane, $\mathbf{n}$ is the normal vector to the plane pointing away from the origin and k is the distance from the origin to the plane), we notice that the equation above, can represent six planes in the stress space (the same approach is used by Florence and Sab [2005] to study the yield surface and its evolution in the case of a periodic tetrakaidecahedral cellular solid). Therefore, substituting the forces found in (10.2), in the expression (10.3), and considering $\Delta\varphi_{ij_e} = \Delta\varphi_{ij_y}$, i.e. the critical yield angle variation, we can describe the elastic range as all the points falling inside the region defined from

$$\frac{c_{rot}}{l}\Delta\varphi_{ij_y} \geq \mid \mathbf{F}_i \cdot \mathbf{d}_{i_0} - \mathbf{F}_j \cdot \mathbf{d}_{j_0} \mid \tag{10.4}$$

(see Figures 10.1 A and B).

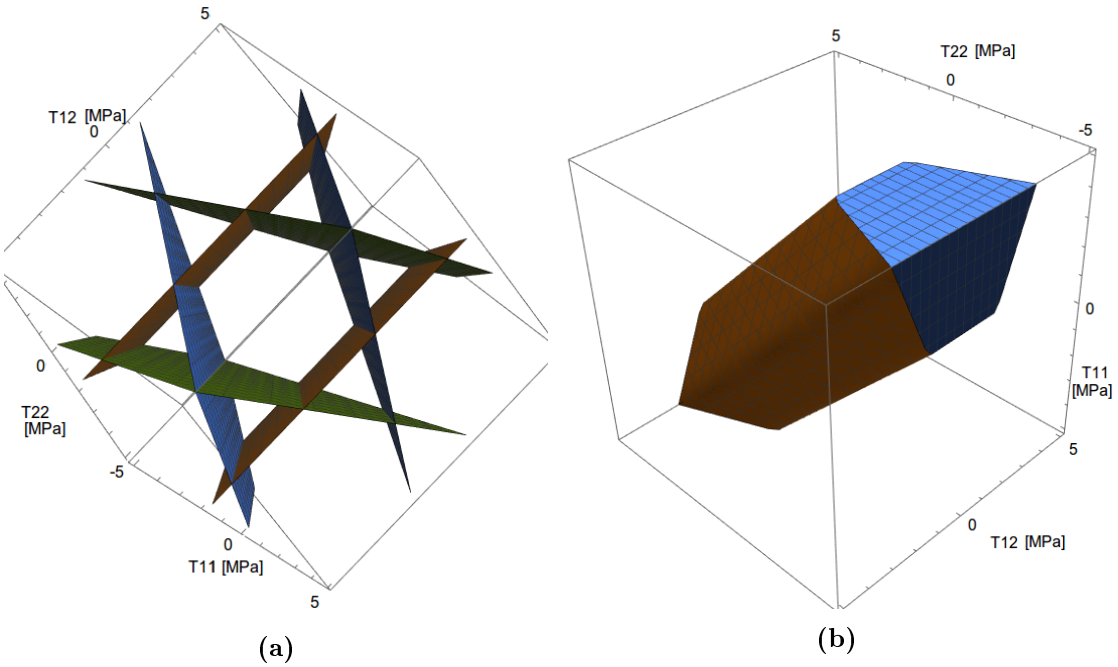

Figure 10.1: (A) Six planes in the stress space defined by (10.3); (B) Hexagonal yield surface in the stress space defined by (10.4)

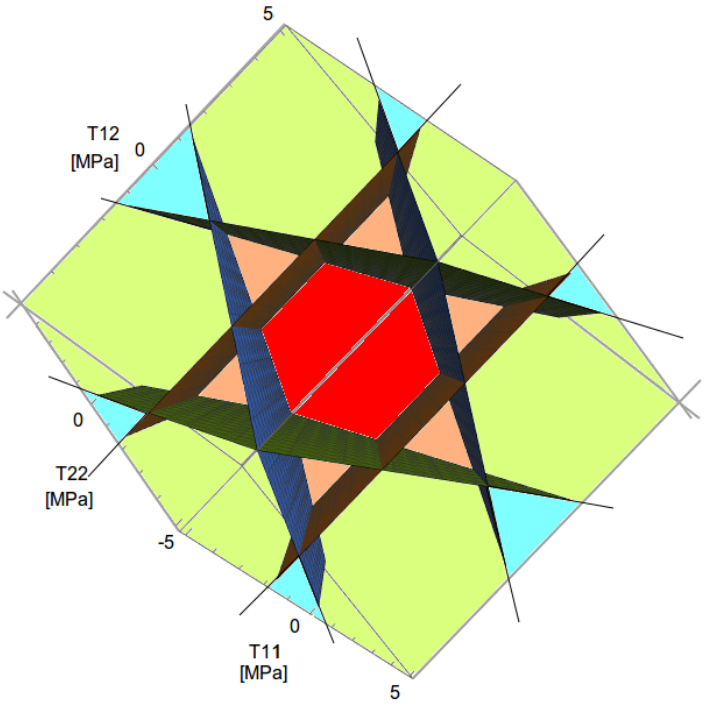

Figure 10.2: Six planes delimiting the elastic range, with different areas in evidence

From the Figures we can recognize some analogies with the yield surface in Figure 5.10: indeed we can identify the six fold symmetry (with the hexagonal shape), the elongation on the tension and compression parts, along the hydrostatic axes. If we have a look at Figure 10.2, we can easily interpret the different areas in evidence: the red part is the elastic range; if we exceed the limit on one side of the hexagon, we are in the pink areas which indicate that only one angle has passed the yield limit; the points where two planes meet indicate that two angles are on the critical value, and in all the green parts they are over it; finally, the blue areas are where three angles yield concurrently. Notice that this last case has to be excluded from the analysis since the predictor step size to reach it would be too big. The cases to consider are only the ones that fall in a small neighborhood of the elastic range.

Unfortunately, but predictably, we loose the information of the non convexity and pressure sensitivity, since the surface extends infinitely along the hydrostatic axis. Nevertheless, this representation of the yield surface allows us to study, with incredible simplicity, its evolution.
To this purpose, let us consider equations (10.4). We know, from the way the model is built, that $\Delta\varphi_{12_p} + \Delta\varphi_{23_p} + \Delta\varphi_{31_p} = 0$. Then we can modify equations (10.4), adding two plastic terms a and b, as state variables, which change the yielding angle as follows:

$$\begin{aligned}
\frac{c_{rot}}{l}\Delta\varphi_{12_y} &\geq a + \mathbf{F}_1 \cdot \mathbf{d}_{1_0} - \mathbf{F}_2 \cdot \mathbf{d}_{2_0} \\
\frac{c_{rot}}{l}\Delta\varphi_{23_y} &\geq -\frac{a}{2} + b + \mathbf{F}_2 \cdot \mathbf{d}_{2_0} - \mathbf{F}_3 \cdot \mathbf{d}_{3_0} \\
\frac{c_{rot}}{l}\Delta\varphi_{31_y} &\geq -\frac{a}{2} - b + \mathbf{F}_3 \cdot \mathbf{d}_{3_0} - \mathbf{F}_1 \cdot \mathbf{d}_{1_0}.
\end{aligned} \tag{10.5}$$

Notice that the first term a is responsible for the symmetric change of the yield surface,

while b for the non-symmetric one. The two state variables basically correspond to a plastic change of the angles $\Delta\varphi$. With this manipulation we can see how the yield surface evolves:

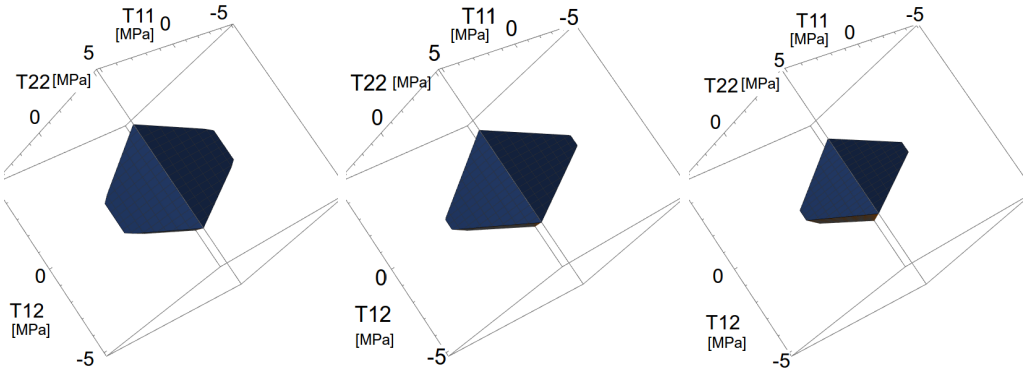

(a) $a = -0.4$, $b = 0$ **(b)** $a = -0.8$, $b = 0$ **(c)** $a = -1.4$, $b = 0$

Figure 10.3: Evolution of the yield surface, changing the first state variable a.

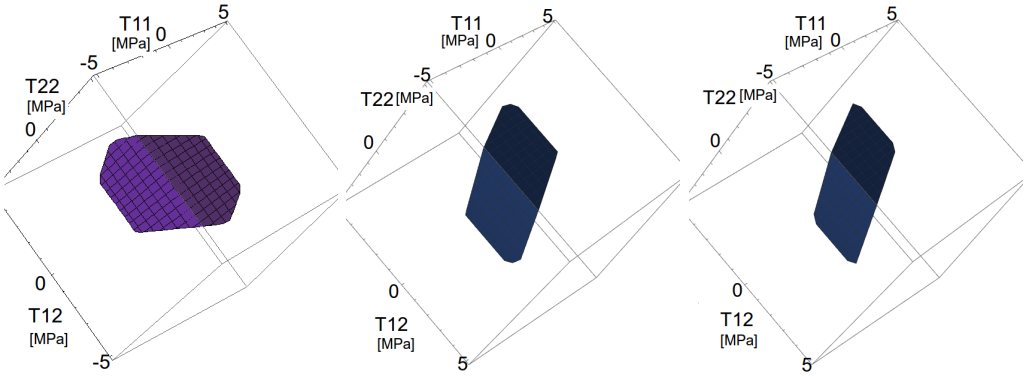

(a) $a = 0$, $b = -0.4$ **(b)** $a = 0$, $b = -0.8$ **(c)** $a = 0$, $b = -1$

Figure 10.4: Evolution of the yield surface, changing the second state variable b.

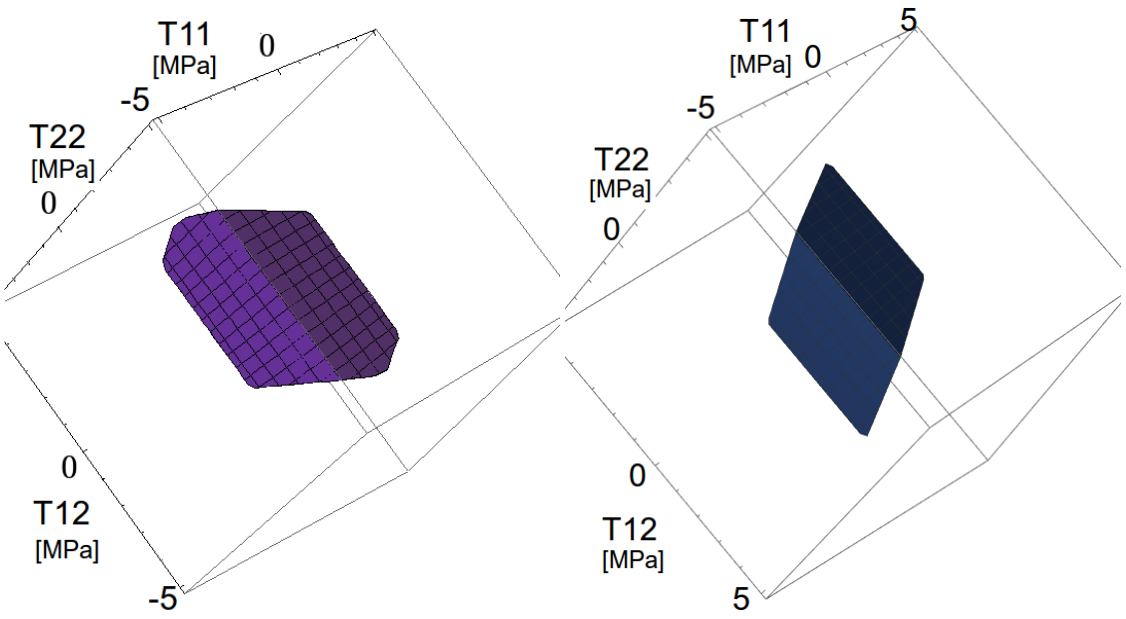

(a) $a = -0.4$, $b = -0.4$ **(b)** $a = 0.4$, $b = -0.8$

Figure 10.5: Evolution of the yield surface, changing both state variables a and b.

From Figures 10.3, 10.4 and 10.5 we can observe some interesting, uncommon, features of the evolution of the yield surface. We notice the loss of the regular hexagonal shape: for example, as we change a, the hexagon flattens symmetrically along the T_{12} direction and elongates along the other two. On the other hand, varying b, leads to a deformation along the T_{12} axes, shearing the sides of the hexagon. Finally, if we change both of the parameters simultaneously, we can see the two effects acting together on the surface. This behaviour cannot be accounted neither for isotropic nor kinematic hardening models and is called distortional hardening (see Ortiz and Popov [1983], Shi and Mosler [2013], Feigenbaum and Dafalias [2007], Manopulo et al. [2015] for more examples on distortional hardening). Another interesting fact is that, after a certain value of the parameter a (in this case after $a = -0.8$), the shape of the surface cease changing anisotropically and starts to shrink showing a softening behaviour, until it disappears. Of course this is a non-physical, limit case because it would mean that the elastic range disappears and only plastic deformations are taking place.

10.2.2 Plastic flow direction

Another advantage of using the algorithm presented in section 10.3 is that it allows us to study the flow direction. Indeed, it can be used as a flow rule to find the vectors indicating the plastic flow direction, in the stress space where we plot the yield surface. To do this, we need to find a way, in our Mathematica codes, to relate the change of plastic strains to the stresses. Once more we will make use of the relations presented in chapter 8 and the algorithm. We solve the equations stepwise in function of the angle variations and substitute the results in the expressions for $\overline{\mathbf{H}}$.
Let us start with a further assumption: we force the relations between u_{i1} and u_{i2} such

that the bars do not elongate, i.e. we assume displacements parallel to $\mathbf{d}_{i_0}$

$$\begin{aligned}\mathbf{u}_1 &= \{u_{11}, \frac{-u_{11}}{\arctan(\pi/3)}\}\\ \mathbf{u}_2 &= \{u_{21}, \frac{u_{21}}{\arctan(\pi/3)}\}\\ \mathbf{u}_3 &= \{u_{31}, 0\}.\end{aligned} \tag{10.6}$$

In this way we suppress a variable and we can write $\overline{\mathbf{H}}$ as function of only u_{11}, u_{21} and u_{31}. Then we solve the equations for the angles variations of (8.8), in function of the displacements. Notice that only two of the three displacements can be used, since the third one is linearly dependent. Therefore, to eliminate the last variable, we solve $H_{12} = H_{21}$ for u_{31}, i.e., we find the displacement such that the matrix becomes symmetric, therefore excluding rigid rotations of the cell. We get the following:

$$\overline{\mathbf{H}} = \begin{bmatrix} \frac{3\Delta\varphi_{12}\arctan(\pi/3)}{\sqrt{3}+\arctan(\pi/3)} & -\frac{\Delta\varphi_{12}+2\Delta\varphi_{23}}{\sqrt{3}+\arctan(\pi/3)} \\ -\frac{\Delta\varphi_{12}+2\Delta\varphi_{23}}{\sqrt{3}+\arctan(\pi/3)} & -\frac{3\Delta\varphi_{12}}{3+\sqrt{3}\arctan(\pi/3)} \end{bmatrix}. \tag{10.7}$$

The next step is to write the angles variations as a function of the stresses. To do this, we substitute the expression for the forces (10.2) in the second of (8.8). Then we can write the elastic angle variation in function of the stresses, which will give us the elastic part of $\overline{\mathbf{H}}$:

$$\begin{aligned}\Delta\varphi_{12e} &= \frac{-T_{11}+T_{22}}{\sqrt{3}c_{rot}l}\\ \Delta\varphi_{23e} &= \frac{\sqrt{3}T_{11}+6T_{12}-\sqrt{3}T_{22}}{6c_{rot}l}\\ \Delta\varphi_{31e} &= \frac{\sqrt{3}T_{11}-6T_{12}-\sqrt{3}T_{22}}{6c_{rot}l}.\end{aligned} \tag{10.8}$$

At this point the algorithm described in section 10.3 must be used in order to find the plastic angles (written in function of the stress tensor components). The so found $\Delta\varphi_p$, once inserted in equation (10.7) will give us the plastic flow direction in the stress space. For the complete Mathematica scripts, look at the Appendix D. The results obtained with this procedure are reported in Figure 10.6.

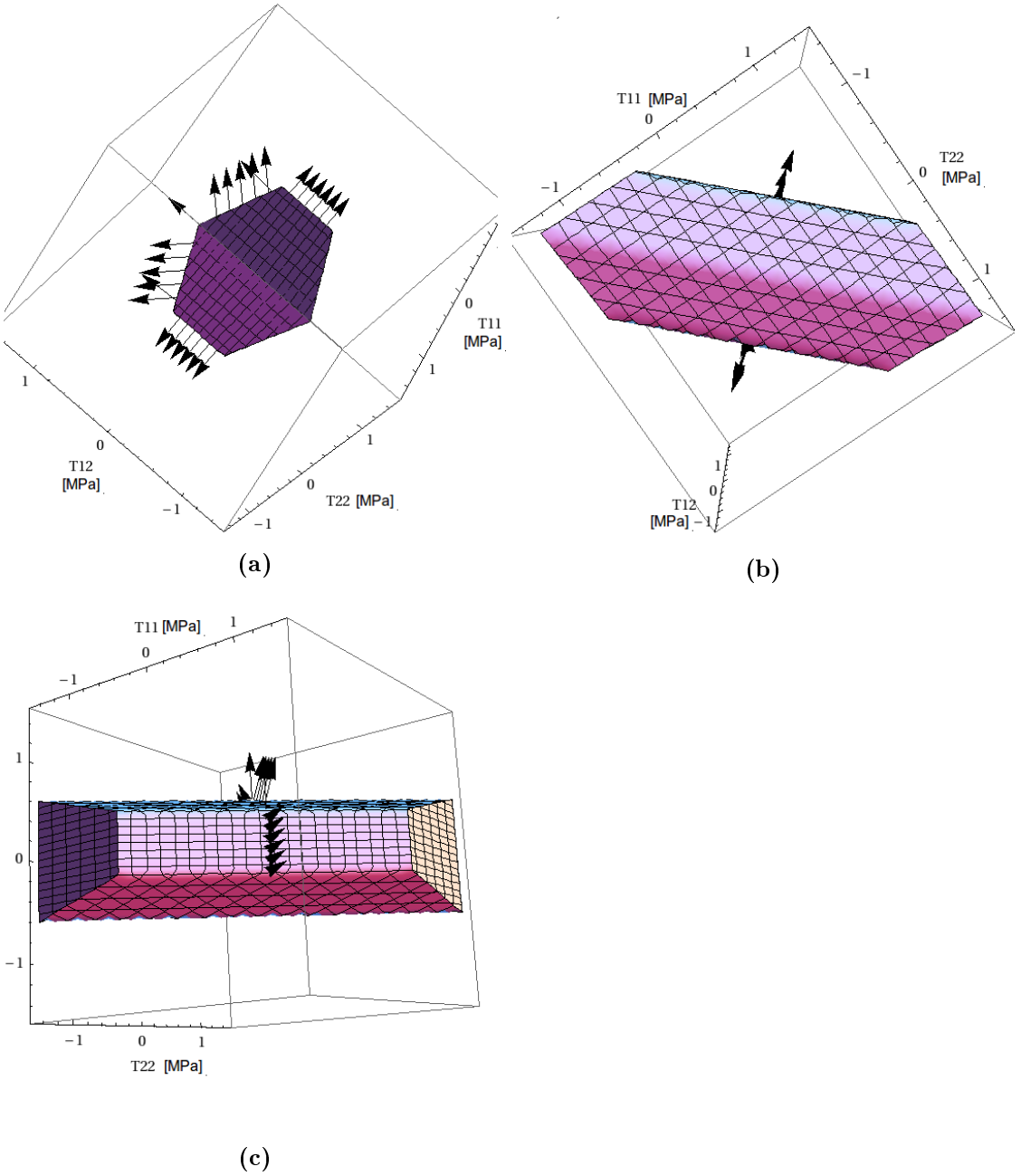

(a) **(b)**

(c)

Figure 10.6: The yield surface with a part of vectors showing the flow direction (then the solution is symmetric).

From this figures we can see that the plastic flow is normal to the yield surface only from the perspective of the T_{12} axes 8.6a. This is lost in the other perspectives. In particular, in Figures 10.6b and 10.6c, we see that the plastic flow has a component along the hydrostatic axis, suggesting compressible plasticity. Indeed, the material presents a volume change, as we can see from the experimental results, due to the collapse and compactification of the rows. Moreover we can see the sudden change of direction of the arrow on the corners, maybe due to a kind of singularity of the surface. In fact, that is the point where two surfaces meet, meaning that two angles yield simultaneously.

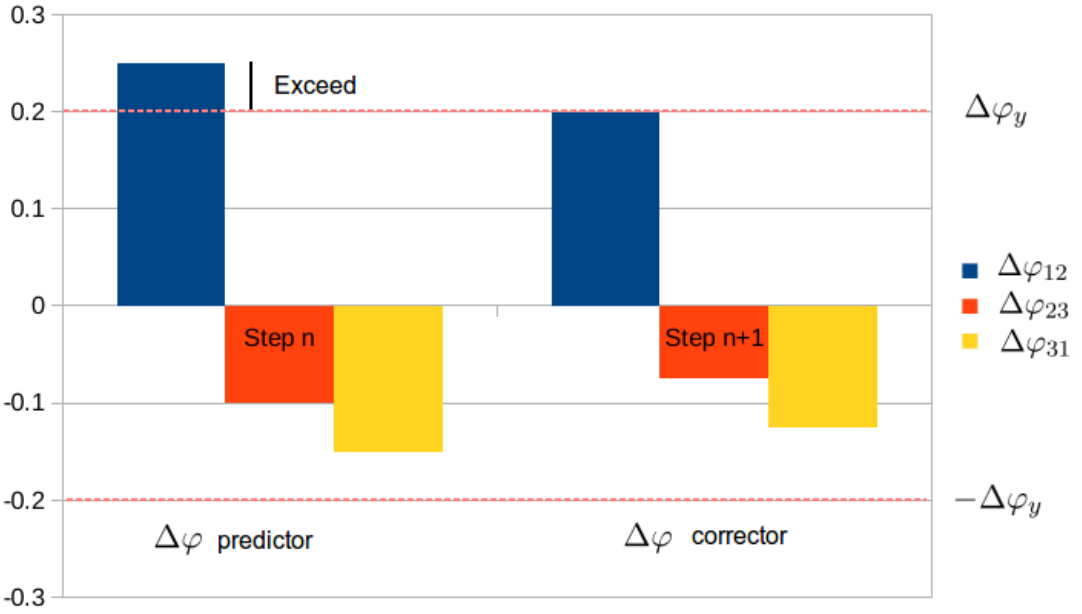

Figure 10.7: Case 1: only one angle exceeds the limit angle $\Delta\varphi_y$

10.3 Implementation in ABAQUS

10.3.1 The predictor corrector algorithm

From the analysis of the plastic step increment, we notice that the final distribution of the angle variation can be summarized in the following way:

Case 1 If only one angle, say $\Delta\varphi_{12}$, exceeds the yield limit, by a quantity that we call ex ($ex = \Delta\varphi_{12_{pred}} - \Delta\varphi_y$), then the corrector step is:

$$\begin{aligned} \Delta\varphi_{12_c} &= \Delta\varphi_y \\ \Delta\varphi_{23_c} &= \Delta\varphi_{23} + ex/2 \\ \Delta\varphi_{31_c} &= \Delta\varphi_{31} + ex/2 \end{aligned} \tag{10.9}$$

Figure 10.7.

Case 2 If two angles, say $\Delta\varphi_{12}$ and $\Delta\varphi_{23}$, exceed the limit, then:

$$\begin{aligned} \Delta\varphi_{12_c} &= \Delta\varphi_y \\ \Delta\varphi_{23_c} &= -\Delta\varphi_y \\ \Delta\varphi_{31_c} &= 0, \end{aligned} \tag{10.10}$$

Figure 10.8.

Case 3 If the three angles exceed the limit then:

- If $\min(|\ \Delta\varphi_{12} - \Delta\varphi_{13}\ |, |\ \Delta\varphi_{23} - \Delta\varphi_{13}\ |, |\ \Delta\varphi_{12} - \Delta\varphi_{23}\ |) \leq \Delta\varphi_y$, then apply [Case 1] where the biggest $\Delta\varphi$ goes to the limit and the other two share the angle excess;

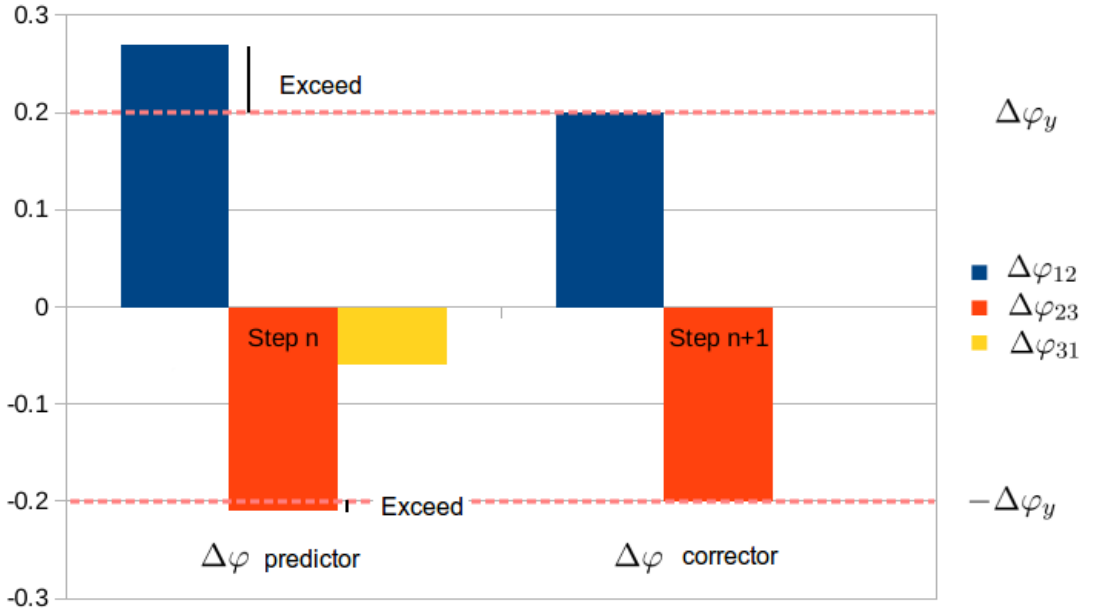

Figure 10.8: Case 2: two angles exceed the limit angle $\Delta\varphi_y$

– If $\min(|\Delta\varphi_{12} - \Delta\varphi_{13}|, |\Delta\varphi_{23} - \Delta\varphi_{13}|, |\Delta\varphi_{12} - \Delta\varphi_{23}|) \geq \Delta\varphi_y$, then apply [Case 2] where the smallest $\Delta\varphi$ goes to 0 and the other two go to the limit with opposite sign.

Here the subscript c stands for "corrector".
Using these conditions instead of the stepwise algorithm, the final result is the same, but obtained in just one iteration. The difference between the two approaches would be as small as δ. The new approach, then, is applied to an homogeneous, 2D, sheet of material which we fix at the bottom, and on which we impose a displacement on the top (see Figure 10.9).

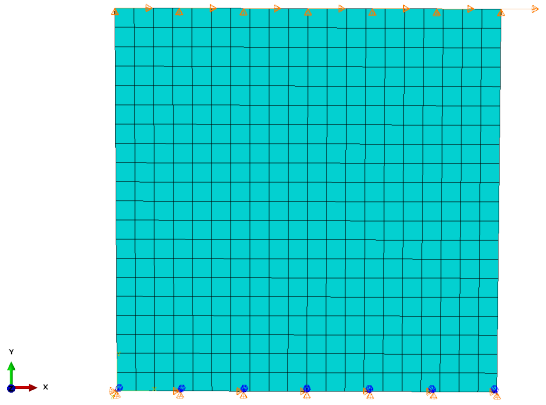

Figure 10.9: 2D, homogeneous structure, with mesh and boundary conditions

For these simulations we can either use the parameters found with the curves fitting, or the material parameters given from the geometry of the bars. For the latter case we use the following:

$c_{elo}[N/m]$	20.96
$c_{rot}[Nm]$	17.29
$\Delta\varphi[]$	0.2
$l[m]$	1

Table 10.1: Material parameters

where c_{elo} and c_{rot} are computed respectively: $c_{elo} = AE/l$, i.e. the stiffness for a rectangular bar, where A is the cross-section area, E is the Young modulus of the base material (in this case we use aluminium) and l is the length of the bar; c_{rot} instead is the stiffness extracted from the stress-strain curve of a compression test. We also report the output using the constitutive parameters obtained with the empirical calibration of polyethylene (which results to be more significant than the one of aluminium, although not really representative of the honeycomb structure behaviour).
For the UMAT.f file, look at the Appendix E.

10.3.2 Observations on the algorithmic consistent linearization

As we can see in the Appendix E our material model has been implemented as a user material in ABAQUS UMAT (see section 6.2). It is worth now to spend some time to point out another advantage of the developed algorithm.
To write a user material some important quantities must be defined, that are the stresses and the dependence on field variables or internal state variables. Moreover, one has to write the constitutive rate equations as incremental equations. Then ABAQUS uses the Newton scheme, to find the $\mathbf{f}_{int}(\mathbf{u})$ such that $\mathbf{r}(\mathbf{u}) = \mathbf{f}_{int}(\mathbf{u}) - \mathbf{f}_{ext} = 0$ at each step increment. This can be linearized as follows

$$\mathbf{0} = \mathbf{r}(\mathbf{u}) \approx \mathbf{r}(\mathbf{u}_n) + \frac{\partial \mathbf{r}(\mathbf{u})}{\partial \mathbf{u}}|_{\mathbf{u_n}}(\mathbf{u}_{n+1} - \mathbf{u}_n) = \mathbf{r}(\mathbf{u}) + \mathbf{J}(\mathbf{u}_{n+1} - \mathbf{u}_n),$$

and solved for

$$\mathbf{u}_{n+1} = -\mathbf{J}^{-1}\mathbf{r}_n + \mathbf{u}_n.$$

To do this, the Jacobian has to be provided and can be decomposed by the chain rule as follows:

$$\frac{\partial \mathbf{r}_{n+1}}{\partial \mathbf{u}_{n+1}} = \frac{\partial \mathbf{r}_{n+1}}{\partial \mathbf{T}_{n+1}} \frac{\partial \mathbf{T}_{n+1}}{\partial \mathbf{E}_{n+1}} \frac{\partial \mathbf{E}_{n+1}}{\partial \mathbf{u}_{n+1}}.$$

The first and last terms are constant element matrices, given from the element formulation, while the middle term needs to be explicitly defined by the user. The problem of defining a consistent Jacobian or "algorithmically consistent tangent moduli" was firstly recognised by Simo and Taylor [1985]. In fact, many constitutive models commonly used in solid mechanics are very difficult to linearize exactly, which creates a need for effective approximations of material stiffness. For a deeper discussion on the argument, refer to Laursen [2013].

This definition involves the use of a time integration algorithm, and here is where our enters: we build a backward algorithm, similar to the backward Euler method, which evaluates the stresses at the end of each time increment, in such a way that they always lie on the yield surface if the yield limit is reached, and are elastic otherwise. The stiffness matrix $\mathbb{K}_{n+1} := \frac{\partial \mathbf{T}_{n+1}}{\partial \mathbf{E}_{n+1}}$ is computed componentwise by numerical differentiation as follows:

$$K_{ijkl} \approx \frac{T_{ij}(\mathbf{E} + \Delta\mathbf{E}) - T_{ij}(\mathbf{E})}{\Delta E_{kl}},$$

for which we just have to define the function $\mathbf{T}(\mathbf{E})$.

10.3.3 Results

In the following figures we report the final configurations of the material sheet under different loading conditions, obtained using the user material implemented in UMAT.

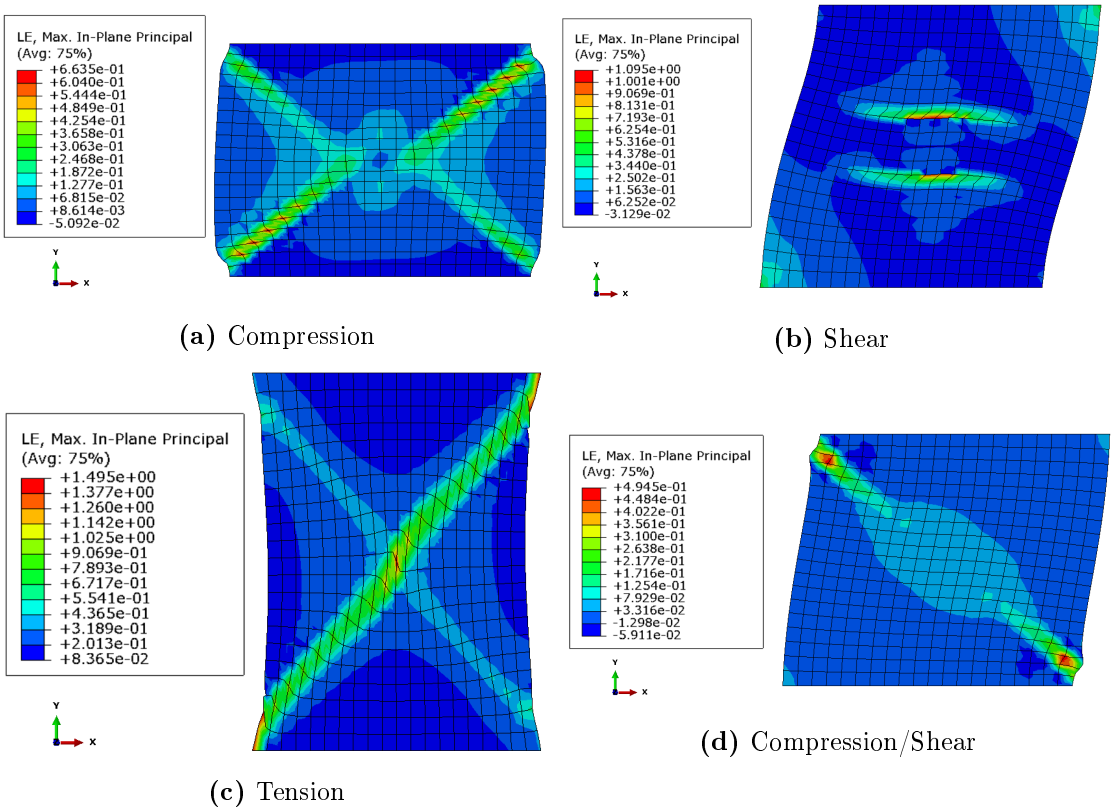

(a) Compression **(b)** Shear

(c) Tension **(d)** Compression/Shear

Figure 10.10: Final configuration under different loading conditions using the material parameters of table 10.1. In the scale of colours equivalent strains are reported

Figures 10.10 are obtained using the geometrical material parameters. They show explicitly the localization of the deformation. For each loading condition we can appreciate the appearance of deformation bands. In particular, for the cases of compression and tension, we see the deformation propagating from the corners to the centre of the body, whereas, in the other two cases, it concentrates immediately in the centre. The rest of the square, instead, remains homogeneous and almost free of deformation. This behaviour is very typical for complex materials, whose mechanical behaviour is well modelled by

second (or higher) order gradient theories (see for example Reiher et al. [2016]). Nevertheless, the aim of this study is to keep our description simple and easily handleable for engineering purposes. Further complexity can be added to the proposed approach and will be discussed in the final outlook of this thesis.

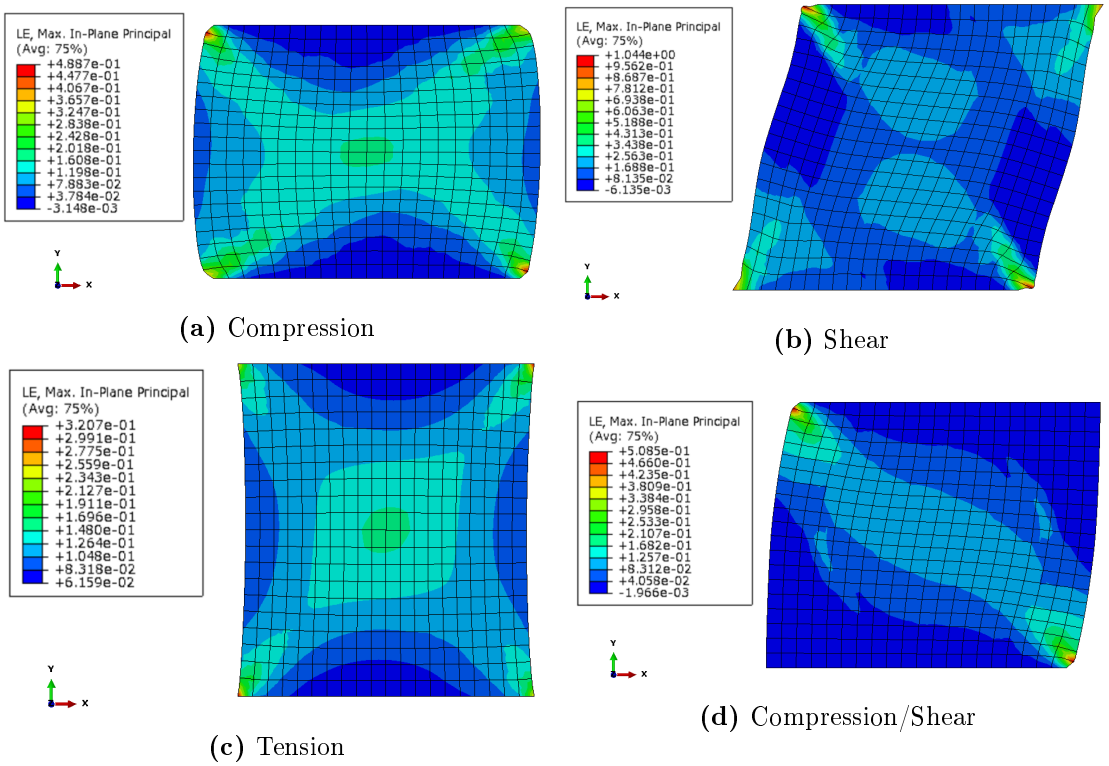

(a) Compression

(b) Shear

(c) Tension

(d) Compression/Shear

Figure 10.11: Final configuration under different loading conditions using the parameters for polyethylene empirical fit (Figure 9.2b). In the scale of colours equivalent strains are reported

On the other hand, Figures 10.11 show the results for the fitted parameters. We can see that the localization of the deformation always starts at the corners of the specimen. For each loading condition we can just appreciate the starting of deformation bands. It is important to observe that, what we can actually see in this second case, are only the initializations of the localization. This is because, as soon as the deformations start to localize, large strains occur. This is one limitation of the model and therefore the first modification that one would start to investigate. In both cases, upgrading the model to large deformations could result in a better representation of the plastic strain localization.

Notice that, since there is no internal scale, a mesh dependence of the final result is unavoidable. Nevertheless, it can be overcome by adding a viscosity term in the model, which can be tuned to uniform the results obtained with different mesh sizes. Indeed, as widely explained in Niazi et al. [2013], Needleman [1988], Peerlings et al. [1998], including a regularizing viscosity in the model means introducing an internal length scale. Then the localization size correlates with the viscosity parameters which can be varied to fit the experimental results (see also De Borst et al. [1993], Dias da Silva [2004]).

Conclusions

In this last chapter we saw that not only is the model able to capture the behaviour shown by the RVE, but it also allows us to study further the characteristics of the yield surface and investigate its evolution. We confirm that the associative flow rule does not apply to the cellular material, being indeed a compressible one, and that distorsional hardening is present in the plastic behaviour. This is one of the most important achievements of the model, since it is able to represent the evolution of the yield surface, when one would not know what to do because of the big functional freedom of the problem. Obtaining the same result through FE approach, would require an excessive number of simulations, if one wants to consider all possible loading paths.
We saw that, once implemented in a finite element software as a user material, the model is able to capture the localization of the deformations in shear bands and its initialization, typical of honeycomb-like structures.

Chapter 11

Conclusions and outlook

11.1 Conclusions

In the presented work we studied and examined the elastic-plastic behaviour of honeycomb structures made of two different materials: aluminium and polyethylene. We approached the structure on three different levels: micro-, meso-, and macro-scale. At each level we faced different problems: parametrization of the stress tensor and the mathematical fit of the yield surface, at the micro-scale; properly modelling the cell structure and finding a good algorithm for its plastic behaviour, at the meso-scale; finding the good material parameters and a finite element implementation, at the macro-scale.
In order to easily preform numerical simulations, we parametrized the stress tensor with the three parameters, i.e. the *magnitude* of the load m, the *orientation angle* θ and the *biaxiality measure angle* χ, and used them to find a mathematical expression for the yield surface, based on observations of symmetry properties. It turned out to be a very complex one, non-classical and above all, non-convex, for both material cases. As a general outcome, we learned that aluminium responds in a stiffer way than polyethylene, conferring it smoother and more regular properties. Nevertheless, not excluding the possibility of having such kind of yield limit, we went on trying to find a flow rule able to capture the localization of deformations, characteristic of the structures. To do so, we had two possibilities: either going on with the expensive numerical approach, or exploring the analytical one.
Observing the outputs of the FE simulations we noticed that all the deformations during every type of test, localized in the joint of the bars. This observation gave us a reason to model the plastic behaviour through the use of plastic hinges. Therefore, on a 2D, small strains framework, we faced the homogenization of the elastic-plastic problem of a "Y" shaped RVE, made of a simple von Mises material on the smallest scale and, of a system of extensible bars connected by rotational springs on the meso-scale. For the former case we performed numerical homogenization, in order to find the yield surface of the homogenized structure, building a numerical laboratory with the software ABAQUS. For the latter, we used average field theory to find a closed relation between $\overline{\mathbf{T}}$ and $\overline{\mathbf{H}}$ for the elastic problem. We assumed that the yielding of the structure is due to an excessive variation of the angle between the bars and not to their elongation or bending. Based on this new assumption, we have developed an algorithm which considers the total angle difference between two bars as the sum of its elastic and plastic parts $\Delta\varphi = \Delta\varphi_e + \Delta\varphi_p$.

This algorithm, although simple, allows us to observe different things: the final configuration of the bars (Figure 8.11); the yield surface in the stress space (Figure 10.1); the evolution of the yield limit (Figures 10.3, 10.4 and 10.5); the direction of the plastic flow and the compressible plasticity (Figure 10.6). Moreover, once computed the effective material parameters and implemented the algorithm as an ABAQUS user material, we could run simulations and see the behaviour of an homogeneous continuum responding to the described material law, in particular we saw the localization of the strains in shear bands paths (Figures 10.10 and 10.11). The real power of this model stands behind its simplicity: observing the behaviour of the internal structure, one can extract the elements that mainly contribute to the effective one, which are the elongation contribution, rather than the bending one, to the deformations, and the fact that the plastic deformations concentrate only at the bar joints, where plastic hinges form. It is clear that the more we enrich the model, the better we can capture the effective plastic behaviour and that this work is just a starting point for further investigations on the topic. Nevertheless, the results obtained with this approach are really encouraging, thanks to the simplicity and interpretability of the methods employed, and we really hope that it will be used and deepened in the future.

11.2 Outlook

In the spirit of encouraging new researchers to use and enrich our model, here we give some inputs and ideas that arose in our minds while working on this thesis. In particular, as an outlook for next works, a few things would be interesting to investigate.

- A study of the evolution of the yield surface with the initial FE approach could be a challenging task for a numerical analyst, which could reformulate the parametrization and run cyclic loads on the structure;
- Extend the model proposed in chapter 8 considering the bending of the bars and including the bending moment. Notice that this is not a trivial extension: the main problem of considering moments on the meso-scale arises when we have to go to the macro-scale. First of all: what would be the respective effective quantity? For the forces we have the Cauchy stress tensor and the conjugate strains. For the moments, this would be a couple stress tensor. If one considers the angle variation on the meso-scale as conjugate to the moments, anyway the question of how to translate it on the macro scale comes natural. The micropolar theory comes to mind, but it is not clear what effective quantity belongs to the angle variations of the beams. In any case, this step would just influence the elastic properties of the structure;
- As a natural consequence of the previous point, the final element implementation of the more complex model comes to mind: this would be a serious issue, because one should develop itself the code for the gradient or micropolar theory, since conventional tools would be useless[1];

[1] Conventional FE methods provide only C^0 continuity of the displacement field, while gradient models require C^1 continuity, since they consider also the second derivative of $\mathbf{u}$. There are no standard 3D finite elements that address this issue. One has resort to somewhat non-standard methods, like the isogeometric analysis or a weak enforcement of the strain gradient in standard finite elements (usually called implicit gradient extension, see, e.g. Dimitrijevic and Hackl [2008].

- Extend the model proposed in chapter 8 considering large deformations: this would be a very challenging task since the linearity of all our equations would be lost and the system would get complex trigonometrical relations between the terms. In this case the plastic angle variations will be influenced and the localization of plastic deformation can become more visible in the finite element simulations;
- Interpret and find an analytical expression for the flow rule;
- Approach the problem directly with plastic gradient theories.

In the context of plastic in-plane models for regular hexagonal honeycomb structures, these are the open questions that arose during our work and still need to be answered.

Appendix A

Python algorithm with stress tensor parametrization

In the following, we report the phython script used to run the simulations as described in chapter 5.

```
# List of tools necessary to run ABAQUS and Python

from abaqus import *
from abaqusConstants import *
from odbAccess import *
from math import *
import __main__
import sys
import string
import fileinput
import shutil
import os
import subprocess
import time
import section
import regionToolset
import displayGroupMdbToolset as dgm
import part
import material
import assembly
import step
import interaction
import load
import mesh
import optimization
import job
import sketch
import visualization
import xyPlot
import displayGroupOdbToolset as dgo
import connectorBehavior
import odbAccess
import random
import math

# Open and operate on the ABAQUS input file

# Looping the angle $\chi$

for j in range(0,360,5):
    kappa=j/180.0*3.1415926
    sigma1=sin(kappa)
    sigma2=cos(kappa)
```

```
    currange=range(21)

# Looping the angle $\phi$
    for i in currange:

        phi=(1.5*i)/180.0*3.1415926
        shutil.copyfile('symyield.inp', 'symyield-current.inp')

        c=cos(phi)
        s=sin(phi)

        f = open('symyield-current.inp','a')

# Setting plane strains on the artificial nodes an1, an2, an3

        f.write('*Boundary\n')
        f.write('fixed, 1, 3, 0.0\n')
        f.write('an1,3,3,0.0\n')
        f.write('an2,3,3,0.0\n')
        f.write('an3,1,1,0.0\n')
        f.write('an3,2,2,0.0\n')
        f.write('an3,3,3,0.0\n')

# Setting stresses through the parametrization on the artificial nodes

        f.write('*CLOAD\n')
        f.write('an1,1,%s\n' %(str(10.0*sigma1*c*c+10.0*sigma2*s*s)))
        f.write('an1,2,%s\n' %(str(10.0*c*s*(sigma1-sigma2))))
        f.write('an2,1,%s\n' %(str(10.0*c*s*(sigma1-sigma2))))
        f.write('an2,2,%s\n' %(str(10.0*s*s*sigma1+10.0*sigma2*c*c)))
        f.write('**                                          \n')
        f.write('** OUTPUT REQUESTS                          \n')
        f.write('**                                          \n')
        f.write('*Restart, write, frequency=0                \n')
        f.write('**                                          \n')
        f.write('** FIELD OUTPUT: F-Output-1                 \n')
        f.write('**                                          \n')
        f.write('*Output, field, variable=PRESELECT, frequency=1 \n')
        f.write('**                                          \n')
        f.write('** HISTORY OUTPUT: H-Output-1               \n')
        f.write('**                                          \n')
        f.write('*Output, history, variable=PRESELECT        \n')
        f.write('*End Step                                   \n')

        f.close()

# Run job

        job = '~/ABQ/Commands/abaqus job=symyield-current ask_delete=OFF  cpus=8'
        os.system(job)

# Wait for job to finish

        t0 = time.time();
        while not os.path.isfile("symyield-current.lck"):
            time.sleep(2.)
            tn = time.time();
            print 'Job starts ..., t = ',tn-t0
        while os.path.isfile("symyield-current.lck"):
            time.sleep(2.)
            tn = time.time();
            print 'Job runs ..., t = ',tn-t0

# Writing the report

        inpname='symyield-current'
        o1 = session.openOdb(name=inpname+'.odb')
        session.viewports['Viewport: 1'].setValues(displayedObject=o1)
        odb = session.odbs[inpname+'.odb']
        framelen=len(odb.steps['Step-1'].frames)
        nodes=odb.rootAssembly.nodeSets[' ALL NODES']
```

```
        session.xyDataListFromField(odb=odb, outputPosition=NODAL, variable=(('RF',
            NODAL, ((COMPONENT, 'RF1'), (COMPONENT, 'RF2'), (COMPONENT, 'RF3'), )),
            ), nodeSets=('AN1', 'AN2', 'AN3', ))
        session.xyDataListFromField(odb=odb, outputPosition=NODAL, variable=(('U',
            NODAL, ((COMPONENT, 'U1'), (COMPONENT, 'U2'), (COMPONENT, 'U3'), )), ),
            nodeSets=('AN1', 'AN2', 'AN3', ))

        K1NR = 6458
        K2NR = K1NR+1
        K3NR = K1NR+2

# Write the displacements

        x0 = session.xyDataObjects['U:U1 PI: PART-1-1 N: %d' %K1NR]
        x1 = session.xyDataObjects['U:U2 PI: PART-1-1 N: %d' %K1NR]
        x2 = session.xyDataObjects['U:U3 PI: PART-1-1 N: %d' %K1NR]
        x3 = session.xyDataObjects['U:U1 PI: PART-1-1 N: %d' %K2NR]
        x4 = session.xyDataObjects['U:U2 PI: PART-1-1 N: %d' %K2NR]
        x5 = session.xyDataObjects['U:U3 PI: PART-1-1 N: %d' %K2NR]
        x6 = session.xyDataObjects['U:U1 PI: PART-1-1 N: %d' %K3NR]
        x7 = session.xyDataObjects['U:U2 PI: PART-1-1 N: %d' %K3NR]
        x8 = session.xyDataObjects['U:U3 PI: PART-1-1 N: %d' %K3NR]

# Write the reaction forces

        x9 = session.xyDataObjects['RF:RF1 PI: PART-1-1 N: %d' %K1NR]
        x10 = session.xyDataObjects['RF:RF2 PI: PART-1-1 N: %d' %K1NR]
        x11 = session.xyDataObjects['RF:RF3 PI: PART-1-1 N: %d' %K1NR]
        x12 = session.xyDataObjects['RF:RF1 PI: PART-1-1 N: %d' %K2NR]
        x13 = session.xyDataObjects['RF:RF2 PI: PART-1-1 N: %d' %K2NR]
        x14 = session.xyDataObjects['RF:RF3 PI: PART-1-1 N: %d' %K2NR]
        x15 = session.xyDataObjects['RF:RF1 PI: PART-1-1 N: %d' %K3NR]
        x16 = session.xyDataObjects['RF:RF2 PI: PART-1-1 N: %d' %K3NR]
        x17 = session.xyDataObjects['RF:RF3 PI: PART-1-1 N: %d' %K3NR]

        session.writeXYReport(fileName=inpname+'_U'+'.rpt', appendMode=OFF, xyData=(x0, x1,
            x2, x3, x4, x5, x6, x7, x8, x9, x10, x11, x12, x13, x14, x15, x16, x17))

# Write Green's strain tensor

        textfile = open(inpname+str(j)+'_'+str(i)+'.txt','w')
        #~ textfile.write("NINC     TIME     STRESS     NORM E     NORM EDEV\n")
        for i in range(len(x0.data)):
            e1=x0.data[i][1]
            e2=x4.data[i][1]
            e3=x8.data[i][1]
            e4=(x1.data[i][1]+x3.data[i][1])/2.0
            e5=(x2.data[i][1]+x6.data[i][1])/2.0
            e6=(x5.data[i][1]+x7.data[i][1])/2.0
            norme=sqrt(e1**2+e2**2+e3**2+2.0*e4**2+2.0*e5**2+2.0*e6**2)
            tracee3=(e1+e2+e3)/3.0
            e1d=e1-tracee3
            e2d=e2-tracee3
            e3d=e3-tracee3
            normed=sqrt(e1d**2+e2d**2+e3d**2+2.0*e4**2+2.0*e5**2+2.0*e6**2)

# Save the resulting values

            textfile.write(str(i)+"    "+str(x0.data[i][0])+"     "+str(norme)+"     "+str(normed)+
        textfile.close()

# Delete the current session and close the odb file

        del session.xyDataObjects['U:U1 PI: PART-1-1 N: %d' %K1NR]
        del session.xyDataObjects['U:U2 PI: PART-1-1 N: %d' %K1NR]
        del session.xyDataObjects['U:U3 PI: PART-1-1 N: %d' %K1NR]
        del session.xyDataObjects['U:U1 PI: PART-1-1 N: %d' %K2NR]
        del session.xyDataObjects['U:U2 PI: PART-1-1 N: %d' %K2NR]
        del session.xyDataObjects['U:U3 PI: PART-1-1 N: %d' %K2NR]
        del session.xyDataObjects['U:U1 PI: PART-1-1 N: %d' %K3NR]
        del session.xyDataObjects['U:U2 PI: PART-1-1 N: %d' %K3NR]
```

```
del session.xyDataObjects['U:U3 PI: PART-1-1 N: %d' %K3NR]

del session.xyDataObjects['RF:RF1 PI: PART-1-1 N: %d' %K1NR]
del session.xyDataObjects['RF:RF2 PI: PART-1-1 N: %d' %K1NR]
del session.xyDataObjects['RF:RF3 PI: PART-1-1 N: %d' %K1NR]
del session.xyDataObjects['RF:RF1 PI: PART-1-1 N: %d' %K2NR]
del session.xyDataObjects['RF:RF2 PI: PART-1-1 N: %d' %K2NR]
del session.xyDataObjects['RF:RF3 PI: PART-1-1 N: %d' %K2NR]
del session.xyDataObjects['RF:RF1 PI: PART-1-1 N: %d' %K3NR]
del session.xyDataObjects['RF:RF2 PI: PART-1-1 N: %d' %K3NR]
del session.xyDataObjects['RF:RF3 PI: PART-1-1 N: %d' %K3NR]

odb.close()
```

Appendix B

UMAT implementation of the non-convex yield surface

The UMAT file for the implementation of the procedure described in chapter 6 is reported in the following. Notice that it contains all the parts of the analysis, namely the von Mises and the proposed yield criteria, the associative and non-associative flow rule, and the isotropic and distortional hardening. To use the desired subroutine, the user has just to comment the others.

```
c~~~~ Initialisation internal variables

      subroutine sdvini(statev,coords,nstatv,ncrds,noel,npt,layer,kspt)
      implicit none
      integer nstatv,ncrds,kspt,layer,npt,noel
      double precision statev(nstatv),coords(ncrds)

      statev=0.d0
      return
      end

      subroutine umat(stress,statev,ddsdde,sse,spd,scd,
     1 rpl,ddsddt,drplde,drpldt,
     2 stran,dstran,time,dtime,temp,dtemp,predef,dpred,cmname,
     3 ndi,nshr,ntens,nstatv,props,nprops,coords,drot,pnewdt,
     4 celent,dfgrd0,dfgrd1,noel,npt,layer,kspt,kstep,kinc)

c~~~~ Declarations abaqus

      implicit none
      integer kstep,kspt,layer,npt,noel,nprops,nstatv,ntens,
     1 nshr,ndi,kinc,maxit
      double precision sse,spd,scd,rpl,drpldt,dtime,temp,dtemp,
     1 pnewdt,celent
      double precision dfgrd0(3,3),dfgrd1(3,3),time(2),stress(ntens),
     1 statev(nstatv),ddsdde(ntens,ntens),ddsddt(ntens),drplde(ntens),
     2 stran(ntens),dstran(ntens),predef(1),dpred(1),props(nprops),
     3 coords(3),drot(3,3)
      character*80 cmname

c~~~~ Declarations user

      integer i
      double precision CMAT(3,3) , EMO,nu
      double precision stranelpred(3),ys,stranplsave(3),stranplneu(3)
      double precision stranneu(3),delta,stressneu(3),lambda,rdummy
      double precision rd2,epeq,epsplast(3)

      delta=1.d-7
```

```
c~~~~ Predictor step, call for hooke's law

      stranneu=stran+dstran
      epsplast(1:3)=statev(1:3)
      stranelpred=stranneu-epsplast
      lambda=statev(4)
      epeq=statev(5)
      rdummy=lambda
      rd2=epeq
      call hooke(stress,stranelpred,CMAT)

c~~~~  Corrector step

      if (YS(stress,epeq,epsplast).gt.0.d0) then

c~~~~ Gets the updates
c~~~~ Saves the output state as the new starting point and
c~~~~ updates stranplneu and stress

        stranplsave=epsplast
        stranplneu=stranplsave
        call update(stranneu,stranplneu,stress,lambda,pnewdt,dtime,epeq)
        statev(1:3)=stranplneu
        statev(4)=lambda
        statev(5)=epeq

c~~~~  Gets the difference quotient

        do i=1,3
          stranplneu=stranplsave
          lambda=rdummy
          epeq=rd2
          stranneu(i)=stranneu(i)+delta
          call update(stranneu,stranplneu,stressneu,lambda,pnewdt,dtime
     &                ,epeq)
          stranneu(i)=stranneu(i)-delta
          ddsdde(i,:)=(stressneu(:)-stress(:))/delta
        end do
      else
        ddsdde=CMAT
      end if

c~~~~  Regularising viscosity:
c~~~~  large values for rdummy will heavily distort the results,
c~~~~  it should be kept small at cost of small stepsize

      rdummy=0.1d0

      stress(1:3)=stress(1:3)+rdummy/dtime*dstran(1:3)
      do i=1,3
        ddsdde(i,i)=ddsdde(i,i)+rdummy/dtime
      end do
      return
      end

c~~~~ Hooke's law

      subroutine hooke(stress,strain,C)
      implicit none
      double precision stress(3),strain(3),C(3,3),rdummy,EMO,nu
      EMO=20.d1
      nu=0.3d0

      rdummy=EMO/(1.d0-nu*nu)

      C=0.d0
      C(1,1)=rdummy
      C(1,2)=nu*rdummy
      C(2,1)=nu*rdummy
      C(2,2)=rdummy
```

```
      C(3,3)=0.5d0*(1.d0-nu**2)*rdummy

      stress=matmul(C,strain)

      return
      end

      subroutine update(stranneu,stranplneu,stress,lambda,pnewdt,dtime,
     &                  epeq)
      implicit none
      double precision stranneu(3),stranplneu(3),stress(3)
      double precision lambda,stranelneu(3),dtime

      double precision x(4),passin(8),tol,damp(4),pnewdt
      integer size,npassin,maxit,msglinesearch,msgjac,msgquasi

      double precision CMAT(3,3),EMO,nu,rdummy,YS,epeq

      external resmaterial

c~~~~ Isotropic plane stress stiffness

      size=4
      npassin=8
      tol=1.d-10
      maxit=1000
      damp=1.d0
      msglinesearch=0
      msgjac=1
      msgquasi=-1

      passin(1:3)=stranplneu
      passin(4:6)=stranneu
      passin(7)=dtime
      passin(8)=epeq
      x(1:3)=stranplneu
      x(4)=lambda

      call solven(x,resmaterial,size,passin,
     &   npassin,tol,maxit,damp,msglinesearch,msgjac,
     &   msgquasi)

      stranplneu(1:3)=x(1:3)
      lambda=x(4)
      epeq=epeq+x(4)*passin(7)
      stranelneu=stranneu-stranplneu
      call hooke(stress,stranelneu,CMAT)
      if(maxit.eq.0)then
        pnewdt=0.5d0
      end if
      return
      end

      subroutine resmaterial(x,r,passin,npassin,size)
      implicit none

      integer npassin,size

      double precision epsplastalt(3),epsneu(3)
      double precision epsplastcurrent(3),epselastcurrent(3)
      double precision dys(3),ys,passin(npassin),x(4),stress(3),r(4)

      double precision CMAT(3,3),EMO,nu,rdummy,epeqneu
      double precision I(3),dil(3),dev(3),s1,s2,ratio

      epsplastalt(1:3)=passin(1:3)
      epsneu(1:3)=passin(4:6)
      epsplastcurrent(1:3)=x(1:3)
      epselastcurrent=epsneu-epsplastcurrent
      epeqneu=passin(8)+x(4)*passin(7)
```

```
c~~~~ Defines the new elements

      I(1)=1.d0
      I(2)=1.d0
      I(3)=0.d0

      call hooke(stress,epselastcurrent,CMAT)

c~~~~ Elements for the non-associative flow rule

      dil=0.5d0*(stress(1)+stress(2))*I
      dev=stress-dil
      ratio=10.d0*dexp(-epeqneu) + 1.d0
      s2=1.d0/(ratio+1.d0)
      s1=1.d0/(1.d0/ratio+1.d0)

      call YSwDerivative(stress,epeqneu,dys,ys,epsplastcurrent)

c~~~~ Associative flow rule

      r(1:3) = epsplastalt + x(4) * passin(7) * (dil+dev)
     &         - epsplastcurrent

c~~~~ Non-associative flow rule

      r(1:3)=epsplastalt+x(4) * passin(7)*(s1*dev(1:3) + s2*dil(1:3))
     &         - epsplastcurrent
      r(4)=ys
      return
      end

c~~~~ HONEYCOMBS' YIELD SURFACE

c~~~~ Define the eigenvalues of the stress tensor

      FUNCTION l1(s)
      implicit none
      double precision s(3), l1

      l1=1/2.d0*(s(1)+s(2)-dsqrt(s(1)**2+4.d0*s(3)**2-2*s(1)*s(2)
     &   +s(2)**2))

      return
      end

      FUNCTION l2(s)
      implicit none
      double precision s(3), l2

      l2=1/2.d0*(s(1)+s(2)+dsqrt(s(1)**2+4*s(3)**2-2*s(1)*s(2)+s(2)**2))

      return
      end

c~~~~ Defines the parametrization

      function chi(s)
      implicit none
      double precision chi,l1,l2,s(3)
      chi=datan2(l2(s),l1(s))
      return
      end

      function phi(s)
      implicit none
      double precision phi,s(3)

      If(s(3).eq.0) then
      phi=0.d0
      else
      phi=datan2(2.d0*s(3),(s(1)+dsqrt(4.d0*(s(3)**2)+(s(1)-s(2))**2)
```

```
     &     -s(2)))
      end if

      return
      end

      function mag(s)
      implicit none
      double precision mag, s(3)

      mag=dsqrt(s(1)**2+s(2)**2+2.d0*s(3)**2)

      return
      end

c~~~~ Defines the function b

      function b(chi)
      implicit none
      double precision chi, pi8, b
      pi8=dacos(-1.0d0)

      if((chi.gt.0.d0) .and. (chi.lt.pi8/2.d0)) then
      b=-0.232135*dsin(5.18173*(-pi8/4.d0+chi))
     &   -0.100778*dsin(10.2899*(-pi8/4.d0+chi))
      else if ((chi.gt.pi8/2.d0) .and. (chi.lt.pi8)) then
      b=-0.146533*dsin(pi8/4.d0-chi)
     &   -0.0231437*dsin(2.d0*(-pi8/4.d0+chi))
      else if (chi.lt.0.d0) then
      b=-0.146533*dsin(pi8/4.d0-chi)
     &   -0.0231437*dsin(2.d0*(-pi8/4.d0+chi))
      end if

      return
      end

c~~~~ Defines the function a

      function a(chi)
      implicit none
      double precision chi, pi8, a

      pi8=dacos(-1.0d0)


      a=0.0862606
     &   +7.1091*10.d0**(-6.d0)*dexp(13.0758*dcos(pi8/4.d0-chi))
     &   +0.2d0*dexp(2.d0*dcos(pi8/8.d0-chi/2.d0)**2)
     &   +3.75384*dexp(-15002.3d0*dcos(pi8/8.d0-chi/2.d0)**2)

      RETURN
      END FUNCTION

c~~~~ Defines the bell function for the distortional hardening

      function bell(chi)
      implicit none
      double precision chi, pi8, bell

      pi8=dacos(-1.0d0)


      bell=dexp(-(chi-pi8)**2/(2*pi8/36))
     &     +dexp(-(chi-3/2*pi8)**2/(2*pi8/36))

      RETURN
      END FUNCTION

c~~~~ T.eps trace(T.eps)/modT (orientation of the load)

      function teps(s,epsplastcurrent)
```

```
      implicit none
      double precision  teps, epsplastcurrent(3), s(3), n

      n=dsqrt(s(1)**2+s(2)**2+2*s(3)**2)

      if(n.lt.1.d-6) then

      teps=0.d0

      else

      teps=(s(1)*epsplastcurrent(1)+s(2)*epsplastcurrent(2)
     &     +2.d0*s(3)*epsplastcurrent(3))/n

      end if

      RETURN
      END FUNCTION

c~~~~ Defines the tuning function for the distortional hardening

      function fs(teps)
      implicit none
      double precision  fs, teps


      If(teps.lt.0) then
      fs=0.d0
      else
      fs=(teps-0.4d0)**4-0.4d0**4
      end if

      RETURN
      END FUNCTION

c~~~~ Defines the term to add to the the yield function

      function c(s,epsplastcurrent)
      implicit none
      double precision  fs, bell, s(3), epsplastcurrent(3), c, teps, chi
      double precision tepsval
      tepsval=teps(s,epsplastcurrent)
      c=1.d0*fs(tepsval)*bell(chi(s))

      RETURN
      END FUNCTION

c~~~~ Defines the function describing the yield stress surface of the material

      function approach(s,epsplastcurrent)
      implicit none
      double precision a, b, approach, phi, s(3),chi, epsplastcurrent(3)
      double precision pi8, c, teps, fsy, bell

c~~~~ Greek pi

      pi8=dacos(-1.0d0)

c~~~~ Yield surface with distortional hardening

      approach=a(chi(s))+b(chi(s))*dcos(6.d0*phi(s))
     &         +c(s,epsplastcurrent)
      RETURN
      END FUNCTION

c~~~~ The material is in the elastic range when ys<0

       FUNCTION ys(s,epeq,epsplastcurrent)
       implicit none
       double precision mag, approach, ys, s(3), epeq
       double precision epsplastcurrent(3)
```

```
c~~~~ Yield criterion with isotropic hardening

        ys=mag(s)
      &    -((epeq - 0.3d0)**2+1.d0-0.3d0**2)*approach(s,epsplastcurrent)

        RETURN
        END FUNCTION

c~~~~ VON-MISES YIELD CRITERION

        FUNCTION YS(stressvek,epeq)
        implicit none
        double precision stressvek(3),YS,press,epeq
        press=0.5d0*(stressvek(1)+stressvek(2))
        YS=dsqrt((stressvek(1)-press)**2+
       &    (stressvek(2)-press)**2+
       &    2.0*stressvek(3)**2)-100.d0*(1.d0+5.d0*epeq)
        RETURN
        END FUNCTION

       SUBROUTINE YSwDerivative(stressvek,epeq,DYS,YSval,epsplastcurrent)
       implicit none
       double precision stressvek(3),DYS(3),YS,YSval,delta,rdummy,epeq
       double precision epsplastcurrent(3)
       integer i

       delta=1.d-3
       YSval=YS(stressvek,epeq,epsplastcurrent)

       do i=1,3
         stressvek(i)=stressvek(i)+delta
         rdummy=YS(stressvek,epeq,epsplastcurrent)
         DYS(i)=(rdummy-YSval)/delta
         stressvek(i)=stressvek(i)-delta
       end do

       RETURN
       END
```

Appendix C

Solution to the problem in chapters 8 and 10

In the following we report the solution for the forces and displacement components of the problems described in the previous chapters. We recall that:

c_{elo} is elastic modulus responsible for the elongation of the bars

c_{rot} is the elastic modulus of the angular spring between the bars

l is the length of the bars.

$$
\begin{aligned}
F_{11} &= \frac{c_{elo}(3c_{elo}(H_{11}+H_{22})+c_{rot}(9H_{11}+2\sqrt{3}H_{12}+2\sqrt{3}H_{21}-3H_{22}-6\Delta\varphi_{12p}l+6\Delta\varphi_{23p}l))}{18(c_{rot}+c_{elo})l}\\
F_{12} &= \frac{c_{elo}(\sqrt{3}c_{elo}(H_{11}+H_{22})+c_{rot}(-\sqrt{3}H_{11}+6H_{12}+6H_{21}+3\sqrt{3}(H_{22}+2(\Delta\varphi_{12p}+\Delta\varphi_{23p})l)))}{18(c_{rot}+c_{elo})l}\\
F_{21} &= \frac{c_{elo}(-3c_{elo}(H_{11}+H_{22})+c_{rot}(-9H_{11}+2\sqrt{3}H_{12}+2\sqrt{3}H_{21}+3H_{22}+12\Delta\varphi_{12p}l+6\Delta\varphi_{23p}l))}{18(c_{rot}+c_{elo})l}\\
F_{22} &= \frac{c_{elo}(\sqrt{3}c_{elo}(H_{11}+H_{22})-c_{rot}(\sqrt{3}H_{11}+6H_{12}+6H_{21}-3\sqrt{3}(H_{22}-2\Delta\varphi_{23p}l)))}{18(c_{rot}+c_{elo})l}\\
F_{31} &= \frac{-(c_{rot}c_{elo}(2\sqrt{3}H_{12}+2\sqrt{3}H_{21}+3(\Delta\varphi_{12p}+2\Delta\varphi_{23p})l)}{9(c_{rot}+c_{elo})l)}\\
F_{32} &= \frac{-(c_{elo}(c_{elo}(H_{11}+H_{22})+c_{rot}(-H_{11}+3(H_{22}+\Delta\varphi_{12p}l)))}{3\sqrt{3}(c_{rot}+c_{elo})l)}
\end{aligned}
\tag{C.1}
$$

$$
\begin{aligned}
u_{11} &= \frac{c_{elo}(H_{11} - H_{21}/\sqrt{3}) + c_{rot}(H_{11} + (2H_{12})/\sqrt{3} + H_{21}/\sqrt{3} + \Delta\varphi_{12p}l + 2\Delta\varphi_{23p}l)}{3(c_{rot} + c_{elo})l} \\
u_{12} &= \frac{\sqrt{3}c_{rot}H_{11} - \sqrt{3}c_{elo}H_{11} + 3c_{rot}H_{21} + 3c_{elo}H_{21} + 2\sqrt{3}c_{elo}H_{22} - 3\sqrt{3}c_{rot}\Delta\varphi_{12p}l}{9c_{rot}l + 9c_{elo}l} \\
u_{21} &= \frac{-3(c_{rot} + c_{elo})H_{11} + 2\sqrt{3}c_{rot}H_{12} + \sqrt{3}c_{rot}H_{21} - \sqrt{3}c_{elo}H_{21} + 3c_{rot}\Delta\varphi_{12p}l + 6c_{rot}\Delta\varphi_{23p}l}{9(c_{rot} + c_{elo})l} \\
u_{22} &= \frac{\sqrt{3}c_{rot}H_{11} - \sqrt{3}c_{elo}H_{11} - 3c_{rot}H_{21} - 3c_{elo}H_{21} + 2\sqrt{3}c_{elo}H_{22} - 3\sqrt{3}c_{rot}\Delta\varphi_{12p}l}{9c_{rot}l + 9c_{elo}l} \\
u_{31} &= \frac{-\sqrt{3}c_{elo}(3H_{12} + H_{21}) + c_{rot}(-\sqrt{3}H_{12} + \sqrt{3}\sqrt{3}H_{21} + 3\Delta\varphi_{12p}l + 6\Delta\varphi_{23p}l)}{9(c_{rot} + c_{elo})l} \\
u_{32} &= \frac{-c_{elo}(H_{11} + H_{22}) + c_{rot}(H_{11} - 3(H_{22} + \Delta\varphi_{12p}l))}{3\sqrt{3}(c_{rot} + c_{elo})l}
\end{aligned}
\tag{C.2}
$$

Notice that, since we are in the small strain setting $H_{12} = H_{21}$.

Appendix D

Mathematica script for the plastic flow direction

The process to find the plastic flow direction is divided in three parts which we report below.

Part 1

Write the average displacement gradient, $\overline{\mathbf{H}}$, in function of the angle variations:

```
Remove["Global`*"]

(*Bars length*)

l = 1;

(*Bars position*)

x01 = {Sqrt[3]/2 l , l/2};
x02 = {-Sqrt[3]/2 l , l/2};
x03 = {0, -l};

(*Bars displacement.*)

(*Neglect elongation setting \
u12=-ArcTan[3,Pi]u11 and u22=-ArcTan[3,Pi]u21*)

u1 = {u11, -u11/ArcTan[Pi/3]};
u2 = {u21, u21/ArcTan[Pi/3]};
u3 = {u31, 0};

(*Tangent and normal vectors to the displacement*)

t01 = {-1/2, Sqrt[3]/2};
t02 = {-1/2, -Sqrt[3]/2};
t03 = {1, 0};
n01 = {l + l/2 , Sqrt[3]/2 l};
n02 = {-l - l/2 , Sqrt[3]/2 l};
n03 = {0, -l 2 Sqrt[3]/2};

(*Average displacement gradient*)

HBAR = (Outer[Times, u1, n01] + Outer[Times, u2, n02] +
    Outer[Times, u3, n03]);
```

```
(*Angles variations*)

eq1 = deltaphi12 == -(u1.t01 - u2.t02);
eq2 = deltaphi23 == -(u2.t02 - u3.t03);
eq3 = deltaphi31 == -(u3.t03 - u1.t01);

(*This equation is not useful because it is linearly \
dependent from the previous two*)

(*Solve equations 1 and 2 for the \
two displacements*)

expr = Solve[{eq1, eq2}, {u11, u21}];

(*Substitute the obtained expressoions for u11 and u22 in the average \
displacement gradient*)

HBAR = FullSimplify[(HBAR /. expr)[[1]]];

(* Determine u31 such that HBAR is symmetric*)

expr = Solve[HBAR[[1, 2]] == HBAR[[2, 1]], u31];

(*Substitute the obtained expressoions for u31 in the average \
displacement gradient*)

HBAR = FullSimplify[HBAR /. expr[[1, 1]]]
```

Part 2

Write the angle variations as a function of the stress tensor components:

```
Remove["Global`*"]

(*Elastic constant of the rotational springs*)

c = 3;
u1 = {u11, u12};
u2 = {u21, u22};
u3 = {u31, u32};
x01 = {Sqrt[3]/2 l , l/2};
x02 = {-Sqrt[3]/2 l , l/2};
x03 = {0, -l};
n01 = {l + l/2 , Sqrt[3]/2 l};
n02 = {-l - l/2 , Sqrt[3]/2 l};
n03 = {0, -l 2 Sqrt[3]/2};
t01 = {-1/2, Sqrt[3]/2};
t02 = {-1/2, -Sqrt[3]/2};
t03 = {1, 0};

(*Forces vectors for each bar*)

F1 = {F11, F12};
F2 = {F21, F22};
F3 = {F31, F32};

(*Stress tensor*)

STRESSES = {{T11, T12}, {T12, T22}};

(*Average stress*)

eqs0 = Flatten[
   Table[STRESSES[[i,
       j]] == (Outer[Times, F1, x01] + Outer[Times, F2, x02] +
        Outer[Times, F3, x03])[[i, j]], {i, 1, 2}, {j, 1, 2}]];

(*Forces equilibrium*)
```

```
eqs1 = Flatten[Table[F1[[i]] + F2[[i]] + F3[[i]] == 0, {i, 1, 2}]];

(*Moment equilibrium*)

eqs2 = {F1.t01 + F2.t02 + F3.t03 == 0};

(*Constitutive equations for the elastic elongations of the bars*)

eqs3 = {EM0 u1.x01 == F1.x01, EM0 u2.x02 == F2.x02,
   EM0 u3.x03 == F3.x03};

(*Compute thte angles variations between the bars*)

deltaphi12 = -(u1.t01 - u2.t02);
deltaphi23 = -(u2.t02 - u3.t03);
deltaphi31 = -(u3.t03 - u1.t01);

(*Calculate the elastic part of the angles variations*)

deltaphi12e = (deltaphi12 - deltaphi12p);
deltaphi23e = (deltaphi23 - deltaphi23p);
deltaphi31e = (deltaphi31 - deltaphi31p);

(*Constitutive equations for the elastic-plastic hinges*)

(*This will \
be used to find the elastic part of the average displacement gradient*)

eqs4 = {
   -c deltaphi12e == F1.t01 - F2.t02,
   -c deltaphi23e == F2.t02 - F3.t03,
   -c deltaphi31e == F3.t03 - F1.t01};

(*Solve equations 0, 1, 2 for the forces*)

eqs = Join[eqs0, eqs1, eqs2] ;
erg = Solve[eqs, {F11, F12, F21, F22, F31, F32}];
Set @@@ erg[[1]];

(*Substitute the expretions found for the forces in the definition of \
the elastic angle variations*)

deltaphi12e =
 FullSimplify[(F1.t01 - F2.t02)/c]
deltaphi23e = FullSimplify[(F2.t02 - F3.t03)/c]
deltaphi31e = FullSimplify[(F3.t03 - F1.t01)/c]
```

Part 3

Find the plastic increment and plot it in the stress space:

```
Remove["Global`*"]
l = 1;
c = 3;

(*Define the function that gives the plastic angle variation for a \
given elastic angle variation*)

update[arg_] := (

   (*a is the list of elastic deltaangles*)

   a = arg;
   yield = 0.2;
   err = 0.00000000;

   (*Plastic corrector step*)
```

```
   ind = {0, 0, 0};
   For[i = 1, i <= 3, i++,
    If[Abs[a[[i]]] > yield, ind[[i]] = 1]
    ];
   sum = Sum[ind[[i]], {i, 1, 3}];

   (*If sum=0 the deformation is purely elastic*)

   (*Case 1:
   only one angle exceeds the yield limit*)

   If[sum == 1,
    While[Max[Abs[a]] > yield,
      which = Position[ind, 1][[1, 1]];
      If[a[[which]] > yield, res = a[[which]] - yield];
      If[a[[which]] < -yield, res = a[[which]] + yield];

      For[i = 1, i <= Length[a], i++,
       If[a[[i]] > yield,
        a[[i]] = yield;
        ];
       If[a[[i]] < -yield,
        a[[i]] = -yield;
        ];
       If[
        a[[i]] > -yield && a[[i]] < -err ||
         a[[i]] > err && a[[i]] < yield,
        a[[i]] = a[[i]] + res/2;
        ];
       ];
      ];
    ];

   (*Case 2: two angles exceed the yield limit*)

   If[sum == 2,
    For[i = 1, i <= 3, i++,
      If[a[[i]] > yield, a[[i]] = yield,
       If[a[[i]] < -yield, a[[i]] = -yield,
        a[[i]] = 0]]];
    ];

   (*Case 3:

   three angle exceed the yield limit*)

   (*Notice that this case is \
in reality excluded from the possibilies because it would mean a too \
big predictor step*)

   (*It is here only for representation scopes*)

      If[sum == 3,
    a = {0, 0, 0};
    ];
   a);

(*Compute the elastic angle variation*)

showyield[T_] := (
   T11 = T[[1]];
   T22 = T[[2]];
   T12 = T[[3]];
   oldel = {(-T11 + T22)/(Sqrt[3] c l), (
     Sqrt[3] T11 + 6 T12 - Sqrt[3] T22)/(6 c l), (
     Sqrt[3] T11 - 6 T12 - Sqrt[3] T22)/(6 c l)};
   newel = update[oldel];
   If[Norm[newel - oldel] == 0, -1, Norm[newel - oldel]]
   );
```

```
(*Compute the plastic angle variation and the flow direction*)

arrow[T_] := (
  T11 = T[[1]];
  T22 = T[[2]];
  T12 = T[[3]];

  oldel = {(-T11 + T22)/(Sqrt[3] c l), (
    Sqrt[3] T11 + 6 T12 - Sqrt[3] T22)/(6 c l), (
    Sqrt[3] T11 - 6 T12 - Sqrt[3] T22)/(6 c l)};
  newel = update[oldel];
  plastangle = oldel - newel;
  deltaphi12 = plastangle[[1]];
  deltaphi23 = plastangle[[2]];
  deltaphi31 = plastangle[[3]];
  dir = -{(3 deltaphi12 ArcTan[\[Pi]/3])/(
     Sqrt[3] + ArcTan[\[Pi]/3]), -((3 deltaphi12)/(
      3 + Sqrt[3] ArcTan[\[Pi]/3])), -((deltaphi12 + 2 deltaphi23)/(
      Sqrt[3] + ArcTan[\[Pi]/3]))};
  Arrow[{T, T + 0.5 Normalize[dir]}]
  )

(*Plot the yield surface together with the plastic flow direction*)
\

limit = 1.5
Show[RegionPlot3D[
  showyield[{x, y, z}] < 0, {x, -limit, limit}, {y, -limit,
   limit}, {z, -limit, limit}, PlotPoints -> 30],
 Graphics3D[Table[arrow[{i, -i, 0.62 - i/2}], {i, 0, 0.5, 0.1}]],
 Graphics3D[Table[arrow[{-i, i, 0.62 - i/2}], {i, 0, 0.5, 0.1}]],
 Graphics3D[Table[arrow[{0.52, -0.52, 0.31 - i}], {i, 0, 0.6, 0.1}]],
 Graphics3D[Table[arrow[{-0.52, 0.52, 0.31 - i}], {i, 0, 0.6, 0.1}]]]
```

Appendix E

UMAT implementation of the algorithm for plastic hinges

In the following, we report the file with the approach and algorithm described in chapter 8

```
c~~~~ Initialisation internal variables

      subroutine sdvini(statev,coords,nstatv,ncrds,noel,npt,layer,kspt)
      implicit none
      integer nstatv,ncrds,kspt,layer,npt,noel
      double precision statev(nstatv),coords(ncrds)

      statev=0.d0

      return
      end

      subroutine umat(stress,statev,ddsdde,sse,spd,scd,
     1 rpl,ddsddt,drplde,drpldt,
     2 stran,dstran,time,dtime,temp,dtemp,predef,dpred,cmname,
     3 ndi,nshr,ntens,nstatv,props,nprops,coords,drot,pnewdt,
     4 celent,dfgrd0,dfgrd1,noel,npt,layer,kspt,kstep,kinc)

c~~~~ Declarations abaqus

      implicit none
      integer kstep,kspt,layer,npt,noel,nprops,nstatv,ntens,
     1 nshr,ndi,kinc,maxit,i
      double precision sse,spd,scd,rpl,drpldt,dtime,temp,dtemp,
     1 pnewdt,celent
      double precision dfgrd0(3,3),dfgrd1(3,3),time(2),stress(ntens),
     1 statev(nstatv),ddsdde(ntens,ntens),ddsddt(ntens),drplde(ntens),
     2 stran(ntens),dstran(ntens),predef(1),dpred(1),props(nprops),
     3 coords(3),drot(3,3)
      character*80 cmname

      double precision strain(3), delta, intvars(3), intvarsnew(3)
      double precision deltastress(3),visk

c~~~~ Calculate result

      strain=stran+dstran
      intvars=statev(1:3)

      call algorithm(strain, intvars, stress, intvarsnew)

      statev(1:3) = intvarsnew

c~~~~ Calculate tangent
```

```
      delta=0.00001d0
      do i=1,3
        strain(i)=strain(i)+delta
        call algorithm(strain, intvars, deltastress, intvarsnew)
        ddsdde(i,:)=(deltastress(:)-stress(:))/delta
        strain(i)=strain(i)-delta
      end do

c~~~~ Add stabilizing viscosity to value (Stress) and derivative (ddsdde)

      visk=0.1d0
      stress=stress+visk*dstran/dtime
      ddsdde(1,1)=ddsdde(1,1)+visk/dtime
      ddsdde(2,2)=ddsdde(2,2)+visk/dtime
      ddsdde(3,3)=ddsdde(3,3)+visk/dtime
      return
      end

c~~~~ Implementation of the algorithm for the plastic hinges

      subroutine algorithm(strain, deltaphipold, stress, deltaphipnew)
      implicit none
      double precision HBAR(2,2),F1(2),F2(2),F3(2),u1(2),u2(2),u3(2)
      double precision x01(2),x02(2),x03(2),n01(2),n02(2),n03(2)
      double precision t01(2),tx02(2),t03(2),emo,l,c,deltaphiold(3)
      double precision TBAR(2,2), identity(2,2),dfgrd(2,2),deltaphi(3)
      double precision deltaphipnew(3), deltaphie(3),yield, angles(3)
      double precision res,stress(3),strain(3), deltaphipold(3)
      double precision summation, error
      integer i, ind(3)

      identity(1,1)=1
      identity(1,2)=0
      identity(2,1)=0
      identity(2,2)=1

      HBAR(1,1)=strain(1)
      HBAR(1,2)=strain(3)
      HBAR(2,1)=strain(3)
      HBAR(2,2)=strain(2)

      EMO=78.d0
      c=8.d0
      l=1

c~~~~ Computation of forces and angle variations

      F1(1)=(EMO*(3.0*(3.0 + Sqrt(5.0))*EMO*(HBAR(1,1)+HBAR(2,2)) +
     -      c*(9.0*(3.0+Sqrt(5.0))*HBAR(1,1)+2.0*Sqrt(3.0)*(3.0
     -      +Sqrt(5.0))*HBAR(1,2)+
     -      2.0*Sqrt(3.0)*(3.0+Sqrt(5.0))*HBAR(1,2)-
     -      3.0*((3.0+Sqrt(5.0))*HBAR(2,2)+4.0*(deltaphipold(1)
     -      -deltaphipold(2))*l))))/(36.0*(c+EMO)*l)


      F1(2)=(EMO*(Sqrt(3.0)*(3.0+Sqrt(5.0))*EMO*(HBAR(1,1)+HBAR(2,2)) +
     -      c*(-(Sqrt(3.0)*(3.0+Sqrt(5.0))*HBAR(1,1)) +
     -      3.0*(2.0*(3.0+Sqrt(5.0))*HBAR(1,2)+
     -      2.0*(3.0+Sqrt(5.0))*HBAR(1,2)+
     -      Sqrt(3.0)*((3.0+Sqrt(5.0))*HBAR(2,2)+4.0*(deltaphipold(1)
     -      +deltaphipold(2))*l)))))/(36.0*(c + EMO)*l)



      F2(1)=(EMO*(-3.0*(3.0+Sqrt(5.0))*EMO*(HBAR(1,1)+HBAR(2,2)) +
     -      c*(-9.0*(3.0+Sqrt(5.0))*HBAR(1,1)+2.0*Sqrt(3.0)*(3.0+
     -      Sqrt(5.0))*HBAR(1,2)+
     -      2.0*Sqrt(3.0)*(3.0+Sqrt(5.0))*HBAR(1,2)+
     -      3.0*(3.0+Sqrt(5.0))*HBAR(2,2)+
     -      12.0*(2.0*deltaphipold(1)
```

```
     -      +deltaphipold(2))*l)))/(36.0*(c+EMO)*l)

      F2(2)=(EMO*(Sqrt(3.0)*(3.0+Sqrt(5.0))*EMO*(HBAR(1,1)+HBAR(2,2))-
     -      c*(Sqrt(3.0)*(3.0+Sqrt(5.0))*HBAR(1,1)+
     -      3.0*(2.0*(3.0+Sqrt(5.0))*HBAR(1,2)+
     -      2.0*(3.0+Sqrt(5.0))*HBAR(1,2)+
     -      Sqrt(3.0)*((-3.0-Sqrt(5.0))*HBAR(2,2)+
     -      4.0*deltaphipold(2)*l)))))/(36.0*(c + EMO)*l)

      F3(1)=(c*EMO*(4.0*Sqrt(3.0)*HBAR(1,2)+4.0*Sqrt(3.0)*HBAR(1,2)-
     -      3.0*(-3.0+Sqrt(5.0))*(deltaphipold(1)+2.0*deltaphipold(2))
     -      *l))/(9.0*(-3.0+Sqrt(5.0))*(c + EMO)*l)

      F3(2)=(EMO*((3.0+Sqrt(5.0))*c*HBAR(1,1)-(3.0+Sqrt(5.0))
     -      *EMO*(HBAR(1,1)+HBAR(2,2)) -
     -      3.0*c*((3.0+Sqrt(5.0))*HBAR(2,2)+2.0*deltaphipold(1)*l)))/
     -      (6.0*Sqrt(3.0)*(c+EMO)*l)

      deltaphi(1)=(4.0*EMO*(-HBAR(1,1)+HBAR(2,2))+3.0*(-3.0+Sqrt(5.0))
     -            *c*deltaphipold(1)*l)/(3.0*(-3.0+Sqrt(5.0))*(c+EMO)*l)

      deltaphi(2)=(2.0*EMO*(HBAR(1,1)+Sqrt(3.0)*HBAR(1,2)+Sqrt(3.0)
     -            *HBAR(1,2)-HBAR(2,2))+3.0*(-3.0+Sqrt(5.0))*c*
     -            deltaphipold(2)*l)/(3.0*(-3.0+Sqrt(5.0))*(c+EMO)*l)

      deltaphi(3)=(2.0*EMO*HBAR(1,1)-2.0*EMO*(Sqrt(3.0)*HBAR(1,2)
     -            +Sqrt(3.0)*HBAR(1,2)+HBAR(2,2)) -
     -            3.0*(-3.0+Sqrt(5.0))*c*(deltaphipold(1)
     -            +deltaphipold(2))*l)/(3.0*(-3.0+Sqrt(5.0))*(c+EMO)*l)

      deltaphie(1) = (deltaphi(1)- deltaphipold(1))
      deltaphie(2) = (deltaphi(2)- deltaphipold(2))
      deltaphie(3) = (deltaphi(3)- deltaphipold(3))

      yield=0.098d0
      angles=deltaphie
      ind=(/0.0,0.0,0.0/)
      do i=1, 3
          if (Abs(angles(i))>yield) then
            ind(i)=1
          end if
      end  do

      summation=ind(1)+ind(2)+ind(3)
      diffs(1)=deltaphie(1)-deltaphie(2)
      diffs(2)=deltaphie(1)-deltaphie(3)
      diffs(3)=deltaphie(2)-deltaphie(3)
      error=0.0000d0

c~~~~ Algorithm to update the plastic angle variations

c~~~~ Case 1 and 3.1

      if ((summation==1).or.
     & ((min(abs(diffs(1)),abs(diffs(2)),abs(diffs(3)))<yield).and.
     & (summation==3) )) then
        do while (max(abs(angles(1)), abs(angles(2)),abs(angles(3)) )>
     &    yield )
          do i = 1, 3
            if (ind(i) .eq. 1) then
                loc = i
                exit
            endif
          end do

          if(angles(loc)>yield) then
           res=angles(i)-yield
          end if
          if(angles(loc)<-yield) then
           res=angles(i)+yield
          end if
```

```
          do i=1, 3
            if (angles(i)>yield) then
              angles(i)=yield
            end if

            if (angles(i)<-yield) then
              angles(i)=-yield
            end if

            if (angles(i)>-yield .AND. angles(i)<-error
     &        .OR. angles(i)>error .AND. angles(i)<yield) then
              angles(i)=angles(i)+res/2
            end if
          end do
        end do
       end if

c~~~~ Case 2 and 3.2

       if ((summation==2).or.
     & ((min(abs(diffs(1)),abs(diffs(2)),abs(diffs(3)))>yield).and.
     & (summation==3) )) then
          do i=1, 3
            if (angles(i)>yield) then
              angles(i)=yield
              if (angles(i)<-yield) then
                angles(i)=-yield
              else
                angles(i)=0.d0
              end if
            end if
          end do
       end if

       deltaphipnew(1)=deltaphi(1)-angles(1)
       deltaphipnew(2)=deltaphi(2)-angles(2)
       deltaphipnew(3)=deltaphi(3)-angles(3)

c~~~~ Compute the updated average stress tensor

       TBAR(1,1)=(EMO*((3.0+Sqrt(5.0))*EMO*(HBAR(1,1)+HBAR(2,2)) +
     -           c*(3.0*(3.0+Sqrt(5.0))*HBAR(1,1)-(3.0+Sqrt(5.0))
     -           *HBAR(2,2)-6.0*deltaphipnew(1)*l)))/
     -           (4.0*Sqrt(3.0)*(c+EMO))

       TBAR(2,1)=-(c*EMO*(4.0*Sqrt(3.0)*HBAR(1,2)+4.0*Sqrt(3.0)*HBAR(1,2)
     -            -3.0*(-3.0+Sqrt(5.0))*(deltaphipnew(1)
     -           +2.0*deltaphipnew(2))*l))/
     -           (6.0*(-3.0+Sqrt(5.0))*(c+EMO))

       TBAR(1,2)=TBAR(2,1)

       TBAR(2,2)=(EMO*((3.0+Sqrt(5.0))*EMO*(HBAR(1,1)+HBAR(2,2)) +
     -           c*((-3.0-Sqrt(5.0))*HBAR(1,1)+3.0*(3.0+Sqrt(5.0))
     -           *HBAR(2,2)+6.0*deltaphipnew(1)*l)))/
     -           (4.0*Sqrt(3.0)*(c+EMO))

       stress(1)=TBAR(1,1)
       stress(2)=TBAR(2,2)
       stress(3)=TBAR(1,2)

       end
```

Bibliography

I. Ali and Y. J. Jun. Mathematical models for in-plane moduli of honeycomb structures—a review. *Research Journal of Applied Sciences, Engineering and Technology*, 7(3):581–592, 2014.

I. Q. Alonso and N. Fleck. The damage tolerance of a sandwich panel containing a cracked honeycomb core. *Journal of Applied Mechanics*, 76(6):061003, 2009.

T. Asada and N. Ohno. Fully implicit formulation of elastoplastic homogenization problem for two-scale analysis. *International Journal of Solids and Structures*, 44(22): 7261–7275, 2007.

T. Asada, Y. Tanaka, and N. Ohno. Two-scale analysis of honeycombs indented by flat punch. *International Journal of Modern Physics B*, 22(31n32):6191–6196, 2008.

T. Asada, Y. Tanaka, and N. Ohno. Two-scale and full-scale analyses of elastoplastic honeycomb blocks subjected to flat-punch indentation. *International Journal of Solids and Structures*, 46(7):1755–1763, 2009.

P. Bardhan. Ceramic honeycomb filters and catalysts. *Current Opinion in Solid State and Materials Science*, 2(5):577–583, 1997.

R. Beblo, J. Puttmann, J. Joo, and G. Reich. Shape memory polymer filled honeycomb model and experimental validation. *Smart Materials and Structures*, 24(2):025019, 2015.

A. Bertram. *Elasticity and plasticity of large deformations.* Springer, 2015.

A. Bertram and R. Glüge. *Solid Mechanics.* Springer, 2015.

A. Bertram and A. Kraska. Finite element simulation of texture development in polycrystalline metals. *Twefth International Conference on Texture of Materials*, pages 273–278, 1999.

D. Bigoni and T. Hueckel. Uniqueness and localization—i. associative and non-associative elastoplasticity. *International Journal of Solids and Structures*, 28(2):197–213, 1991.

T. Bitzer. *Honeycomb technology: materials, design, manufacturing, applications and testing.* Springer Science & Business Media, 2012.

G. Chochua, W. Shyy, and J. Moore. Computational modeling for honeycomb-stator gas annular seal. *International Journal of Heat and Mass Transfer*, 45(9):1849–1863, 2002.

B. D. Coleman and W. Noll. Material symmetry and thermostatic inequalities in finite elastic deformations. *Archive for Rational Mechanics and Analysis*, 15(2):87–111, 1964.

M. Considère. *Memoire sur l'emploi du fer et de l'acier dans les constructions*. Dunod, 1885.

E. Cosserat, F. Cosserat, et al. Théorie des corps déformables. 1909.

D. N. Cross. The use of honeycomb sandwich panels in engineering applications. *The Southern African Institute of Mining and Metallurgy*, 1990.

C. Darwin and W. F. Bynum. *The origin of species by means of natural selection: or, the preservation of favored races in the struggle for life*. AL Burt, 2009.

J. F. Davalos, P. Qiao, X. F. Xu, J. Robinson, and K. E. Barth. Modeling and characterization of fiber-reinforced plastic honeycomb sandwich panels for highway bridge applications. *Composite Structures*, 52(3):441–452, 2001.

C. Davini. Homogenization of linearly elastic honeycombs. *Mathematics and Mechanics of Solids*, 18(1):3–23, 2013.

R. De Borst, L. Sluys, H.-B. Muhlhaus, and J. Pamin. Fundamental issues in finite element analyses of localization of deformation. *Engineering Computations*, 10(2): 99–121, 1993.

F. dell'Isola, D. Steigmann, and A. Della Corte. Synthesis of fibrous complex structures: designing microstructure to deliver targeted macroscale response. *Applied Mechanics Reviews*, 67(6):060804, 2015.

F. dell'Isola, S. Bucci, and A. Battista. Against the fragmentation of knowledge: The power of multidisciplinary research for the design of metamaterials. In *Advanced Methods of Continuum Mechanics for Materials and Structures*, pages 523–545. Springer, 2016.

B. Dempsey, S. Eisele, and D. L. McDowell. Heat sink applications of extruded metal honeycombs. *International Journal of Heat and Mass Transfer*, 48(3):527–535, 2005.

V. Dias da Silva. A simple model for viscous regularization of elasto-plastic constitutive laws with softening. *International Journal for Numerical Methods in Biomedical Engineering*, 20(7):547–568, 2004.

B. J. Dimitrijevic and K. Hackl. A method for gradient enhancement of continuum damage models. *Techniche Mechanik*, 28(1):43–52, 2008.

D. C. Drucker. A definition of stable inelastic material. Technical report, DTIC Document, 1957.

D. C. Drucker. On the postulate of stability of material in the mechanics of continua. Technical report, Brown University Providence Rhode Island, 1963.

Y. Du, N. Yan, and M. T. Kortschot. Light-weight honeycomb core sandwich panels containing biofiber-reinforced thermoset polymer composite skins: fabrication and evaluation. *Composites Part B: Engineering*, 43(7):2875–2882, 2012.

G. C. Engelmayr Jr, M. Cheng, C. J. Bettinger, J. T. Borenstein, R. Langer, and L. E. Freed. Accordion-like honeycombs for tissue engineering of cardiac anisotropy. *Nature Materials*, 7(12):1003–1010, 2008.

D. J. Fahey, M. Dunlap, R. J. Seidl, et al. *Thermal conductivity of paper honeycomb cores and sound absorption of sandwich panels.* Madison, Wis.: US Dept. of Agriculture, Forest Service, Forest Products Laboratory, 1961.

H. P. Feigenbaum and Y. F. Dafalias. Directional distortional hardening in metal plasticity within thermodynamics. *International Journal of Solids and Structures*, 44(22): 7526–7542, 2007.

C. Florence and K. Sab. Overall ultimate yield surface of periodic tetrakaidecahedral lattice with non-symmetric material distribution. *Journal of Materials Science*, 40 (22):5883–5892, 2005.

C. C. Foo, G. B. Chai, and L. K. Seah. Mechanical properties of nomex material and nomex honeycomb structure. *Composite Structures*, 80(4):588–594, 2007.

G. Galilei. Discorsi e dimostrazioni matematiche intorno a due nuove scienze attenenti alla meccanica. *Elzevier, Leiden*, 1638.

J. George, J. Onodera, and T. Miyata. Biodegradable honeycomb collagen scaffold for dermal tissue engineering. *Journal of Biomedical Materials Research Part A*, 87(4): 1103–1111, 2008.

L. J. Gibson and M. F. Ashby. *Cellular solids: structure and properties.* Cambridge university press, 1997.

R. Glüge. Generalized boundary conditions on representative volume elements and their use in determining the effective material properties. *Computational Materials Science*, 79:408–416, 2013.

R. Glüge and S. Bucci. Does convexity of yield surfaces in plasticity have a physical significance? *Mathematics and Mechanics of Solids*, page 1081286517721599, 2017.

R. Gmeiner, U. Deisinger, J. Schönherr, B. Lechner, R. Detsch, A. Boccaccini, and J. Stampfl. Additive manufacturing of bioactive glasses and silicate bioceramics. *Journal of Ceramic Science and Technology*, 6(2):75–86, 2015.

S. Grove, E. Popham, and M. Miles. An investigation of the skin/core bond in honeycomb sandwich structures using statistical experimentation techniques. *Composites Part A: Applied Science and Manufacturing*, 37(5):804–812, 2006.

S. Gu, T. Lu, and A. Evans. On the design of two-dimensional cellular metals for combined heat dissipation and structural load capacity. *International Journal of Heat and Mass Transfer*, 44(11):2163–2175, 2001.

B. Haghpanah, R. Oftadeh, J. Papadopoulos, and A. Vaziri. Self-similar hierarchical honeycombs. In *Proceedings of the Royal Socciety A*, volume 469, page 20130022. The Royal Society, 2013.

B. Haghpanah, J. Papadopoulos, and A. Vaziri. Plastic collapse of lattice structures under a general stress state. *Mechanics of Materials*, 68:267–274, 2014.

T. C. Hales. The honeycomb conjecture. *Discrete & Computational Geometry*, 25(1): 1–22, 2001.

J. T. A. Herbert. Method of making stainless steel honeycomb panels, 1960. US Patent 2,962,811.

R. Hill. Elastic properties of reinforced solids: some theoretical principles. *Journal of the Mechanics and Physics of Solids*, 11(5):357–372, 1963.

R. Höfler and S. Renyi. Plattenförmiger Baukörper. *DE355036*, 1914.

J. Hohe and W. Becker. Effective elastic properties of triangular grid structures. *Composite Structures*, 45(2):131–145, 1999.

S.-T. Hong, J. Pan, T. Tyan, and P. Prasad. Quasi-static crush behavior of aluminum honeycomb specimens under compression dominant combined loads. *International Journal of Plasticity*, 22(1):73–109, 2006.

M. Hori and S. Nemat-Nasser. On two micromechanics theories for determining micro–macro relations in heterogeneous solids. *Mechanics of Materials*, 31(10):667–682, 1999.

J. Jiang, H. I. Ling, and V. N. Kaliakin. An associative and non-associative anisotropic bounding surface model for clay. *Journal of Applied Mechanics*, 79(3):031010, 2012.

D. Karagiozova and T. Yu. Plastic deformation modes of regular hexagonal honeycombs under in-plane biaxial compression. *International Journal of Mechanical Sciences*, 46 (10):1489–1515, 2004.

D. Karagiozova and T. Yu. Strain localization in circular honeycombs under in-plane biaxial quasi-static and low-velocity impact loading. *International Journal of Impact Engineering*, 35(8):753–770, 2008.

B. Kim and R. M. Christensen. Basic two-dimensional core types for sandwich structures. *International Journal of Mechanical Sciences*, 42(4):657–676, 2000.

T. A. Laursen. *Computational contact and impact mechanics: fundamentals of modeling interfacial phenomena in nonlinear finite element analysis*. Springer Science & Business Media, 2013.

X. Lei and C. J. Lissenden. Pressure sensitive nonassociative plasticity model for DRA composites. *Journal of Engineering Materials and Technology*, 129(2):255–264, 2007.

V. Lubarda, S. Mastilovic, and J. Knap. Some comments on plasticity postulates and non-associative flow rules. *International Journal of Mechanical Sciences*, 38(3):247–258, 1996.

G. Maier and T. Hueckel. Nonassociated and coupled flow rules of elastoplasticity for rock-like materials. In *International Journal of Rock Mechanics and Mining Sciences & Geomechanics Abstracts*, volume 16, pages 77–92. Elsevier, 1979.

N. Manopulo, F. Barlat, and P. Hora. Isotropic to distortional hardening transition in metal plasticity. *International Journal of Solids and Structures*, 56:11–19, 2015.

M. T. Manzari and K. Yonten. On implementation and performance of an anisotropic constitutive model for clays. *International Journal of Computational Methods*, 11(02): 1342009, 2014.

I. Masters and K. Evans. Models for the elastic deformation of honeycombs. *Composite Structures*, 35(4):403–422, 1996.

C. Miehe and A. Koch. Computational micro-to-macro transitions of discretized microstructures undergoing small strains. *Archive of Applied Mechanics*, 72(4-5):300–317, 2002.

C. Miehe, J. Schröder, and M. Becker. Computational homogenization analysis in finite elasticity: material and structural instabilities on the micro-and macro-scales of periodic composites and their interaction. *Computer Methods in Applied Mechanics and Engineering*, 191(44):4971–5005, 2002.

R. D. Mindlin. Micro-structure in linear elasticity. *Archive for Rational Mechanics and Analysis*, 16(1):51–78, 1964.

R. D. Mindlin. Second gradient of strain and surface-tension in linear elasticity. *International Journal of Solids and Structures*, 1(4):417–438, 1965.

D. Mohr. Multi-scale finite-strain plasticity model for stable metallic honeycombs incorporating microstructural evolution. *International Journal of Plasticity*, 22(10):1899–1923, 2006.

D. Mohr and M. Doyoyo. Experimental investigation on the plasticity of hexagonal aluminum honeycomb under multiaxial loading. *Journal of Applied Mechanics*, 71: 375–385, 2004a.

D. Mohr and M. Doyoyo. Large plastic deformation of metallic honeycomb: orthotropic rate-independent constitutive model. *International Journal of Solids and Structures*, 41(16):4435–4456, 2004b.

A. Needleman. Material rate dependence and mesh sensitivity in localization problems. *Computer Methods in Applied Mechanics and Engineering*, 67(1):69–85, 1988.

M. S. Niazi, H. Wisselink, and T. Meinders. Viscoplastic regularization of local damage models: revisited. *Computational Mechanics*, 51(2):203–216, 2013.

M. Ortiz and E. P. Popov. Distortional hardening rules for metal plasticity. *Journal of Engineering Mechanics*, 109(4):1042–1057, 1983.

S.-D. Pan, L.-Z. Wu, Y.-G. Sun, Z.-G. Zhou, and J.-L. Qu. Longitudinal shear strength and failure process of honeycomb cores. *Composite Structures*, 72(1):42–46, 2006.

S.-D. Pan, L.-Z. Wu, and Y.-G. Sun. Transverse shear modulus and strength of honeycomb cores. *Composite Structures*, 84(4):369–374, 2008.

S. Papka and S. Kyriakides. Biaxial crushing of honeycombs:—part I: Experiments. *International Journal of Solids and Structures*, 36(29):4367–4396, 1999a.

S. Papka and S. Kyriakides. In-plane biaxial crushing of honeycombs—: Part II: Analysis. *International Journal of Solids and Structures*, 36(29):4397–4423, 1999b.

S. D. Papka and S. Kyriakides. In-plane compressive response and crushing of honeycomb. *Journal of the Mechanics and Physics of Solids*, 42(10):1499–1532, 1994.

S. D. Papka and S. Kyriakides. Experiments and full-scale numerical simulations of in-plane crushing of a honeycomb. *Acta materialia*, 46(8):2765–2776, 1998a.

S. D. Papka and S. Kyriakides. In-plane crushing of a polycarbonate honeycomb. *International Journal of Solids and Structures*, 35(3-4):239–267, 1998b.

R. Peerlings, W. Brekelmans, R. de Borst, and M. Geers. Softening, singularity and mesh sensitivity in quasi-brittle and fatigue damage, in nonlocal aspects in solid mechanics. In *Proceedings of EUROMECH Colloquium*, volume 378, pages 94–99, 1998.

A. Petras and M. Sutcliffe. Failure mode maps for honeycomb sandwich panels. *Composite Structures*, 44(4):237–252, 1999.

J. Pflug, I. Verpoest, and D. Vandepitte. Folded honeycomb. fast and continuous production of the core and a reliable core-skin bond. In *International Conference on Composite Materials*, 1999.

G. Piola. *La meccanica de' corpi naturalmente estesi: trattata col calcolo delle variazioni.* Paolo Emilio Giusti, 1833.

J. C. Reiher, I. Giorgio, and A. Bertram. Finite-element analysis of polyhedra under point and line forces in second-strain gradient elasticity. *Journal of Engineering Mechanics*, 143(2):04016112, 2016.

L. Russo. *The forgotten revolution: how science was born in 300 BC and why it had to be reborn.* Springer Science & Business Media, 2013.

K. S. Sacks. *Diodorus Siculus and the first century.* Princeton University Press, 2014.

C. C. Seepersad, B. M. Dempsey, J. K. Allen, F. Mistree, and D. L. McDowell. Design of multifunctional honeycomb materials. *American Institute of Aeronautics and Astronautics Journal*, 42(5):1025–1033, 2004.

B. Shi and J. Mosler. On the macroscopic description of yield surface evolution by means of distortional hardening models: application to magnesium. *International Journal of Plasticity*, 44:1–22, 2013.

J. C. Simo and R. L. Taylor. Consistent return mapping algorithm for plane stress elasto-plasticity. Technical report, Stanford Univ., CA (USA). Div. of Applied Mechanics; California Univ., Berkeley (USA). Div. of Structural Engineering and Structural Mechanics, 1985.

W. Sumelka and M. Nowak. Non-normality and induced plastic anisotropy under fractional plastic flow rule: a numerical study. *International Journal for Numerical and Analytical Methods in Geomechanics*, 2015.

A. Taherizadeh, D. E. Green, and J. W. Yoon. Evaluation of advanced anisotropic models with mixed hardening for general associated and non-associated flow metal plasticity. *International Journal of Plasticity*, 27(11):1781–1802, 2011.

N. Tejavibulya, J. Youssef, B. Bao, T.-M. Ferruccio, and J. R. Morgan. Directed self-assembly of large scaffold-free multi-cellular honeycomb structures. *Biofabrication*, 3 (3):034110, 2011.

J. Tejchman. *Confined Granular Flow in Silos: Experimental and Numerical Investigations.* Springer Science & Business Media, 2013.

S. Timoshenko. *History of strength of materials: with a brief account of the history of theory of elasticity and theory of structures.* Courier Corporation, 1953.

S. P. Timoshenko and S. Woinowsky-Krieger. *Theory of plates and shells.* McGraw-Hill, 1959.

S. Torquato, L. Gibiansky, M. Silva, and L. Gibson. Effective mechanical and transport properties of cellular solids. *International Journal of Mechanical Sciences*, 40(1):71–82, 1998.

R. A. Toupin. Elastic materials with couple-stresses. *Archive for Rational Mechanics and Analysis*, 11(1):385–414, 1962.

J. R. Vinson. Optimum design of composite honeycomb sandwich panels subjected to uniaxial compression. *American Institute of Aeronautics and Astronautics Journal*, 24 (10):1690–1696, 1986.

H. N. Wadley. Multifunctional periodic cellular metals. *Philosophical Transactions of the Royal Society of London A: Mathematical, Physical and Engineering Sciences*, 364 (1838):31–68, 2006.

A.-J. Wang and D. L. McDowell. In-plane stiffness and yield strength of periodic metal honeycombs. *Journal of Engineering Materials and Technology*, 126(2):137–156, 2004.

A.-J. Wang and D. L. McDowell. Yield surfaces of various periodic metal honeycombs at intermediate relative density. *International Journal of Plasticity*, 21(2):285–320, 2005.

Y. Wang and A. M. Cuitiño. Three-dimensional nonlinear open-cell foams with large deformations. *Journal of the Mechanics and Physics of Solids*, 48(5):961–988, 2000.

A. Wilbert, W. Y. Jang, S. Kyriakides, and J. Floccari. Buckling and progressive crushing of laterally loaded honeycomb. *International Journal of Solids and Structures*, 48(5): 803–816, 2011.

J. Zhang and M. Ashby. Buckling of honeycombs under in-plane biaxial stresses. *International Journal of Mechanical Sciences*, 34(6):491–509, 1992.

Q. Zhang, X. Yang, P. Li, G. Huang, S. Feng, C. Shen, B. Han, X. Zhang, F. Jin, F. Xu, et al. Bioinspired engineering of honeycomb structure–using nature to inspire human innovation. *Progress in Materials Science*, 74:332–400, 2015.

H. Zhu and N. Mills. The in-plane non-linear compression of regular honeycombs. *International Journal of Solids and Structures*, 37(13):1931–1949, 2000.